

AD-A206 083

①



DEVELOPMENT OF THE EXTENDED KALMAN FILTER
 FOR THE ADVANCED COMPLETELY INTEGRATED
 REFERENCE INSTRUMENTATION SYSTEM (CRIS)

THESIS

Joseph K. Solomon, B.S.M.E.
Captain, USAF

DTIC
 ELECTE
 S 29 MAR 1989 D
 E

DEPARTMENT OF THE AIR FORCE
 AIR UNIVERSITY

AIR FORCE INSTITUTE OF TECHNOLOGY

Wright-Patterson Air Force Base, Ohio

This document has been approved
 for public release and sale in
 unlimited distribution.

89 3 29 034

AFIT/GE/ENG/89M-8



**DEVELOPMENT OF THE EXTENDED KALMAN FILTER
FOR THE ADVANCED COMPLETELY INTEGRATED
REFERENCE INSTRUMENTATION SYSTEM (CIRIS)**

THESIS

*Joseph K. Solomon, B.S.M.F.
Captain, USAF*

DTIC
ELECTE
S 29 MAR 1989 **D**
E

Approved for public release; distrubution unlimited

AFIT/GE/ENG/89M-8

**DEVELOPMENT OF THE EXTENDED KALMAN FILTER
FOR THE ADVANCED COMPLETELY INTEGRATED
REFERENCE INSTRUMENTATION SYSTEM (CIRIS)**

THESIS

**Presented to the Faculty of the School of Engineering
of the Air Force Institute of Technology
Air University
In Partial Fulfillment of the
Requirements for the Degree of
Master of Science in Electrical Engineering**

**Joseph K. Solomon, B.S.M.E
Captain, USAF**

March 1989

Approved for public release; distribution unlimited

Classification
Distribution
U.S. Government
Work
This work is in the
public domain in the
United States of America
except where copyright
protection may apply
to otherwisely
indicated material
DISTRIBUTION STATEMENTS
1. THIS DOCUMENT IS UNCLASSIFIED
2. DATE OF DECLASSIFICATION
3. BY
4. THIS DOCUMENT IS UNCLASSIFIED
DATE OF DECLASSIFICATION
BY
1A1



REPORT DOCUMENTATION PAGE				Form Approved OMB No. 0704-0188	
1a. REPORT SECURITY CLASSIFICATION UNCLASSIFIED			1b. RESTRICTIVE MARKINGS		
2a. SECURITY CLASSIFICATION AUTHORITY			3. DISTRIBUTION / AVAILABILITY OF REPORT Approved for Public Release; Distribution Unlimited		
2b. DECLASSIFICATION / DOWNGRADING SCHEDULE					
4. PERFORMING ORGANIZATION REPORT NUMBER(S) AFIT/GE/ENG/89M-8			5. MONITORING ORGANIZATION REPORT NUMBER(S)		
6a. NAME OF PERFORMING ORGANIZATION School of Engineering		6b. OFFICE SYMBOL (if applicable) AFIT/ENG	7a. NAME OF MONITORING ORGANIZATION		
6c. ADDRESS (City, State, and ZIP Code) Air Force Institute of Technology Wright-Patterson AFB, OH 45433-6583			7b. ADDRESS (City, State, and ZIP Code)		
8a. NAME OF FUNDING / SPONSORING ORGANIZATION 6585th Test Group		8b. OFFICE SYMBOL (if applicable) GDN	9. PROCUREMENT INSTRUMENT IDENTIFICATION NUMBER		
8c. ADDRESS (City, State, and ZIP Code) Holloman AFB, NM 88230-5000			10. SOURCE OF FUNDING NUMBERS		
			PROGRAM ELEMENT NO.	PROJECT NO.	TASK NO.
			WORK UNIT ACCESSION NO.		
11. TITLE (Include Security Classification) See Block 19					
12. PERSONAL AUTHOR(S) Joseph K. Solomon, Capt, USAF, BSME					
13a. TYPE OF REPORT MS Thesis		13b. TIME COVERED FROM _____ TO _____		14. DATE OF REPORT (Year, Month, Day) 1989 March	15. PAGE COUNT 166
16. SUPPLEMENTARY NOTATION					
17. COSATI CODES			18. SUBJECT TERMS (Continue on reverse if necessary and identify by block number) INERTIAL NAVIGATION SYSTEM, KALMAN FILTER, COVARIANCE ANALYSIS, CIRIS, GLOBAL POSITIONING SYSTEM. Thesis. JES		
FIELD	GROUP	SUB-GROUP			
17	07	03			
19. ABSTRACT (Continue on reverse if necessary and identify by block number) Title: Development of the Extended Kalman Filter for the Advanced Completely Integrated Reference Instrumentation System (CIRIS) Thesis Chairman: Lt Col Z. H. Lewantowicz (Abstract on Back)					
20. DISTRIBUTION / AVAILABILITY OF ABSTRACT <input checked="" type="checkbox"/> UNCLASSIFIED/UNLIMITED <input type="checkbox"/> SAME AS RPT. <input type="checkbox"/> DTIC USERS			21. ABSTRACT SECURITY CLASSIFICATION UNCLASSIFIED		
22a. NAME OF RESPONSIBLE INDIVIDUAL Lt Col Z. H. Lewantowicz			22b. TELEPHONE (Include Area Code) 513-255-2024		22c. OFFICE SYMBOL AFIT/ENG

Block 19 (Continued):

Abstract

The Completely Integrated Reference Instrumentation System (CIRIS) was developed by the Central Inertial Guidance Test Facility (CIGTF) at Holloman AFB, NM. The CIRIS system is an inertial navigation system (INS) aided with line-of-sight range and range-rate measurements from surveyed ground transponders. The information from the measurement and INS data is combined using an extended Kalman filter to produce an accurate estimate of the INS position and velocity errors. The accurate CIRIS aircraft position and velocity data is used as a baseline reference to determine the performance capabilities of proposed aircraft navigation systems. The new aircraft navigation systems projected in the next five years will attain accuracies approaching the level of the current CIRIS system. In order to test these systems, the accuracy of CIRIS will be increased through the addition of aiding measurements from the Global Positioning System (GPS).

The purpose of this research is to develop the "truth" model that describes all known error sources in the current CIRIS. Based on current literature and experiments at CIGTF, a 127-state Kalman filter "truth" model is designed. This model includes the measurement errors due to inaccuracies in the transponder surveys and measurement errors caused by atmospheric propagation delays. This full-ordered Kalman filter is used to process the empirical data from a representative CIRIS flight. The Kalman filter residuals, correlated error states, and position/velocity error estimates are analyzed and compared to the current CIRIS filter data to verify the accuracy of the "truth" model. Based on the 127-state "truth" model, a 70-state reduced-ordered filter is derived to decrease computer processing time with a minimum loss in performance. These models will serve as the foundation for the design of an extended Kalman filter that uses the information from both transponder and GPS measurements.

Preface

The current CIRIS system uses measurements from surveyed ground transponders to aid its Kalman filter in estimating the errors in its inertial navigation system. The goal of this research is to develop a Kalman filter "truth" model that describes all known error sources in the current CIRIS system. The "truth" model developed in this research will serve as the foundation for the future development of a Kalman filter that uses measurements from both ground transponders and Global Positioning System (GPS) satellites. The measurements from GPS satellites are required to increase the accuracy of current CIRIS to a level that will allow it to serve as a reference baseline for testing future, high accuracy aircraft navigation systems.

The primary tool used in conducting this research is the Multimode Simulation for Optimal Filter Evaluation (MSOFE) software developed by the Avionics Laboratory at Wright-Patterson AFB, OH. The power and capabilities of this package are proportional to the current lack of documentation on how to use it. I am indebted to Mr. Robert Urbanic, an engineer at the lab, for his guidance in learning the intricacies and anomalies of MSOFE. Without his help this research would have never got off the ground.

I chose to use the AFIT VAX VMS computers for conducting my simulations and software development because of the power and ease-of-use of these systems. The programs I used on these computers pushed the machines to their computational limits. In doing this many anomalies occurred and I must thank Mr. Daniel Zambon and Mr. Robert Ewing for their time in helping me understand the limitations of these computer systems. Unlike the other AFIT computer system managers, they always had time for my questions.

Finally, special thanks to my faculty advisor and mentor: Lt Col Lewantowicz. This man defines the term workaholic, which was lucky for me. He could be found at all hours of the day or night working away in his office and he always had time for a question. His knowledge, experience, and ideas are an integral part of this thesis. There were many times when he had me working at levels that I did not think were possible and without his incessant

motivation I would have not been able to progress as far as I did. I feel that the knowledge and experience I gained through our interactions will benefit me throughout my engineering career.

Joseph K. Solomon

Table of Contents

	Page
Preface	ii
List of Figures	vi
List of Tables	viii
Abstract	ix
I. Introduction	1-1
Background	1-4
Research Objectives	1-6
Research Approach	1-7
Overview	1-9
II. Theory	2-1
Reference Frames	2-1
Earth Fixed Frame	2-1
Navigation Frame	2-1
Coordinate Transformations	2-3
Inertial Navigation System	2-5
Hardware	2-5
Error State Mechanization Equations	2-6
Transponders	2-8
Range Measurement	2-8
Range-Rate Measurement	2-10
Current CIRIS Filter Model	2-10
Kalman Filter Equations	2-13
Correlated Error and Residual Characteristics	2-17
Simulation Software	2-20
Multimode Simulation for Optimal Filter Evaluation (MSOFE)	2-20
Profile Generator (PROFGEN)	2-21
MATRIX _x	2-22
Summary	2-22
III. INS "Truth" Model Design/Verification	3-1
Error States	3-1
INS Stochastic Differential Equation	3-2
Elements of the F _{INS} Matrix	3-4
Elements of the Q matrix	3-8
Alignment Simulation	3-9
Aircraft Trajectory Simulations	3-12
Static Profile	3-12
Fighter Profile	3-12
Summary	3-14

	Page
IV. INS/Transponder "Truth" Model Design/Verification	4-1
Range Measurement Model	4-1
Range-Rate Measurement Model	4-4
Full-Ordered Kalman Filter "Truth" Model	4-6
CIRIS Flight Simulation	4-9
Residual Analysis	4-12
Full Ordered Filter Data	4-17
Means and 1 σ Values.	4-17
Means and 1 σ Value Differences.	4-19
Correlated Measurement Error Analysis	4-24
Transponder Survey Errors.	4-24
Atmospheric Errors.	4-30
Calibration Errors.	4-30
Summary	4-33
V. Reduced Order Filter Design/Simulation	5-1
Selection of States	5-1
Filter Model	5-2
Comparison of Reduced to "Truth"	5-3
Covariance Analysis Consideration	5-5
Comparison of the Reduced and CIRIS filters	5-6
Position and Velocity Differences.	5-6
Correlated Error Model Performnce.	5-10
Summary	5-14
VI. Conclusions and Recommendations	6-1
Conclusions	6-1
Recommendations	6-3
Additional CIRIS Flights.	6-3
Correlated Errors.	6-3
Filter Tuning.	6-3
Acceleration Data.	6-4
Higher Sampling Rate.	6-4
Smoothing Algorithm.	6-4
GPS Measurements.	6-5
Appendix A: A Historical Review of the CIRIS Development and Operation ...	A-1
Appendix B: Initial Covariance, Noise Strengths, and Dynamics Matrix Elements for the INS "Truth" Model	B-1
Appendix C: Initial Covariance, Noise Strengths, Dynamics Matrix, and Measurement Gradient Matrix Elements for the Measurement "Truth" Model	C-1
Appendix D: INS and Baro Altimeter CIRIS Flight Data	D-1
Bibliography	bi-1
Vita	v-1

List of Figures

Figure		Page
1-1.	Physical Concept of CIRIS.....	1-2
1-2.	Physical Concept of Advanced CIRIS	1-3
1-3.	Advanced CIRIS Indirect Kalman Filter.....	1-4
2-1.	WGS 84 Ellipsoidal Model	2-2
2-2.	Navigation Frame	2-3
2-3.	Random Bias Shaping Filter Characteristics.....	2-18
2-4.	First Order Markov Shaping Filter Characteristics	2-19
2-5.	Gaussian "White" Noise.....	2-20
3-1.	RMS Errors for Alignment Simulation	3-11
3-2.	1 σ Values for the Static Simulation	3-13
3-3.	PROFGEN Fighter Profile	3-15
3-4.	1 σ Values for the Fighter Simulation.....	3-16
4-1.	Errors in Calculated Measurement.....	4-2
4-2.	CIRIS Flight Trajectory.....	4-10
4-3.	CIRIS Abbreviated Flight Profile.....	4-11
4-4.	Range Residuals (CIRIS and "TRUTH").....	4-14
4-5.	Range-Rate Residuals (CIRIS and "TRUTH")	4-16

Figure	Page
4-6. Position Error States ("TRUTH").....	4-18
4-7. Velocity Error States ("TRUTH").....	4-20
4-8. Position Differences ("TRUTH" - CIRIS)	4-22
4-9. Velocity Differences ("TRUTH" - CIRIS).....	4-23
4-10. T-181 X' and Y' Correlated Errors	4-25
4-11. T-181 Z' and ATM Correlated Errors	4-26
4-12. T-185 X' and Y' Correlated Errors	4-28
4-13. T-185 Z' and ATM Correlated Errors	4-29
4-14. T-186 X' and Y' Correlated Errors	4-31
4-15. T-186 Z' and ATM Correlated Errors.....	4-32
4-16. Range and Range-Rate Correlated Errors	4-34
5-1. Position and Velocity Differences ("TRUTH" - REDUCED)	5-4
5-2. Position Differences (REDUCED - CIRIS)	5-7
5-3. Velocity Differences (REDUCED - CIRIS)	5-8
5-4. Range Residual T-181 and T-163	5-11
5-5. T-181/T-163 X' and Y' Correlated Errors	5-12
5-6. T-181/T-163 Z' and ATM Correlated Errors	5-13

List of Tables

Table	Page
2-1. WGS 84 Constants	2-2
2-2. Range Measurement Frequencies.....	2-9
3-1. Error State Partitions	3-3
4-1. Range Residual Statistical Comparison	4-13
4-2. Range-Rate Residual Statistical Comparison.....	4-15
4-3. Position Error State Differences.....	4-21
4-4. Velocity Error State Differences	4-24
5-1. "TRUTH"/Reduced Position/Velocity Error State Differences	5-5
5-2. Reduced/CIRIS Position Error State Differences	5-9
5-3. Reduced/CIRIS Velocity Error State Differences.....	5-10
6-1. "TRUTH"/Reduced/CIRIS Position Error State Differences.....	6-2
6-2. "TRUTH"/Reduced/CIRIS Velocity Error State Differences	6-3

Abstract

The Completely Integrated Reference Instrumentation System (CIRIS) was developed by the Central Inertial Guidance Test Facility (CIGTF) at Holloman AFB, NM. The CIRIS system is an inertial navigation system (INS) aided with line-of-sight range and range-rate measurements from surveyed ground transponders. The information from the measurement and INS data is combined using an extended Kalman filter to produce an accurate estimate of the INS position and velocity errors. The accurate CIRIS aircraft position and velocity data is used as a baseline reference to determine the performance capabilities of proposed aircraft navigation systems. The new aircraft navigation systems projected in the next five years will attain accuracies approaching the level of the current CIRIS system. In order to test these systems, the accuracy of CIRIS will be increased through the addition of aiding measurements from the Global Positioning System (GPS).

The purpose of this research is to develop the "truth" model that describes all known error sources in the current CIRIS. Based on current literature and experiments at CIGTF, a 127-state Kalman filter "truth" model is designed. This model includes the measurement errors due to inaccuracies in the transponder surveys and measurement errors caused by atmospheric propagation delays. This full-ordered Kalman filter is used to process the empirical data from a representative CIRIS flight. The Kalman filter residuals, correlated error states, and position/velocity error estimates are analyzed and compared to the current CIRIS filter data to verify the accuracy of the "truth" model. Based on the 127-state "truth" model, a 70-state reduced-ordered filter is derived to decrease computer processing time with a minimum loss in performance. These models will serve as the foundation for the design of an extended Kalman filter that uses the information from both transponder and GPS measurements.

DEVELOPMENT OF THE EXTENDED KALMAN FILTER FOR THE ADVANCED COMPLETELY INTEGRATED REFERENCE INSTRUMENTATION SYSTEM (CIRIS)

I. Introduction

The Completely Integrated Reference Instrumentation System (CIRIS) is a term that refers to a transponder aided Inertial Navigation System (INS) currently used by the Air Force for testing new aircraft navigation systems. The Office of Primary Responsibility (OPR) for this system is the Central Inertial Guidance Test Facility (CIGTF), 6585th Test Group, Air Force Systems Command (AFSC), Holloman AFB, NM. The basic idea is to fly the navigation system to be tested, the test article, and the CIRIS system over an aircraft trajectory of interest through the CIRIS transponder range. The data from both systems is recorded during flight and compared to determine how closely the test system followed the CIRIS system. The CIRIS system is considered to be much more accurate than the navigation systems currently being tested and therefore the CIRIS data serves as a baseline for determining performance of current aircraft navigation systems (15).

The current CIRIS system is capable of providing the aircraft's latitude and longitude with an accuracy of 13 feet (ft) 1σ ; altitude with an accuracy of 40 ft 1σ ; north and west velocity with an accuracy 0.1 ft/sec (fps) 1σ ; and vertical velocity with an accuracy of 0.4 fps 1σ (the 1σ value indicates a 68.3% probability that the position/velocity true error lies in the interval between $[m - \sigma, m + \sigma]$, where m is the estimated mean). The high accuracy of the CIRIS system is due to the transponder measurement aiding. Figure 1-1 depicts the basic concept.

Ground based transponders are installed over a test range that can cover the entire length and width of the United States land mass. The positions of these transponders are surveyed and known precisely; CIGTF estimates the accuracy of these surveys at

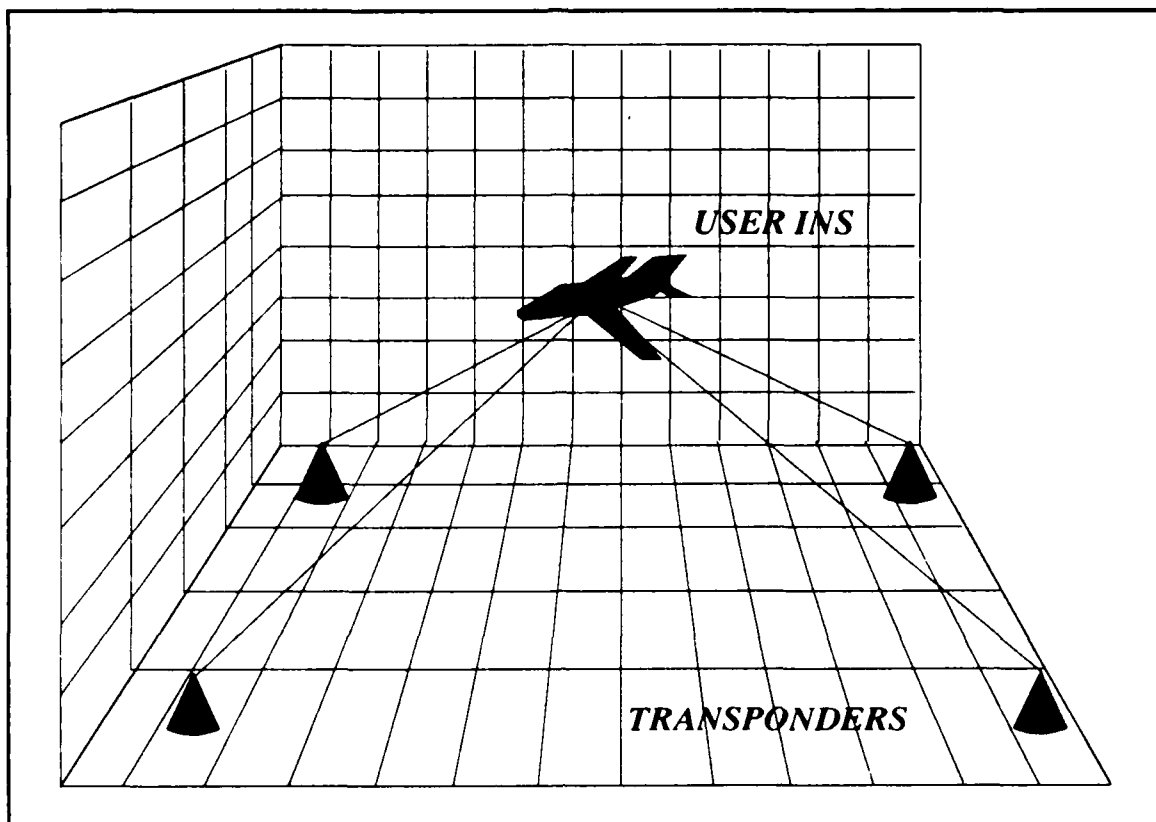


Figure 1-1. Physical Concept of CIRIS

approximately 3-6 ft 1σ . During testing the CIRIS system receives an accurate measurement of the host aircraft's range and range-rate. The range and range-rate measurements from each transponder are optimally combined with the CIRIS INS data, in an extended Kalman filter, to produce an accurate estimate of the error in the INS data. The INS data is corrected to produce an accurate estimate of the aircraft position and velocity. Currently this data is much more accurate than the standard aircraft navigation systems (15). A historical review of the development and operation of CIRIS is presented in Appendix A.

To increase the accuracy of the CIRIS system it has been proposed that pseudorange and delta-range measurements from the Global Positioning System (GPS) be added to the transponder measurements to increase the accuracy of the CIRIS system data. This

concept is shown in Figure 1-2 and is similar to the transponder idea. The positions of the satellites are known precisely and accurate pseudorange and delta-range measurements from available GPS satellites can be provided to the CIRIS system.

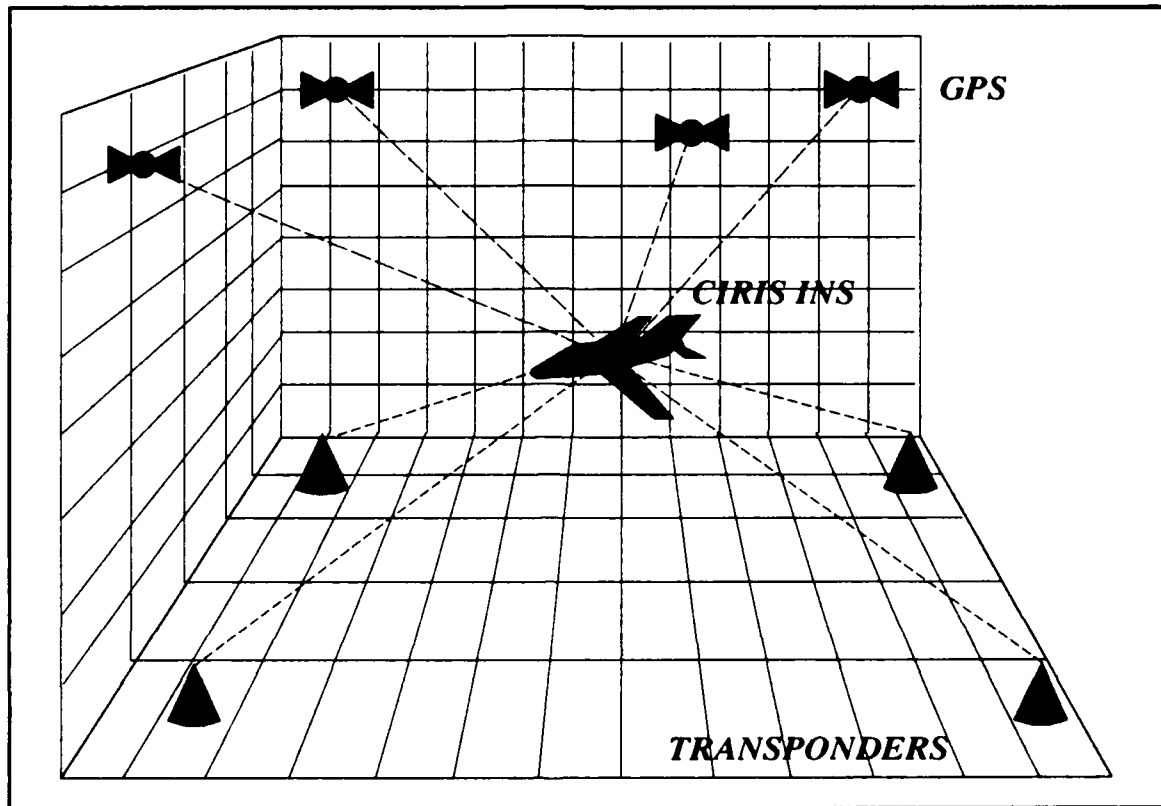


Figure 1-2. Physical Concept of Advanced CIRIS

The GPS range (R_{SAT}), GPS range-rate (V_{SAT}), transponder range (R_{TRANS}), transponder range-rate (V_{TRANS}), and baro altimeter (H_B) measurements are optimally combined with INS position (P), velocity (V), and acceleration (A) data, through the use of an extended Kalman filter, to estimate the error in the CIRIS INS. This filter concept is shown in Figure 1-3. The CIRIS INS data is corrected, resulting in an accurate estimate of aircraft position and velocity. This estimate is expected to be more accurate than that of the current CIRIS system (15).

This thesis research effort concentrates on developing and verifying a realistic full-ordered "truth" model that describes all known error sources in the current CIRIS

system (INS/Transponder). This "truth" model is the foundation for future research into the design of an extended Kalman filter based on an INS/Transponder/GPS model; initial research into this area is presented in Reference (20).

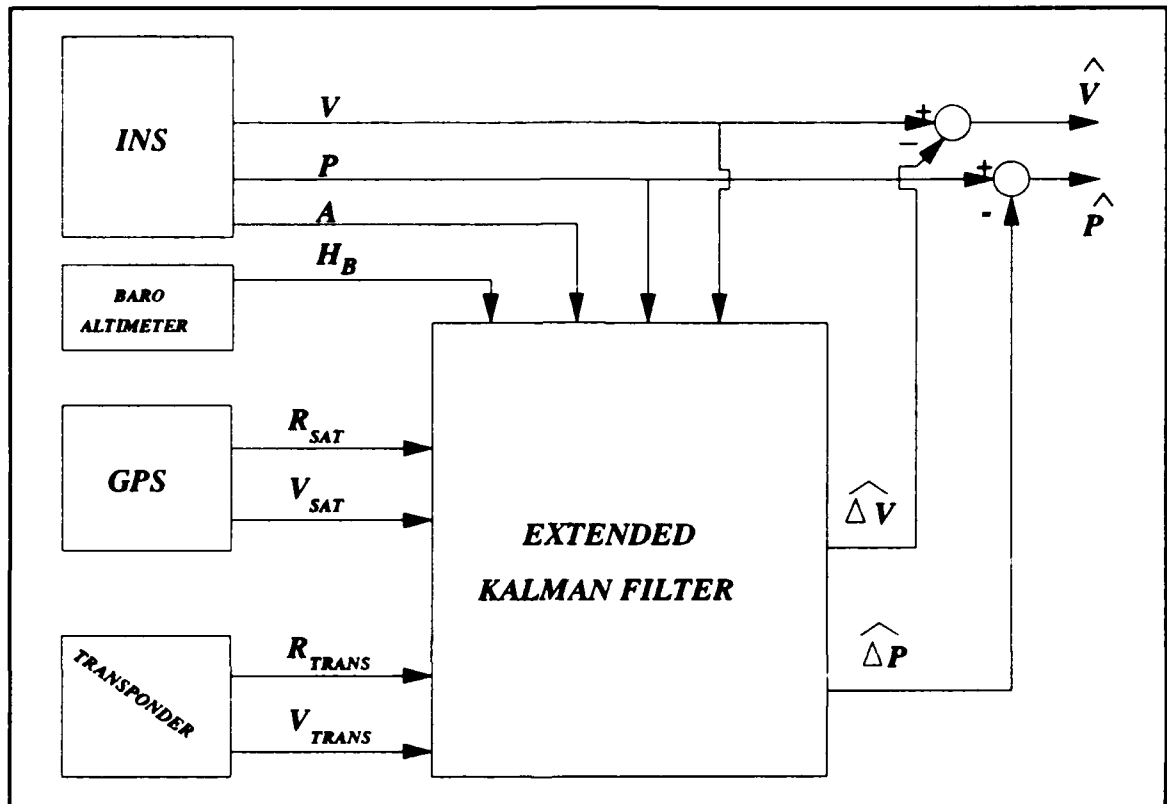


Figure 1-3. Advanced CIRIS Indirect Kalman Filter

Background

The original CIRIS system is based on a reduced-order Kalman filter consisting of 14 states. This filter is based on the 9 primary error states of the Litton LN-15 INS, two vertical channel aiding states, and 3 error states reserved for estimating errors in Doppler velocity aiding measurements; the Doppler velocity error states were never used because initial tests indicated these additional states provided an insignificant increase in accuracy. The correlated transponder and atmospheric measurement error sources are modeled as uncorrelated white noise. This filter is limited to 14 states, of which only 11 are being used, due to computer limitations that existed during the initial filter design process. This system is designated CIRIS I by CIGTF (18).

In the current CIRIS system the Litton LN-15 INS has been replaced by the Litton LN-39 INS. The main reason for this change was to increase the overall reliability of the CIRIS system. This system is designated CIRIS II by CIGTF, and the current CIRIS system data referred throughout this thesis is from the CIRIS II system (18).

Due to the low number of states, limitations exist in the Kalman filter model currently being used by CIRIS. A higher ordered Kalman filter model, including the correlated measurement errors, is required to increase the CIRIS filter's accuracy. Current state of the art computational capabilities allow a higher ordered filter to be realistically implemented. A new Kalman filter design based on the CIRIS system, with the Litton LN-39 INS, and the addition of GPS range and range-rate aiding measurements, promise to achieve a maximum increase in the accuracy and stability of the CIRIS velocity and position data.

The majority of current research in this area has been directed towards the integration of GPS measurements with INS systems. Of the many papers published in this area, the paper by D. B. Cox (6:144-153) is most representative. This paper generally explores the advantages of GPS integration with INS systems and serves to justify the idea of integrating CIRIS with GPS. Previous AFIT research in this area was undertaken by R. Butler and G. Rhue, who designed a GPS/INS system with a 15-state Kalman filter which performed well (4).

The idea of aiding an INS with GPS and transponders is unique to CIRIS and there are no known current papers published in this area. However, there has been one AFIT research effort conducted by C. Smith in 1985 (19). He designed a 13-state Kalman filter for the INS/GPS data integration. His filter performed well also, but with the advances in technology since his thesis was written, there exists the ability to improve his filter. The INS model used by Smith was designed for the Litton LN-15 INS which is now obsolete. The advanced CIRIS Kalman filter will be based on the state of the art Litton LN-39 standard INS and a Kalman filter of approximately 100 states. The models are expanded to allow better Kalman filter error estimation.

Past research has proven that the integration of an INS with GPS and/or transponders can significantly increase the accuracy of aircraft navigation systems. This thesis research effort builds on past developments and applies it specifically to the hardware proposed for advanced CIRIS. Through the use of detailed system models and the latest technology in Kalman filter development, this research ultimately provides an advanced CIRIS system model with a significant increase in accuracy and stability over the current CIRIS.

Research Objectives

The first step in the efficient design of a reduced-order Kalman filter is the development of a full-ordered "truth" model. This "truth" model must realistically model all major error sources in the real world. Due to time and computational limitations, this research effort concentrates on the development and verification of the "truth" model for the current CIRIS system (INS/Transponders). Initial research completed on the INS/GPS/Transponder integrated model is presented in Reference (20). This goal is defined by the following objectives:

1. Design and verify the full-ordered "truth" model for the Litton LN-39 INS using a covariance analysis simulation.
2. Design a realistic measurement "truth" model for the range and range-rate transponder measurements. This model includes atmospheric and transponder correlated error sources.
3. Augment the INS and measurement models to form the overall Kalman filter "truth" model.
4. Develop the software required to allow the full-ordered Kalman filter, based on the "truth" model, to process the empirical data from a CIRIS flight tape. This CIRIS flight tape contains the CIRIS INS and measurement data available during a test flight.
5. Process the data from a typical CIRIS test flight with the full-ordered Kalman filter based on the "truth" model.

6. Perform a detailed comparison of the position error states, velocity error states, and selected transponder residuals from the current CIRIS filter and the full-ordered filter. This comparison defines the increase in accuracy possible with a higher ordered filter and serves to verify the full-ordered filter.

7. Perform a detailed analysis on the results of the correlated measurement states. The purpose of this analysis is to determine if the correlated errors are fully observable and contribute to filter error estimation.

8. Design a reduced-order filter (70 states) to reduce filter computation time while maintaining the highest level of accuracy possible. The accuracy loss is quantified by comparing the reduced-order filter data to the full-ordered filter.

Research Approach

First the INS "truth" model must be coded into the Multimode Simulation for Optimal Filter Evaluation (MSOFE) simulation package. The 85-state LN-39 "truth" model is defined in a Litton engineering analysis report (21). This report also defines the INS error growth statistics using a 10-run Monte Carlo analysis for several different flight trajectories. The 10-hour static and 2-hour fighter flight profiles are chosen for this INS "truth" model verification. The MSOFE covariance simulations must agree in magnitude and shape with the Litton Monte Carlo simulations for the MSOFE model to be considered correct (21).

Using MSOFE, the covariance of the INS "truth" model's stochastic differential equation is propagated over the 10-hour static flight profile; the stochastic differential equation's solution mean is considered to be zero for all covariance simulations. The 1σ error growth plots for position, velocity, and tilts are compared with the applicable Monte Carlo 1σ plots in the Litton engineering report (21).

Next, the INS "truth" model must be verified for a non-static flight profile. Using the Profile Generator (PROFGEN) simulation package, the position, velocity, and acceleration data for the Litton fighter flight profile is generated. Using the flight data

from PROFGEN and MSOFE, the covariance of the INS "truth" model's stochastic differential equation is propagated over the 2-hour flight profile. Again, the 1σ error growth plots for position, velocity, and tilts are compared with the applicable Monte Carlo 1σ plots in the Litton engineering report (21).

The transponder measurement "truth" model development follows. The correlated errors in the range measurement are modeled as a random bias for the receiver/transmitter calibration error, random biases for the transponder Defense Mapping Agency (DMA) survey data errors, and a first order Markov atmospheric error. One random bias state is required for the aircraft transponder receiver/transmitter bias, 3 states for each transponder's 3-dimensional survey error, and 1 state for each transponder's line-of-sight atmospheric error.

The CIRIS system works with a window of 5-10 transponders which it samples at a 1 Hertz (Hz) rate. Therefore, 10 sets of transponder bias/atmospheric states are required. This results in 41 additional states. The correlated error in the range-rate measurement is modeled with only a random bias error for the receiver/transmitter calibration error. This requires only 1 additional state. The overall filter "truth" model consists of 127 states (85 INS and 42 measurement).

The 127-state "truth" model is verified using actual CIRIS flight data. The necessary MSOFE modifications are made to facilitate this data processing. A direct comparison is made between the "truth" model and the current CIRIS position and velocity error state means. If the "truth" model filter is operating correctly, the "truth" model error state means fall within the 1σ bounds on the CIRIS error state means; since the current CIRIS system accuracies have been independently verified. A comparison is also made between selected transponder range and range-rate residuals. The error growth reflected in the transponder atmospheric and survey error state means and covariances is analyzed to determine if the states are fully observable and their magnitudes warrant inclusion in the "truth" model.

The final step is the design of a reduced-order Kalman filter based on this "truth" model. The reduced-order filter is required in order to reduce the computation time for a typical CIRIS flight to an acceptable level. The "truth" model states with insignificant error contribution magnitudes are deleted until the computation time is reduced to an estimated 8-12 hours of CPU time, for a 4.5 hour CIRIS flight data record, on a VAX 8650 computer system. A final comparison is made between the reduced-order filter, "truth" model filter, and the current CIRIS filter. The final analysis quantifies the differences between these models. The conclusions/recommendations are based on the results of this analysis.

Overview

Chapter 2 defines the general theory that is used throughout this research. The coordinate frames and transformations are defined. The operational concepts of current CIRIS, the Litton LN-39 INS, and Cubic transponders are described. The basic Kalman filter equations used in this research are defined. Finally, the MSOFE and PROFGEN simulation software capabilities are explained.

Chapter 3 defines the Litton LN-39 INS "truth" model. The coding of this model into MSOFE is described and the flight profiles are defined. The plots of the INS error growth for the static and fighter flight profiles are shown and compared to the Litton Monte Carlo error growth plots.

Chapter 4 defines the Cubic transponder range and range-rate measurement "truth" model. In this chapter the measurement "truth" model is augmented to the INS "truth" model and implemented in MSOFE. This full-ordered Kalman filter is used to process a CIRIS flight tape. The position and velocity error states of the "truth" model and the current CIRIS filter are compared and the differences quantified. The range and range-rate residuals for selected transponders are analyzed to determine efficiency and validity of the "truth" model. Finally, the correlated measurement error states means and covariances are analyzed to determine extent of observability, magnitude of estimated mean, and physical significance.

Chapter 5 describes the reduced-order filter model. The states considered for elimination are listed and their elimination justified. The final reduced-order filter model is implemented in MSOFE and the CIRIS flight tape processed. Finally, the position and velocity error growth plots are compared and the differences quantified for the reduced-order filter, full-ordered filter ("truth"), and the current CIRIS filter.

Chapter 6 summarizes the results and emphasizes the important aspects of this research effort. This chapter also recommends areas where future research should be directed.

II. Theory

This chapter describes the general theory that forms the basis for this research. Concepts and equations are described at the level required for this effort. Where necessary, cited references allow the reader to find more detailed information.

Reference Frames

Earth Fixed Frame. In this research it is important to relate global map coordinates (latitude, longitude, and altitude) to an earth-centered, earth-fixed (ECEF) coordinate system. Several different world geodetic systems exist to accomplish this task. The most accurate system is the World Geodetic System 1984 (WGS 84). This system is provided to the Department of Defense (DOD) by the Defense Mapping Agency. The CIRIS INS is capable of providing latitude, longitude, and altitude in the WGS 84 system. The transponder and satellite positions are also available in this system. Therefore, this is the primary system used for this research.

The WGS 84 system is an ellipsoidal model of the earth as illustrated in Figure 2-1. The parameters shown in Figure 2-1, the ellipse eccentricity, and the ellipse flattening constant are defined in Table 2-1 (8:3-10,3-11). The X' axis is parallel to the Bureau International de L'Heure (BIH) which is defined as Zero Meridian (Greenwich Meridian). The Y' axis is rotated 90° to the East along the equatorial plane. The Z' axis is parallel to the earth's spin axis and completes the right-handed, earth-fixed, orthogonal coordinate system (8:2-2). The surface of the ellipsoid is considered to be mean sea level (MSL).

Navigation Frame. The LN-39 INS implements a wander azimuth platform mechanization. This platform frame is illustrated in Figure 2-2. The orthogonal, right-handed, set of axes pointing North, West, and Up are designated N, W, and U respectively.

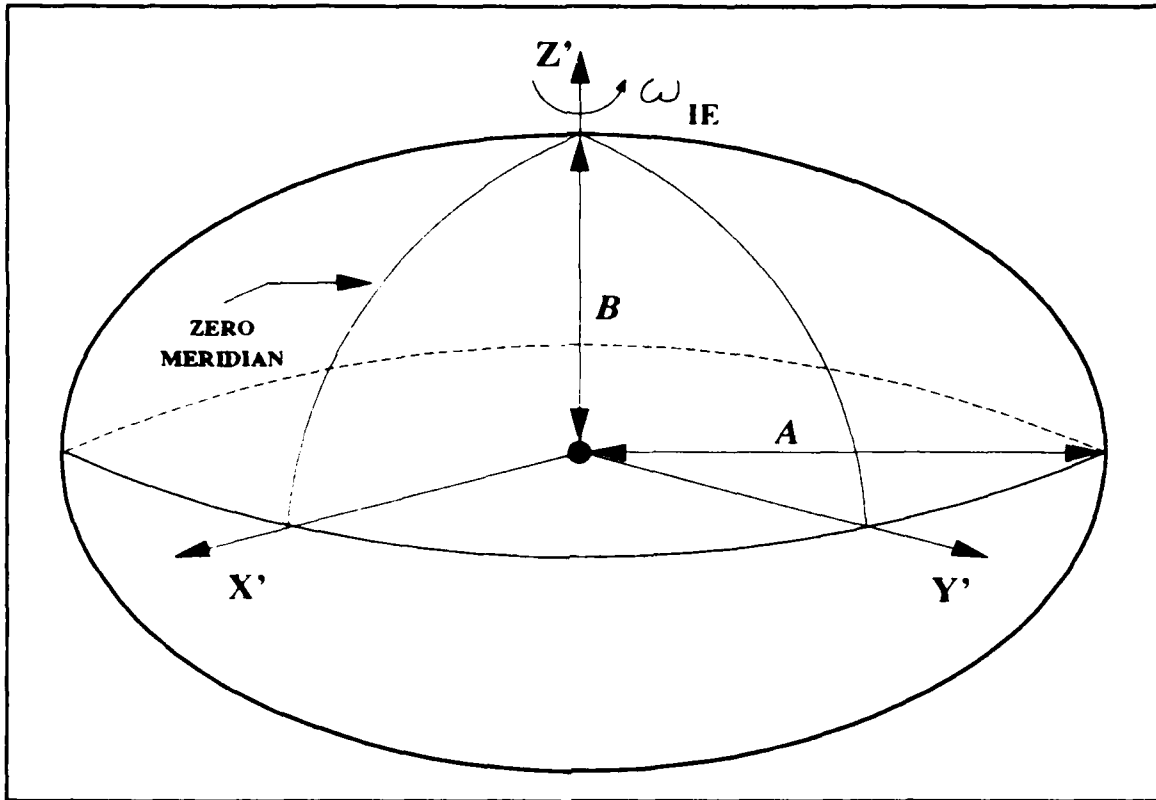


Figure 2-1. WGS 84 Ellipsoidal Model

Table 2-1
WGS 84 Constants

Parameter	Definition	Value
X',Y',Z'	ECEF Coordinate Frame Axes	none
ω_{IE}	Angular Velocity of the Earth	7.292115E-5 rad/sec
A	Semimajor Axis (Equatorial Radius)	6378137 meters ($\sigma = 2$ meters)
B	Semiminor Axis (Polar Radius)	6356752.3142 meters
e	First Eccentricity	0.0818191908426
f	Flattening (Ellipticity)	0.00335281066474
G_0	Gravity Constant	32.08744 ft/sec ²

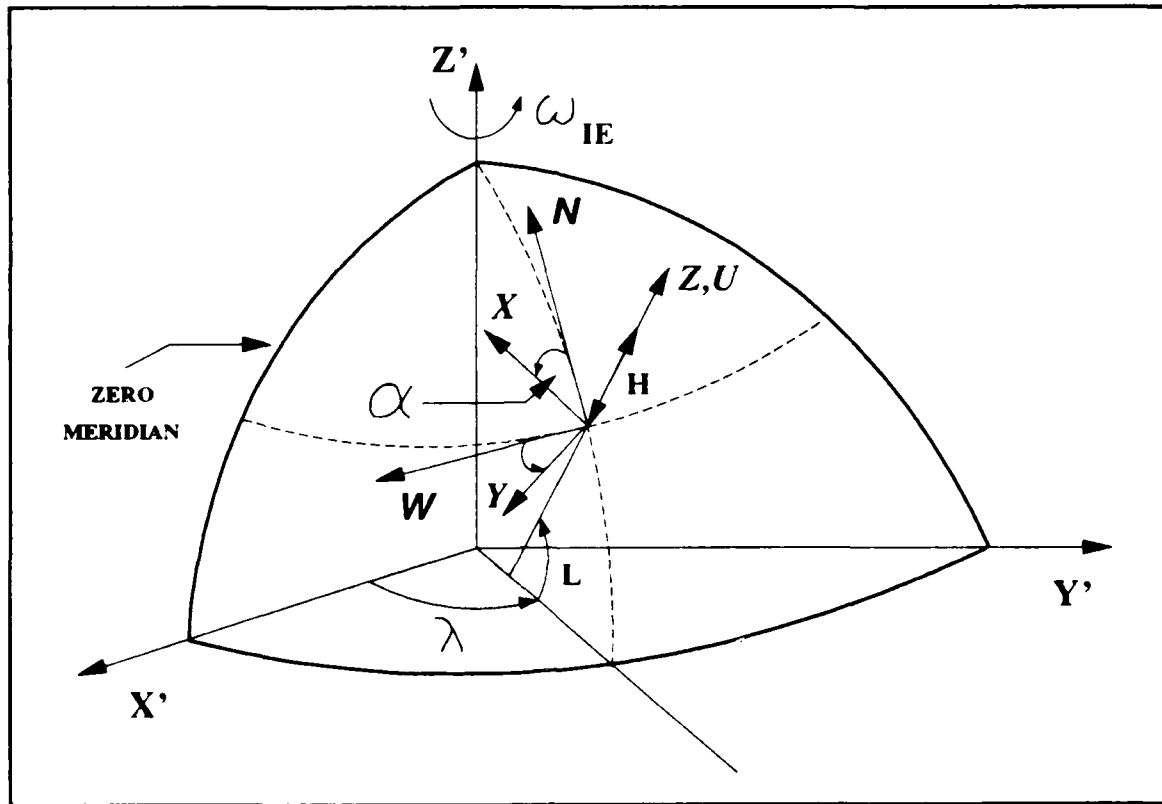


Figure 2-2. Navigation Frame

This frame is defined as the NWU navigation frame (N-Frame). The right-handed, orthogonal true reference axes (T-Frame) are designated X , Y , and Z respectively; this is also referred to as the wander azimuth frame. The wander angle (α) is considered positive when measured as a counter clockwise rotation about the Z, U axis of the true frame from the NWU navigation frame. When the wander angle is zero, the X , Y , and Z axes of the true frame are parallel to the NWU navigation frame. The geodetic latitude is represented by the variable L , the geodetic longitude by the variable λ , and the height above the reference ellipsoid by the variable H . These 3 parameters define the vehicle position in the geographically related navigation frame.

Coordinate Transformations. Coordinate transformations between frames are required in many instances throughout this thesis. The 5 frames are designated T for

true reference frame, P for the platform frame, C for computation frame, N for the NWU navigation frame, and E for the ECEF frame. The coordinatization frame of a vector is as follows:

$[X]^T$	True T-Frame
$[X]^C$	Computation C-Frame
$[X]^P$	Platform P-Frame
$[X]^N$	Navigation N-Frame
$[X]^E$	ECEF E-Frame

The true frame, platform frame, and computation frame refer to the same general coordinate frame mechanization. However, the platform and computation frames are slightly misaligned with respect to the true frame. The transformations from the true frame to the platform and computation frames are defined as (13:13-1,13-2):

$$[X]^P = [I + \phi] [X]^T \quad (2-1)$$

$$\phi = \begin{bmatrix} 0 & \phi_z & -\phi_y \\ -\phi_z & 0 & \phi_x \\ \phi_y & -\phi_x & 0 \end{bmatrix}$$

$$[X]^C = [I + \delta\Theta] [X]^T \quad (2-2)$$

$$\delta\Theta = \begin{bmatrix} 0 & \delta\theta_z & -\delta\theta_y \\ -\delta\theta_z & 0 & \delta\theta_x \\ \delta\theta_y & -\delta\theta_x & 0 \end{bmatrix}$$

The $\delta\Theta$ and ϕ variables are skew-symmetric matrices representing the small misalignment angles. This concept is used by Litton in the derivation of the INS error equations.

The majority of vectors used throughout this thesis are coordinatized in the platform frame. Therefore, to simplify notation, any vector shown without coordinatization brackets is assumed to be coordinatized in the P frame. The coordinate transformation matrices for the P, N, and E frames are now defined:

$$[X]^N = C_P^N [X]^P \quad (2-3)$$

$$C_P^N = \begin{bmatrix} \cos(\alpha) & -\sin(\alpha) & 0 \\ \sin(\alpha) & \cos(\alpha) & 0 \\ 0 & 0 & 1 \end{bmatrix} \quad (2-4)$$

$$[X]^E = C_N^E [X]^N \quad (2-5)$$

$$C_N^E = \begin{bmatrix} -\sin(L)\cos(\lambda) & \sin(\lambda) & \cos(L)\cos(\lambda) \\ -\sin(L)\sin(\lambda) & -\cos(\lambda) & \cos(L)\sin(\lambda) \\ \cos(L) & 0 & \sin(L) \end{bmatrix} \quad (2-6)$$

$$C_P^E = C_N^E C_P^N \quad (2-7)$$

$$C_P^E = \begin{bmatrix} -\sin(L)\cos(\lambda)\cos(\alpha) + \sin(\lambda)\sin(\alpha) \\ -\sin(L)\sin(\lambda)\cos(\alpha) - \cos(\lambda)\sin(\alpha) \\ \cos(L)\cos(\alpha) \\ \sin(L)\cos(\lambda)\sin(\alpha) + \sin(\lambda)\cos(\alpha) & \cos(L)\cos(\lambda) \\ \sin(L)\sin(\lambda)\sin(\alpha) - \cos(\lambda)\cos(\alpha) & \cos(L)\sin(\lambda) \\ -\cos(L)\sin(\alpha) & \sin(L) \end{bmatrix} \quad (2-8)$$

Inertial Navigation System

Hardware. The original INS used in CIRIS was the Litton LN-15. This INS has been replaced by CIGTF with the reliable and accurate Litton LN-39 standard INS. The LN-39 INS is also the standard navigation unit for the USAF F-16 fighter aircraft. This section describes the major operating characteristics of this INS.

The LN-39 is implemented in a wander-azimuth, local-level mechanization with a 4-gimbal, all-attitude platform. Vertical channel stabilization is accomplished with baro-altimeter aiding using a 3-state filter. This system is designed by Litton to meet the form, fit, and function characteristics and low life-cycle cost objectives of the USAF moderate-accuracy INS as specified in ASD/ENAC 77-1. This USAF standard INS, designated AN/ASN-141, is designed for multiple aircraft applications and worldwide operation (10:1-1).

The LN-39 INS is based on the Litton P-1000C all-attitude inertial platform, G-1200 gyros, A-1000 accelerometers, LC-4516 digital computer, and a MIL-STD-1553 data bus. This INS utilizes gyrocompass or stored heading initial alignment procedures. The user can also select from one of 11 different earth reference spheroids. In the CIRIS operational mode, the gyrocompass alignment and WGS-84 earth reference spheroid are used. In this operating mode the INS achieves accuracies of 0.8 nautical miles/hour (Circular Error Probability (CEP)), 2.5 fps 1σ horizontal velocity, and 2.0 fps 1σ vertical velocity (10:1-2,1-4,1-14).

Error Mechanization Equations. The concept of terrestrial navigation using inertial equipment involves the measurement of the specific force vector by an orthogonal triad of accelerometers. The orientation relative to the earth of the accelerometer triad is established and maintained by a stable mounting platform. This platform is instrumented with three orthogonally mounted gyroscopes whose output is used to control the attitude of the platform. The force vector due to gravity is analytically removed from the acceleration measurements to obtain the acceleration of the inertial system's center of mass, relative to inertial space. This inertial acceleration is compensated for Coriolis accelerations and earth rate, with respect to the coordinatization of the accelerometer reference frame (in this case the wander azimuth frame). Using appropriate initial conditions, these variables are integrated to obtain the inertial velocity of the system. This nonlinear vector differential equation for velocity has the form (13:13-1):

$$\underline{\dot{V}} = \underline{A} + \underline{C} - \underline{\gamma} \quad (2-9)$$

\underline{A} = Acceleration Measurements

\underline{C} = Calculated Coriolis Accelerations

$\underline{\gamma}$ = Modeled Gravity Vector

This terrestrial velocity, referenced in the inertial frame, is transformed to an earth-referenced velocity. Finally, using appropriate initial conditions, the velocity vector is integrated to obtain the system position in the geographic navigation frame. The nonlinear position equations have the form:

$$\dot{L} = -\omega_{IP_B} \quad (2-10)$$

$$\dot{\lambda} = \omega_{IP_N} \sec(L) \quad (2-11)$$

$$\dot{\alpha} = \omega_{IP_Z} - \omega_{IP_N} \tan(L) \quad (2-12)$$

$$\dot{H} = V_Z \quad (2-13)$$

$$\omega_{IP} = f(\mathbf{V})$$

The nonlinear equations defined in Eqs (2-9) through (2-13) are combined to form the describing nonlinear vector differential equation of the form:

$$\underline{\dot{X}}(t) = \underline{f}[\underline{X}(t)]$$

In order to analyze the error characteristics of these nonlinear equations, these equations are expanded in a Taylor series and truncated to first order. This forms the 9-state navigation system linearized error dynamics model. These linearized dynamics are in the standard form used by the linearized Kalman filter system model (13:13-2). The Taylor series expansion is about a nominal point. It is standard procedure in navigation applications to use the corrected INS data (corrected using Kalman filter estimated errors) as the nominal point. These quantities are defined as:

$$\hat{L} = L_{INS} - \delta\hat{L} \quad (2-14)$$

$$\hat{\lambda} = \lambda_{INS} - \delta\hat{\lambda} \quad (2-15)$$

$$\hat{H} = H_{INS} - \delta\hat{H} \quad (2-16)$$

$$\hat{\alpha} = \alpha_{INS} - \delta\hat{\alpha} \quad (2-17)$$

The "hat" designated delta variables are the respective errors estimated by the Kalman filter and the "hat" designated variables are the "best" estimate of the respective nominal or true point.

The engineers at Litton augmented the correlated error sources specific to the LN-39 INS to these linearized equations to the form the 85 state "truth" model defined in Reference (21). The details of this derivation are not presented.

Transponders

The transponder measurement system was developed by the Cubic Corporation (7). This system provides accurate line-of-sight (slant) range and range-rate measurements. The system is designated by Cubic as the Range/Range-Rate Subsystem (RRS). This section describes its major operating characteristics and accuracies.

The RRS consists of an airborne interrogator (receiver/transmitter) and ground-based transponders (receiver/transmitter). The interrogator transmits/receives carriers in the frequency bandwidth 2400-2500 MHZ. The interrogator operation is controlled by the CIRIS airborne computer. The specific transponders to be used during a flight are specified to the CIRIS computer before the flight. The CIRIS computer normally cycles through a window of 5-10 transponders at a 1 Hz rate. The transponder window is changed, as the flight progresses, by the CIRIS computer to optimize the aircraft to transponder distance.

The CIRIS computer interrogates the transponder first to verify the transponder is fully operational. Once the transponder status is verified as good, the CIRIS computer directs the RRS to lock-on to the transponder and activate the range/range-rate measurement loops (7:1).

Range Measurement. A frequency synthesizer in the interrogator generates the range modulation and transmits it on the primary carrier to the transponder. It is re-transmitted by the transponder back to the interrogator receiver. The round-trip phase delay is measured and converted to range.

The range measurement is based upon the principle that sine wave modulation on a radio frequency (RF) carrier, propagated through free space. It undergoes a phase shift directly proportional to the distance traveled. This phase shift is independent of carrier frequency and can be measured by means of an electronic phase-meter. For nonambiguous measurements, the modulation wavelength must be long enough so that the largest measurable delay (one-half wavelength) corresponds to a large range increment. However, for good resolution, a short wavelength is needed so the smallest measurable phase delay corresponds to a small increment of range. In the RRS, four harmonically related frequencies (tones) are used. The four frequencies are required to allow the system to measure the maximum range required by CIRIS with a resolution of 1 ft. The frequencies and their characteristics are shown in Table 2-2.

The actual transmission method for these frequencies and the calculation of the range magnitude is beyond the scope of this section, but further detail can be found in Reference (7). Range is measured from 200 ft to 200 miles with an overall accuracy of 3 ft 1σ (7:1,43,44).

Table 2-2
Range Measurement Frequencies

Designation	Frequency (KHZ)	Half Wavelength (ft)	Resolution (ft)
Fine	240.053	2,048	1
Intermediate	30.007	16,384	8
Coarse	3.751	131,072	64
Very Coarse	0.469	1,048,576	512

Range-Rate Measurement. An oscillator in the interrogator generates the range-rate reference frequency and transmits it on the primary carrier to the transponder. It is retransmitted by the transponder back to the interrogator receiver. The round-trip doppler shift is measured and converted to range-rate.

The actual transmission method for this frequency and the calculation of the range-rate magnitude is beyond the scope of this section, but further detail can be found in reference (7). Range-rate is measured from -5000 fps to +5000 fps with range accelerations from -1000 fps² to +1000 fps². The overall accuracy is 0.03 fps 1σ (7:1,43).

Current CIRIS Filter Model

This section describes the major characteristics of the current CIRIS filter model. The 11-state filter model is described by the stochastic error differential equation shown in Eq (2-18).

$$\begin{aligned} \delta\dot{\underline{X}}(t) &= \underline{F}(t) \delta\underline{X}(t) + \underline{W}(t) & (2-18) \\ E\{\underline{W}(t)\} &= \underline{0} \\ E\{\underline{W}(t)\underline{W}(t+\tau)\} &= \underline{Q}(t) \delta(\tau) \end{aligned}$$

The error state vector is defined as:

$$\delta\underline{X} = \begin{bmatrix} \delta L \\ \delta \lambda \\ \delta H \\ \phi_N \\ \phi_E \\ \phi_Z \\ \delta V_N \\ \delta V_E \\ \delta V_Z \\ \delta H_B \\ \delta A_Z \end{bmatrix} = \begin{bmatrix} \text{Latitude Error} \\ \text{Longitude Error} \\ \text{Altitude Error} \\ \text{North Tilt} \\ \text{East Tilt} \\ \text{Vertical Tilt} \\ \text{North Velocity Error} \\ \text{East Velocity Error} \\ \text{Vertical Velocity Error} \\ \text{Baro Altimeter Error} \\ \text{Vertical Acceleration Error} \end{bmatrix}$$

The measurement equation is defined in Eq (2-19). The index $k=1$ for the range measurement and $k=2$ for the delta-range measurement. In this research these two measurements are considered to completely uncorrelated in time. Therefore the cross correlation elements in the defining 2×2 noise strength matrix are zero and the scalar R values defined in Eq (2-19) represent the diagonal elements of this matrix. The delta-range measurement is equal to the change in the range measurement (ft) over the time of the measurement cycle. The time of the measurement cycle normally ranges from 100 to 900 milliseconds.

$$\begin{aligned} \delta Z_k(t_i) &= H_k(t_i) \delta X(t_i) + V_k(t_i) & (2-19) \\ E\{V_k(t_i)\} &= 0 \\ E\{V_k(t_i) V_k(t_j)\} &= \begin{cases} R_k(t_i) & t_i = t_j \\ 0 & t_i \neq t_j \end{cases} \end{aligned}$$

The actual structure of these equations are beyond the scope of this section, but further information can be found in Reference (14).

It is important to note how the time correlated INS and measurement errors are taken into account in the filter error estimates. The current CIRIS model is limited to the standard INS position, velocity, tilt, and vertical channel aiding error states. The correlated INS errors such as gyro drift rate, gyro bias, accelerometer bias, etc., are not modeled. The correlated measurement errors such as transponder survey errors, atmospheric errors, and transponder interrogator calibration errors are not modeled. However, these errors are compensated in the model by using time varying noise strengths (R and Q). The system noise strength (Q) is varied to compensate for INS gyro and accelerometer correlated errors. The measurement noise strength (R) is varied to compensate for transponder survey, atmospheric errors and transponder interrogator calibration errors. The filter uses a complex algorithm based on different parameters such as INS velocity, accelerations, and range to the transponder. The details of this algorithm are described in Reference (14).

An additional open loop deterministic correction is made to the line-of-sight range measurement data before it is processed by the filter. This correction is shown in Eq (2-20).

$$R_M = R'_M - e_R \quad (2-20)$$

R_M = Corrected Range Measurement

R'_M = Raw Range Measurement

e_R = Error Due To Atmospheric Effects

The atmospheric error (e_R) is attributed entirely to the non-zero refractivity of the troposphere. The troposphere is defined as the region of the atmosphere from sea-level to about 70,000 ft. The refractivity (N) is a function of the atmospheric index of refraction (n) defined in Eq (2-21). A non-zero refractivity (N) indicates an index of refraction (n) greater than 1 and a decrease in the electromagnetic wave propagation velocity (v) from the speed of light (c). This decrease in velocity results in an erroneous increase in the line-of-sight range measurement. The basic equation is shown in Eq (2-22) (14:6.3-1,6.3-3):

$$N = (1-n) \times 10^6 \quad (2-21)$$

$$v = \frac{1}{n} c \quad (2-22)$$

The refractivity is a time varying quantity based on the atmospheric temperature (T), water vapor content (e), and atmospheric pressure (P). This quantity is defined by Eq (2-23) (14:6.3-4):

$$N = \frac{77.6 P(t)}{T(t)} + \frac{37,300 e(t)}{T(t)^2} \quad (2-23)$$

The refractivity at sea level, N_s , is assigned a nominal value of 330. In the CIRIS filter, the refractivity above sea level is approximated with an exponential function based on altitude above sea level (H), atmospheric scale factor (H_s), and sea level refractivity (N_s). This equation is shown in Eq (2-24) (14:6.3-4).

$$N = N_s e^{\frac{h}{H_s}} \quad (2-24)$$

The CIRIS range correction (e_R) is calculated based on a complicated function relating refractivity, altitude, and length of measurement cycle. This algorithm is beyond the scope of this description, but can be found in Reference (14:6.3-14,6.3-15).

This section outlines the correlated error compensation in the current CIRIS filter. The open-loop corrections can be improved through the modeling of the uncompensated correlated errors with stochastic shaping filters and allowing the Kalman filter to estimate these errors. This idea is explored in later sections and implemented in the CIRIS "truth" model developed in Chapter 4.

Kalman Filter Equations

The Kalman filter propagation and update equations are implemented in the MSOFE simulation software described in the next section. The stochastic differential equation, measurement equations, and residual equations must be defined to setup the Kalman filter equations. In this section the form and notation used in the Kalman filter equations are defined.

The stochastic differential equation must be defined first. The form of this equation follows.

$$\delta \dot{\underline{X}}(t) = \underline{F}(t) \delta \underline{X}(t) + \underline{W}(t) \quad (2-25)$$

$$E\{\underline{W}(t)\} = \underline{0} \quad (2-26)$$

$$E\{\underline{W}(t) \underline{W}^T(t+\tau)\} = \underline{Q}(t) \delta(\tau) \quad (2-27)$$

The states in a navigation stochastic differential equation are error states. Error states ($\delta \underline{X}(t)$) represent the difference between the true and the INS indicated states. Therefore, the vector of states is represented by the $\delta \underline{X}$ notation and the rate of change of the vector of states by the $\delta \dot{\underline{X}}$ notation. The filter structure defined in this way is commonly referred to as a linearized Kalman filter, where the $\underline{F}(t)$ matrix represents the linearization of the error dynamics about the nominal state.

The linearized Kalman filter estimate of the error states defined in Eq (2-25) is defined by a conditional mean, Eq (2-28), and a conditional covariance matrix, Eq (2-29).

$$E\{\delta\underline{X}(t) | \delta Z\} = \delta\underline{\hat{X}}(t) \quad (2-28)$$

$$E\{[\delta\underline{X}(t) - \delta\underline{\hat{X}}(t)] [\delta\underline{X}(t) - \delta\underline{\hat{X}}(t)]^T | \delta Z\} = P(t) \quad (2-29)$$

The expected value of $\delta\underline{X}$ is the conditional mean of the error state ($\delta\underline{\hat{X}}$) and the conditional covariance of $\delta\underline{X}$ is represented by P . P is a positive semidefinite $n \times n$ matrix (n =number of states) that represents the statistical accuracy of the estimate. The square root of each diagonal element of P is considered the standard deviation (1σ value) of the associated error state estimate.

$$\text{Mean} = \delta\underline{\hat{X}}_i \quad (2-30)$$

$$\text{Standard Deviation} = 1 \sigma_i = \sqrt{P_{ii}} \quad (2-31)$$

$$i = 1, \dots, n$$

$F(t)$ is an $n \times n$ matrix that represents the linearized model system dynamics. \underline{W} is a gaussian, "white" noise vector with a mean of $\underline{0}$, Eq (2-26), and a noise strength of Q , Eq (2-27); Q is a positive semidefinite $n \times n$ matrix of noise strengths (16:275).

The measurement equation is defined next. The form of this equation follows.

$$\delta Z_k(t_i) = H_k(t_i) \delta\underline{X}(t_i) + V_k(t_i) \quad (2-32)$$

$$E\{V_k(t_i)\} = 0 \quad (2-33)$$

$$E\{V_k(t_i) V_k(t_j)\} = \begin{cases} R_k(t_i) & t_i = t_j \\ 0 & t_i \neq t_j \end{cases} \quad (2-34)$$

Since the stochastic differential equation is defined in error space, the measurement equation is also defined in error space. δZ represents the error in the measurement that the Kalman filter is estimating. H is $1 \times n$ measurement gradient matrix. V is a Gaussian, "white" noise with a mean of 0 , Eq (2-33), and a noise variance of R , Eq (2-34); R is a positive definite scalar noise strength. The measurement equation is a scalar equation and k ranges from 1 to the maximum number of different measurement types (16:275).

The Kalman filter propagation equations are defined here. The continuous time form of the equations follows (16:275).

$$\underline{\delta\hat{X}}(t/t_{i-1}) = F(t) \underline{\delta\hat{X}}(t/t_{i-1}) \quad (2-35)$$

$$\dot{P}(t/t_{i-1}) = F(t) P(t/t_{i-1}) + P(t/t_{i-1}) F^T(t) + Q(t) \quad (2-36)$$

The integration is started from the initial conditions:

$$\underline{\delta\hat{X}}(t_0) = \underline{\delta\hat{X}}_0$$

$$P(t_0) = P_0$$

After the first integration, the Kalman filter mean and covariance propagation equations use the filter's last updated mean and covariance as initial conditions on the integration performed to propagate the filter statistics to the next update point (16:275). These propagation equations are integrated in MSOFE using a Kutta-Merson integration algorithm (2).

The Kalman filter update equations are defined next. The standard form of these equations follow (16:275).

$$\underline{K}(t_i) = P(t_i^-) H^T(t_i) [H(t_i) P(t_i^-) H^T(t_i) + R(t_i)]^{-1} \quad (2-37)$$

$$\underline{\delta\hat{X}}(t_i^+) = \underline{\delta\hat{X}}(t_i^-) + \underline{K}(t_i) [\delta Z_k(t_i) - H(t_i) \underline{\delta\hat{X}}(t_i^-)] \quad (2-38)$$

$$P(t_i^-) = P(t_i^-) - \underline{K}(t_i) H(t_i) P(t_i^-) \quad (2-39)$$

To increase numerical precision, these update equations are implemented in the U-D covariance factorization form. To start the algorithm P_0 must be converted into its U-D factors. The U-D factorization of P and the factorization equations are defined as (16:392):

$$P = U D U^T \quad (2-40)$$

For the n-th column:

$$D_{nn} = P_{nn}$$

$$U_{in} = \begin{cases} 1 & i = n \\ \frac{P_{in}}{D_{nn}} & i = n-1, n-2, \dots, 1 \end{cases} \quad (2-41)$$

Then for the remaining columns, for $j=n-1, n-2, \dots, 1$, compute:

$$D_{jj} = P_{jj} - \sum_{k=j+1}^n D_{kk} U_{jk}^2$$

$$U_{ij} = \begin{cases} 0 & i > j \\ 1 & i = j \\ \frac{[P_{ij} - \sum_{k=j+1}^n D_{kk} U_{ik} U_{jk}]}{D_{jj}} & i = j-1, j-2, \dots, 1 \end{cases} \quad (2-42)$$

The scalar measurement update for the U-D covariance factorized filter is defined as (16:394):

$$\begin{aligned} \underline{f} &= \mathbf{U}^T(t_i^-) \mathbf{H}^T(t_i) \\ v_j &= D_{jj}(t_i^-) f_j \quad j = 1, 2, \dots, n \\ a_0 &= R(t_i) \end{aligned} \quad (2-43)$$

Then, for $k=1, 2, \dots, n$, calculate:

$$\begin{aligned} a_k &= a_{k-1} + f_k v_k \\ D_{kk}(t_i^+) &= \frac{D_{kk}(t_i^-) a_{k-1}}{a_k} \\ b_k &\leftarrow v_k \\ p_k &= - \frac{f_k}{a_{k-1}} \\ \left. \begin{aligned} U_{jk}(t_i^+) &= U_{jk}(t_i^-) + b_j p_k \\ b_j &\leftarrow b_j + U_{jk}(t_i^-) v_k \end{aligned} \right\} j = 1, 2, \dots, (k-1) \end{aligned} \quad (2-44)$$

(the symbol \leftarrow denotes replacement by writing over) After the n iterations are complete the updated mean and covariance are calculated with:

$$\mathbf{P}(t_i^+) = \mathbf{U}(t_i^+) \mathbf{D}(t_i^+) \mathbf{U}^T(t_i^+) \quad (2-45)$$

$$\underline{\mathbf{K}}(t_i) = \frac{\mathbf{b}}{a_n} \quad (2-46)$$

$$\delta \underline{\hat{\mathbf{X}}}(t_i^+) = \delta \underline{\hat{\mathbf{X}}}(t_i^-) + \underline{\mathbf{K}}(t_i) [\delta \mathbf{Z}_k(t_i) - \mathbf{H}(t_i) \delta \underline{\hat{\mathbf{X}}}(t_i^-)] \quad (2-47)$$

Finally, the residual equation is defined in the standard form as (16:394):

$$\text{Residual} = \delta Z_k(t_i) - H(t_i) \delta \hat{X}(t_i^-) \quad (2-48)$$

Because the measurement is nonlinear, the extended Kalman filter form of the residual is used to increase the accuracy of the residual calculation. This form of the residual equation is defined as:

$$\text{Residual} = \delta Z_k(t_i) - \delta \hat{Z}_k(t_i) \quad (2-49)$$

Here $\delta \hat{Z}$ is formed based on the corrected INS and transponder data. The actual calculation of this residual is explained in Chapter 4.

Correlated Error and Residual Characteristics

The correlated measurement errors must be modeled with shaping filters and the necessary states augmented to the dynamic system model. The shaping filters required for this research are defined in this section (16:180-185).

The transponder survey errors result from limitations in the DMA geodetic survey procedure. The resulting errors are constant in time and relatively small in magnitude. In this research the survey errors are modeled for the X', Y', and Z' (E-frame) axes. The calibration error in the aircraft transponder interrogator is also constant in time and relatively small. These errors are "best" represented by a random bias (constant) shaping filter. The defining stochastic differential equation is:

$$\begin{aligned} \delta \dot{E}(t) &= 0 \\ \delta \hat{E}(t_0) &= m_0 \\ P_{\delta E}(t_0) &= P_0 \end{aligned} \quad (2-50)$$

The autocorrelation function and the power spectral density characteristics are shown in Figure 2-3 (16:183).

A line-of-sight error occurs in the range measurement due to atmospheric conditions changing the index of refraction and resulting in propagation delays. The resulting error

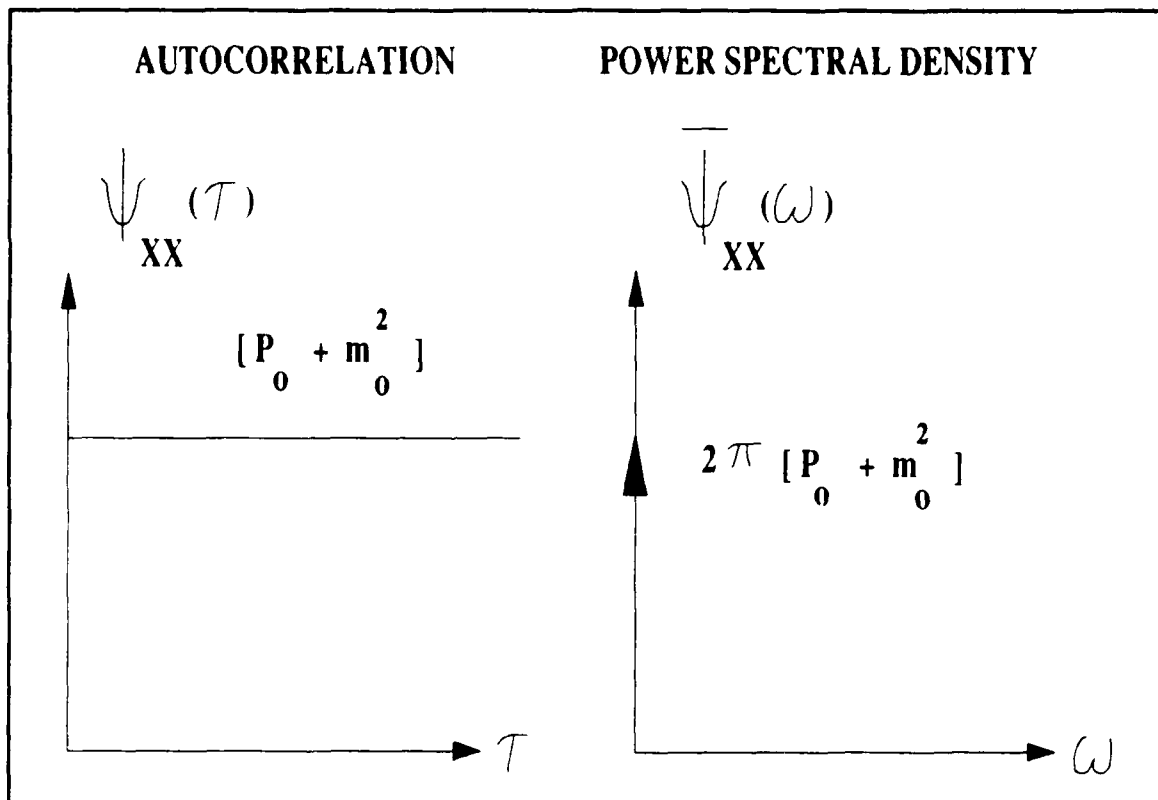


Figure 2-3. Random Bias Shaping Filter Characteristics (16:183)

is time varying and relatively small in magnitude. This error is "best" represented by a first-order Markov process shaping filter. The defining stochastic differential equation is:

$$\delta \dot{E}(t) = -\frac{1}{T} \delta E(t) + W(t) \quad (2-51)$$

$$\delta \hat{E}(t_0) = m_0$$

$$P_{\delta E}(t_0) = P_0 = \sigma^2$$

$$E\{W(t)\} = 0$$

$$E\{W(t)W(t+\tau)\} = \frac{2\sigma^2}{T} \delta(\tau) = Q \delta(\tau)$$

This is an exponentially time-correlated process. The correlation time is represented by the variable T and the initial variance by σ^2 . The autocorrelation function and power spectral density characteristics are shown in Figure 2-4.

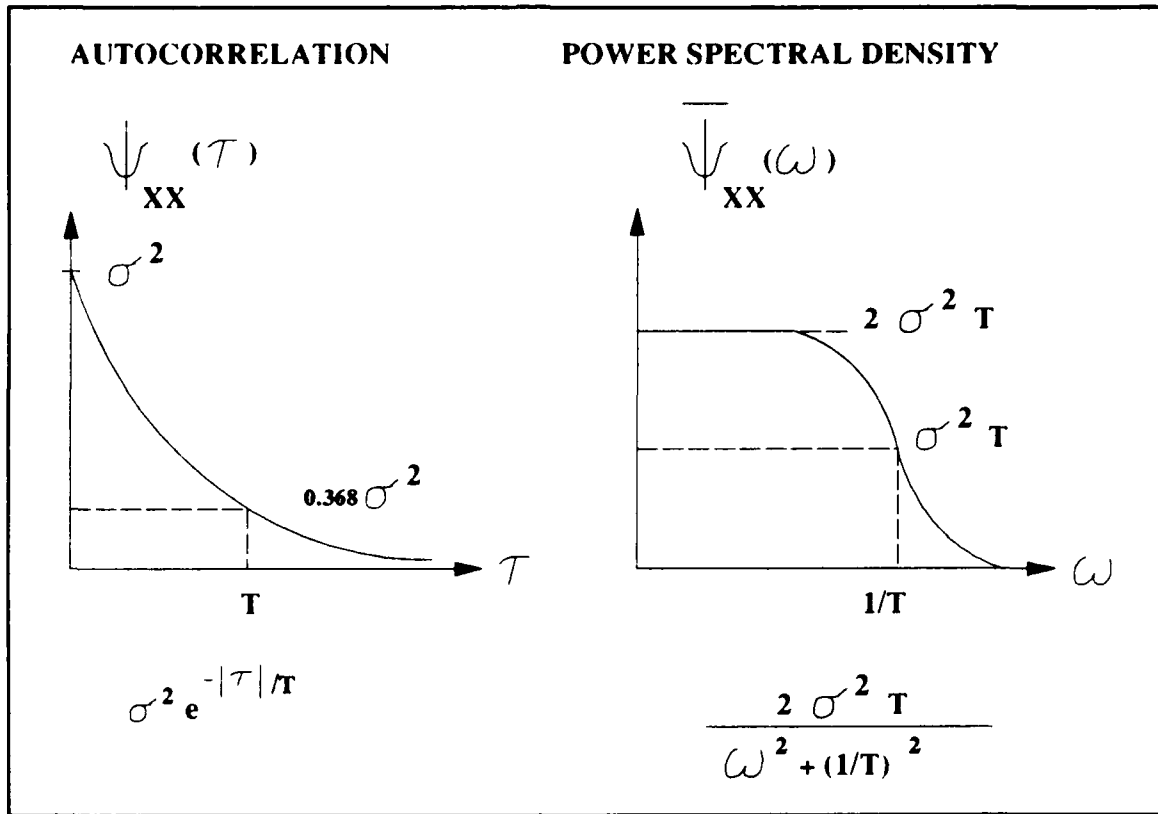


Figure 2-4. First-Order Markov Shaping Filter Characteristics (16:183)

The Kalman filter residuals are a direct indication of how well the Kalman filter model is representing the real world data. If the model perfectly matches the spectral characteristics of the real world data, the residual data process will be a "white" Gaussian sequence of mean zero and variance $H(t)P(t)H^T(t) + R(t)$. Since it is a function of the filter's covariance, it is independent of the real world measurements and can be calculated "a priori". The square root of this covariance is designated the residual 1σ value and is referred to throughout the residual analysis section in Chapter 4 (16:229).

An example of a discrete-time "white" Gaussian noise with a 1σ value of 1 is shown in Figure 2-5. In the real world a perfectly "white" residual cannot be attained. However, the closer the Kalman filter residuals are to this "white" process, with the applicable 1σ magnitude, the better the Kalman filter model.

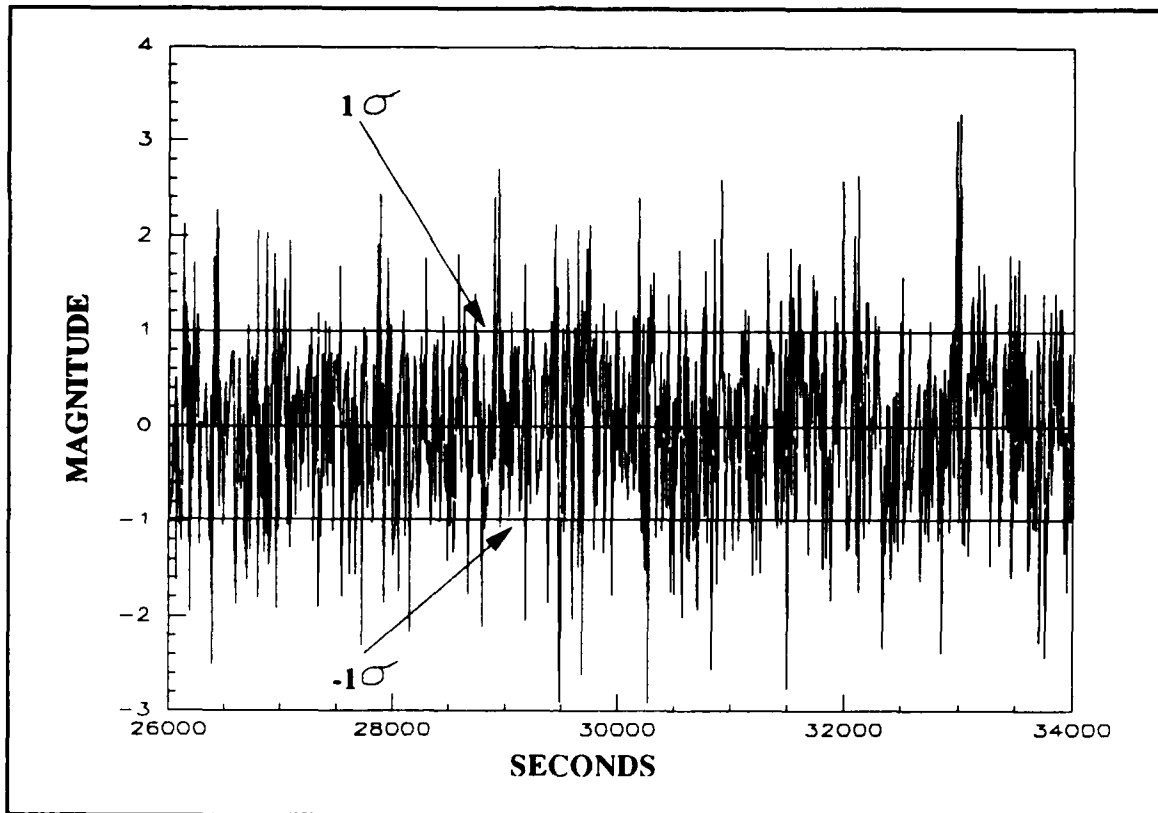


Figure 2-5. Gaussian "White" Noise

Simulation Software

Several independently developed software simulation packages are used in this research effort. All software packages are written in FORTRAN and used on a VAX 780, VAX 785, MicroVax III, or VAX 8650 Digital Equipment computer under the VMS operating system. This section describes the major characteristics of the software package and lists the respective references.

Multimode Simulation for Optimal Filter Evaluation (MSOFE). The Avionics Laboratory at Wright-Patterson AFB, OH. and Integrity Systems at Winchester, MA developed MSOFE (under contract to the Avionics Lab). It is a general purpose multimode simulation program for designing and evaluating integrated systems based on

optimal (Kalman) filtering techniques. It provides two major operation modes: Monte Carlo simulation and Covariance simulation. These two modes can be used independently or simultaneously.

The user must set up 14 FORTRAN subroutines to use the package. Basically these subroutines define the system ("truth") model, reduced order filter model, and the trajectory for the time varying stochastic differential equations. These subroutines are compiled and linked to the MSOFE main program to form the final simulation software. An MSOFE control file is read upon execution to control and set up the specifics of the user requirements for the simulation. The program outputs time histories of user selected variables (means, covariances, measurements, etc.). The specific details on how to use this package are beyond the scope of this introductory description, but can be found in Reference (5:1-1,1-2,1-4).

The research conducted in this effort concentrates on the verification of the CIRIS "truth" model. For this effort the MSOFE covariance and Monte Carlo simulation capabilities are not required. However, the MSOFE software already contains all the routines necessary to implement an extended Kalman filter with over 100 states; thus the MSOFE package is chosen for this reason. The only major modification required is to allow the filter to read measurements from an external data file; the filter model is originally set up to receive its measurements from the internal system ("truth") model.

The only other supporting software developed is a program to convert the empirical CIRIS flight tape into MSOFE trajectory and measurement data files. With these modifications, MSOFE is used to process empirical CIRIS flight tapes through a CIRIS full ordered extended Kalman filter based on the CIRIS "truth" model. This same software is also used to evaluate the reduced order CIRIS filter developed in this research.

Profile Generator (PROFGEN). The Avionics Laboratory at Wright-Patterson AFB, OH developed PROFGEN. This acronym refers to a computer program

that is capable of computing the position, velocity, acceleration, and attitude rates for a vehicle under continuous control moving over the earth's surface. This is done by solving the kinematic equations of motion appropriate for a zero-mass body responding to maneuver commands specified by the user. The user specifies a sequence of maneuvers consisting of vertical turns, horizontal turns, sinusoidal heading changes, straight flights, and rolls. The specific details on how to use this package are beyond the scope of this introductory description, but can be found in Reference (1).

It is used in this research effort to generate the fighter flight profile required for the verification of the INS "truth" model in Chapter 3. The MSOFE program is already set up to read the flight trajectory files generated by PROFGEN.

MATRIX_x. The term MATRIX_x refers to a commercial analysis and simulation package developed by Integrated Systems Inc., Palo Alto, Ca. This software package is a powerful general purpose control design/synthesis simulation package. It features a powerful matrix interpreter, a user-friendly environment with device independent graphics, state-of-the-art numerical algorithms for reliable computations, and user-transparent file management. The specific details on how to use this package are beyond the scope of this introductory description, but can be found in Reference (22:30).

It is used in this research effort for supporting matrix operations. This consisted mainly of data time history manipulations, filtering, and graphics. The Kalman filter simulation software (MSOFE) was modified to output all data in a file format readable by MATRIX_x.

Summary

This chapter develops all the general theory applicable to the following chapters in this thesis. The notation, coordinate frames, and coordinate frame transformation matrices

are developed in detail in the first section. The major operating characteristics of the CIRIS Litton LN-39 INS and its Cubic transponder system are described in the second and third sections. The Kalman filter notation and equations used are developed in detail in the fourth section. The residual and correlated error characteristics are described in section five. Finally, a brief introduction to the independently developed software simulation packages is given in section six.

The main purpose of this section is to present and explain the notation, equations, and terms used throughout this research. No attempt is made to explain all the details necessary for a complete understanding of the topic. However, appropriate references are quoted for each major topic to allow the reader to further explore the material. The additional detail required for a particular facet of this research is given in the applicable chapter.

III. INS "Truth" Model Design/Verification

This chapter describes the stochastic differential equations that define the LN-39 INS "truth" model. The equations presented are taken directly from the Litton systems engineering report (21:6-9). Minor notational changes are made to increase the clarity of certain variable names.

This "truth" model is coded into the filter differential equation routines of MSOFE. The MSOFE simulations are conducted by propagating these differential equations over different aircraft trajectories and plotting the time histories of the error state covariances. The actual error state statistics plotted are the square roots of the diagonal elements of the 85x85 error state covariance matrix. These values are referred to as the 1σ error state covariance values throughout this section.

The results of a 10-run Monte Carlo analysis for a static flight profile and a simulated fighter profile are documented in the Litton report (21:45-158). The MSOFE INS "truth" model is verified by comparing the MSOFE 1σ error state covariance value plots to the Litton report's Monte Carlo 1σ error state covariance value plots, for similar trajectories.

Error States

This LN-39 INS "truth" model consists of 85 error states. This error, 85 state vector is partitioned into 6 sub-vectors which group similar error states. The total error state vector is represented by $\delta\mathbf{X}$. The subvectors are defined as follows: $\delta\mathbf{X}_1$ contains the 13 general INS dynamics errors such as position, attitude, velocity, and vertical channel errors; $\delta\mathbf{X}_2$ contains the 10 accelerometer, gyro, and barometer correlated errors; $\delta\mathbf{X}_3$ contains the 21 gyro bias errors; $\delta\mathbf{X}_4$ contains the 29 accelerometer bias and barometer bias errors; $\delta\mathbf{X}_5$ contains the 9 accelerometer and gyro initial thermal transient errors; and $\delta\mathbf{X}_6$ contains the 3 gyro turnaround drift rate errors. The error states are all coordinatized in the P-frame and the states in each sub-vector are shown in Table 3-1.

The 85 error states and their initial 1σ error state covariance values are defined in Appendix B, Tables B-1 thru B-9. The error states of main interest, that are continuously referred to throughout this thesis, are defined here. They are the $\delta\Theta$, δH , $\delta\Phi$, and δV states. The angular error between the computer coordinate frame and the "true" coordinate frame is represented by $\delta\Theta$. The angular error between the computer calculated altitude and the "true" altitude is represented by δH . The angular error between the platform coordinate frame and the "true" coordinate frame is represented by $\delta\Phi$. The error between the computer calculated and the "true" earth referenced velocity defined in the P-Frame is represented by δV . The coordinate frames are defined in Chapter 2.

INS Stochastic Differential Equation

The INS time varying error dynamics are described by a single stochastic differential equation.

$$\delta\dot{\underline{X}}(t) = \mathbf{F}_{\text{INS}}(t) \delta\underline{X}(t) + \underline{W}(t) \quad (3-1)$$

The partitioned $\delta\underline{X}$ vector is defined in Table 3-1. In order to define the \mathbf{F}_{INS} matrix and $\delta\underline{W}$ vector, they are also partitioned into smaller submatrices (F_{ij}).

$$\delta\underline{X} = \begin{bmatrix} \delta X_1 \\ \delta X_2 \\ \delta X_3 \\ \delta X_4 \\ \delta X_5 \\ \delta X_6 \end{bmatrix} \quad (3-2)$$

$$\mathbf{F}_{\text{INS}} = \begin{bmatrix} F_{11} & F_{12} & F_{13} & F_{14} & F_{15} & F_{16} \\ 0 & F_{22} & 0 & 0 & 0 & 0 \\ 0 & 0 & 0 & 0 & 0 & 0 \\ 0 & 0 & 0 & 0 & 0 & 0 \\ 0 & 0 & 0 & 0 & F_{55} & 0 \\ 0 & 0 & 0 & 0 & 0 & F_{66} \end{bmatrix} \quad (3-3)$$

Table 3-1
Error State Partitions

δX_1	δX_2	δX_3	δX_4		δX_5	δX_6
General Errors (13)	Correlated Errors (10)	Gyro Bias Errors (9) (12)		Acc and Baro Bias Errors (12) (17)	Thermal Transients (9)	Gyro Turnaround Drift Errors (3)
$\delta\theta_x$				F_{XX}		
$\delta\theta_y$				F_{YY}		
$\delta\theta_z$				F_{ZZ}		
Φ_x	B_{XC}	B_X	N_1	Δ_{BX}	F_{XY}	
Φ_y	B_{YC}	B_Y	N_2	Δ_{BY}	F_{XZ}	
Φ_z	B_{ZC}	B_Z	N_3	Δ_{BZ}	F_{YX}	Δ_{XQ}
δV_x	Δ_{XC}	S_{GX}	H_{XX}	S_{Ax}	F_{YZ}	Δ_{YQ}
δV_y	Δ_{YC}	S_{GY}	H_{YY}	S_{Ay}	F_{ZX}	Δ_{ZQ}
δV_z	Δ_{ZC}	S_{GZ}	H_{ZZ}	S_{Az}	F_{ZY}	B_{XQ1}
δH	δG_x	X_1	H_{XY}	S_{QA_x}	μ_1	B_{XQ2}
δH_L	δG_y	X_2	H_{YX}	S_{QA_y}	μ_2	B_{YQ1}
δS_3	δG_z	X_3	H_{ZY}	S_{QA_z}	μ_3	B_{YQ2}
δS_4	δH_C		K_{XZ}	S_{Qx2}	σ_1	B_{ZQ1}
			K_{YZ}	S_{Qy2}	σ_2	B_{ZQ2}
			K_{ZX}	S_{Qz2}	σ_3	
					δH_B	B_{XTA}
					δH_{SF}	B_{YTA}
						B_{ZTA}

Note: See Appendix B-1 thru B-9 for individual element definitions.

$$\underline{W} = \begin{bmatrix} \underline{W}_1 \\ \underline{W}_2 \\ 0 \\ 0 \\ 0 \\ 0 \end{bmatrix} \quad (3-4)$$

In order to solve this differential equation, the initial conditions on $\underline{\delta\hat{X}}$ and the initial driving noise strength of \underline{W} must be defined. The initial conditions required are the initial error state means ($\underline{\delta\hat{X}}$), state covariance matrix (P), and the initial noise strength matrix (Q).

$$\underline{\delta\hat{X}}(t_0) = [0] \quad (3-5)$$

$$P_{\underline{\delta\hat{X}}}(t_0) = P_{INS}(t_0) = \begin{bmatrix} P_{11} & 0 & 0 & 0 & 0 & 0 \\ 0 & P_{22} & 0 & 0 & 0 & 0 \\ 0 & 0 & P_{33} & 0 & 0 & 0 \\ 0 & 0 & 0 & P_{44} & 0 & 0 \\ 0 & 0 & 0 & 0 & P_{55} & 0 \\ 0 & 0 & 0 & 0 & 0 & P_{66} \end{bmatrix} \quad (3-6)$$

$$E\{\underline{W}(t_0)\underline{W}(t_0+\tau)\} = Q_{INS}(t_0)\delta(\tau) = \begin{bmatrix} Q_{11} & 0 & 0 & 0 & 0 & 0 \\ 0 & Q_{22} & 0 & 0 & 0 & 0 \\ 0 & 0 & 0 & 0 & 0 & 0 \\ 0 & 0 & 0 & 0 & 0 & 0 \\ 0 & 0 & 0 & 0 & 0 & 0 \\ 0 & 0 & 0 & 0 & 0 & 0 \end{bmatrix} \delta(\tau) \quad (3-7)$$

The initial 1σ error state covariance values for the states are defined in Appendix B, Tables B-1 thru B-9. The elements of the matrices F and Q consist of many different physical variables which are defined in the next section.

Elements of the F_{INS} Matrix

The variables shown in the elements of the INS dynamics matrix, F_{INS} , (Appendix B, Tables B-12 thru B-24) are defined in this section. The parameters A , f , and G_o appear

in some of the following equations and they are defined in Chapter 2, Table 2-2. Elements of the direction cosine matrix C_P^E are also used and this matrix is defined in Chapter 2, Eq (2-8).

The wander azimuth angle (α) is used in calculating the direction cosine elements that are used in the definitions that follow. The best estimate of this angle is calculated by subtracting the filter error estimate $\delta\hat{\alpha}$ from the INS α angle:

$$\hat{\alpha} = \alpha_{INS} - \delta\hat{\alpha} \quad (3-8)$$

where:

$$\delta\hat{\alpha} = -\cos(\hat{\alpha})\tan(\hat{L})\delta\hat{\Theta}_x + \sin(\hat{\alpha})\tan(\hat{L})\delta\hat{\Theta}_y + \delta\hat{\Theta}_z \quad (3-9)$$

The best estimate of the aircraft position vector components is defined as:

$$\underline{\hat{P}} = \begin{bmatrix} L_{INS} - \delta\hat{L} \\ \lambda_{INS} - \delta\hat{\lambda} \\ H_{INS} - \delta\hat{H} \end{bmatrix} = \begin{bmatrix} \hat{L} \\ \hat{\lambda} \\ \hat{H} \end{bmatrix} \quad (3-10)$$

where:

$$\begin{bmatrix} \delta\hat{L} \\ \delta\hat{\lambda} \\ \delta\hat{H} \end{bmatrix} = \begin{bmatrix} \sin(\hat{\alpha}) & \cos(\hat{\alpha}) & 0 \\ \cos(\hat{\alpha})\sec(\hat{L}) & -\sin(\hat{\alpha})\sec(\hat{L}) & 0 \\ 0 & 0 & 1 \end{bmatrix} \begin{bmatrix} \delta\hat{\Theta}_x \\ \delta\hat{\Theta}_y \\ \delta\hat{H} \end{bmatrix} = T_e \begin{bmatrix} \delta\hat{\Theta}_x \\ \delta\hat{\Theta}_y \\ \delta\hat{H} \end{bmatrix} \quad (3-11)$$

The best estimate of the aircraft velocity vector is formed by subtracting the filter estimated velocity error from the INS velocity output, with components defined:

$$\underline{\hat{V}} = \begin{bmatrix} V_{INS_x} - \delta\hat{V}_x \\ V_{INS_y} - \delta\hat{V}_y \\ V_{INS_z} - \delta\hat{V}_z \end{bmatrix} = \begin{bmatrix} \hat{V}_x \\ \hat{V}_y \\ \hat{V}_z \end{bmatrix} \quad (3-12)$$

In the extended Kalman filter implementation, the best estimate of the position and velocity trajectory variables are formed by subtracting the filter estimate of the position/velocity errors from the INS position/velocity outputs. In the covariance analyses that follow, only the error state covariances are calculated. Therefore, the trajectory

variables cannot be corrected by the filter error estimate. However, in these simulations, the trajectory variables used are considered to be true values (without error) and do not require correction.

The best estimate of the aircraft acceleration vector components are defined as:

$$\underline{\hat{A}} = \begin{bmatrix} A_{INS_X} \\ A_{INS_Y} \\ A_{INS_Z} \end{bmatrix} = \begin{bmatrix} \hat{A}_X \\ \hat{A}_Y \\ \hat{A}_Z \end{bmatrix} \quad (3-13)$$

Since the filter is not estimating the acceleration error, the best estimate of the aircraft's acceleration vector is the INS acceleration output. The aircraft thrust acceleration value is also required and is defined as:

$$A'_Z = A_Z - G \quad (3-14)$$

where:

$$G = G_0 \left[1 - (2.00996) \frac{H}{A} + (5.28659E-3) (C_P^E\{3,3\})^2 \right] \quad (3-15)$$

The $C_P^E\{i,j\}$ notation refers to the i,j (row,column) element of the coordinate transformation matrix. The components of the earth's spheroid inverse radii of curvature are defined as:

$$[C_R]^P = \begin{bmatrix} \frac{1}{A} \left(1 - \frac{H}{A} - f \left[(C_P^E\{3,3\})^2 - 2(C_P^E\{3,1\})^2 \right] \right)^P \\ \frac{1}{A} \left(1 - \frac{H}{A} - f \left[(C_P^E\{3,3\})^2 - 2(C_P^E\{3,2\})^2 \right] \right)^P \\ \frac{2f}{A} (C_P^E\{3,1\})(C_P^E\{3,2\}) \end{bmatrix} = \begin{bmatrix} C_{RX} \\ C_{RY} \\ C_{RZ} \end{bmatrix}^P \quad (3-16)$$

Three different angular rate vectors are required. The angular rate of the E-frame with respect to the I-frame is defined as:

$$\underline{\omega}_{IE} = |\underline{\omega}_{IE}| \quad (3-17)$$

$$\underline{\omega}_{IE}^P = \begin{bmatrix} \omega_{IE} C_P^E\{3,1\} \\ \omega_{IE} C_P^E\{3,2\} \\ \omega_{IE} C_P^E\{3,3\} \end{bmatrix}^P = \begin{bmatrix} \omega_{IE X} \\ \omega_{IE Y} \\ \omega_{IE Z} \end{bmatrix}^P \quad (3-18)$$

The angular rate of the P-frame with respect to the E-frame is defined as:

$$\underline{\omega}_{EP}^P = \begin{bmatrix} -V_X C_{RZ} - V_Y C_{RY} \\ V_X C_{RX} + V_Y C_{RZ} \\ 0 \end{bmatrix}^P = \begin{bmatrix} \omega_{EPX} \\ \omega_{EPY} \\ \omega_{EPZ} \end{bmatrix}^P \quad (3-19)$$

The angular rate of the P-frame with respect to the I-frame is defined as:

$$\underline{\omega}_{IP}^P = \begin{bmatrix} \omega_{EPX} + \omega_{IE} C_P^E\{3,1\} \\ \omega_{EPY} + \omega_{IE} C_P^E\{3,2\} \\ \omega_{IE} C_P^E\{3,3\} \end{bmatrix}^P = \begin{bmatrix} \omega_{IPX} \\ \omega_{IPY} \\ \omega_{IPZ} \end{bmatrix}^P \quad (3-20)$$

The constants K_1 thru K_4 represent feedback gains in the baro-altimeter vertical channel aiding loops. They are defined as follows:

$$K_1 = \frac{3}{\lambda} \quad (3-21)$$

$$K_2 = \frac{2G_o}{A} + \frac{4}{\lambda^2} \quad (3-22)$$

$$K_3 = \frac{2}{\lambda^3} \quad (3-23)$$

$$K_4 = \frac{\Delta^2}{\Delta_o^2 + \Delta^2} \quad (3-24)$$

where:

$$\Delta = \dot{H}_{\text{BARO}}$$

$$\lambda = 100 \left[1 + \left(\frac{\Delta}{\Delta_0} \right)^2 \right]$$

$$\Delta_0 = 30 \text{ (INITIALLY)}$$

$$\Delta_0 = \begin{cases} (\Delta_0 + 8) & \text{IF } \Delta_0 \leq \Delta \\ (\Delta_0 - 8) & \text{IF } \Delta_0 > \Delta \text{ AND } \Delta_0 > 38 \\ 30 & \text{OTHERWISE} \end{cases}$$

The parameter β represents the inverse correlation time of the applicable state. They are defined as follows:

$$\begin{aligned} \beta_{\text{SH}_c} &= \frac{1}{600} \text{ SEC}^{-1} & \beta_{\text{B}_{\text{XC,YC,ZC}}} &= \frac{1}{300} \text{ SEC}^{-1} \\ \beta_{\Delta_{\text{XC,YC,ZC}}} &= \frac{1}{600} \text{ SEC}^{-1} & \beta_{\delta_{\text{G}_{\text{X,Y,Z}}}} &= \frac{|\mathbf{V}|}{121520} \text{ SEC}^{-1} \\ \beta_{\Delta_{\text{XQ,YQ,ZQ}}} &= \frac{1}{60} \text{ SEC}^{-1} & \beta_{\text{B}_{\text{XQ1,YQ1,ZQ1}}} &= \frac{1}{60} \text{ SEC}^{-1} \\ \beta_{\text{B}_{\text{XQ2,YQ2,ZQ2}}} &= \frac{1}{140} \text{ SEC}^{-1} & & \end{aligned}$$

where:

$$|\mathbf{V}| = \sqrt{V_x^2 + V_y^2 + V_z^2}$$

Elements of the Q matrix

The variables shown in the elements of the Q matrix (Appendix B, Tables 10 thru 11) are defined in this section. The β parameters shown in these elements are defined in the previous section. The σ values are defined as follows:

$$\begin{aligned} \sigma_{\delta H_c} &= 100\text{ft} & \sigma_{B_{Xc,Yc}} &= 0.002 \frac{\text{deg}}{\text{hr}} \\ \sigma_{B_{Zc}} &= 0.005 \frac{\text{deg}}{\text{hr}} & \sigma_{\Delta_{Xc,Yc,Zc}} &= 3 \mu\text{g} \\ \sigma_{\eta_{B_{X,Y,Z}}} &= 0.003 \frac{\text{deg}}{\text{hr}} & \sigma_{\eta_{A_{X,Y,Z}}} &= 5 \mu\text{g} \end{aligned}$$

Alignment Simulation

The INS always undergoes an 8-10 minute gyrocompass alignment before being placed in the navigation mode. This alignment process must be simulated before any navigation simulations can be run. The Litton engineer responsible for the Litton INS Monte Carlo simulations advised that the best way to simulate this alignment process is to use a Kalman filter to update the INS with zero velocity measurements (2).

To accomplish this simulation, the measurement update routines in MSOFE are used. The true trajectory variables L , λ , H , V_x , V_y , V_z , A_x , A_y , and A_z are constants and set to 32.8 deg North, 106 deg West, 4200 ft, 0, 0, 0, 0, 0, and 32.08744 fps^2 respectively. The alignment simulation uses two velocity error measurements and the INS is updated every two seconds for 10 minutes. The first scalar measurement is the V_x velocity error. The H matrix (1 X 85) and value of the measurement noise R (1 X 1) are defined:

$$H_{V_x} = [0 \ 0 \ 0 \ 0 \ 0 \ 0 \ 0 \ 1 \ 0 \ \dots \ 0] \quad (3-25)$$

$$R_{V_x} = 0.02 \frac{\text{ft}^2}{\text{sec}^2} \quad (3-26)$$

The second scalar measurement is the V_y velocity error. The 1 X 85 H matrix and the value of the measurement noise 1 X 1 R matrix are defined:

$$H_{V_y} = [0 \ 0 \ 0 \ 0 \ 0 \ 0 \ 0 \ 0 \ 1 \ 0 \ \dots \ 0] \quad (3-27)$$

$$R_{V_y} = 0.02 \frac{\text{ft}^2}{\text{sec}^2} \quad (3-28)$$

A covariance analysis is conducted using these measurements for a 10 minute period. The resulting 1σ error state covariance values for the latitude, longitude, altitude, North tilt, East tilt, azimuth tilt, North velocity, East velocity, and vertical velocity error states are plotted in Figure 3-1.

In order to obtain the latitude and longitude errors in feet, the following transformation is used (3:48,94):

$$\mathbf{P}^N = \mathbf{T}_f \mathbf{P}^C \mathbf{T}_f^T \quad (3-29)$$

where:

$$\mathbf{P}^C = \begin{bmatrix} P_{INS}\{1,1\} & P_{INS}\{1,2\} \\ P_{INS}\{2,1\} & P_{INS}\{2,2\} \end{bmatrix}$$

$$\mathbf{T}_f = \begin{bmatrix} R \sin(\hat{\alpha}) & R \cos(\hat{\alpha}) \\ -R \cos(\hat{\alpha}) & R \sin(\hat{\alpha}) \end{bmatrix}$$

$$R = A (1 - e \sin^2(\hat{L}))$$

The square root of the diagonal elements of the \mathbf{P}'' represent the 1σ error state covariance values of latitude and longitude in feet. To obtain the North/East tilts and velocities, the following transformation is used:

$$[\mathbf{P}]^N = \mathbf{C}_P^N \mathbf{P}^P \mathbf{C}_N^P \quad (3-30)$$

In this equation \mathbf{P} represents the applicable 2×2 submatrix of \mathbf{P}_{INS} corresponding to the X/Y tilts or velocities. The direction cosine matrix is defined in Eq (2-4).

The fully populated covariance matrix that results from this simulation is used as the initial error covariance for all navigation simulations. The off-diagonal elements of this matrix reflect the cross-correlation between the states as a result of the alignment. The main purpose of this simulation is to obtain these off-diagonal elements. Producing just the diagonal elements of the initial covariance matrix does not accurately portray the resulting alignment correlations.

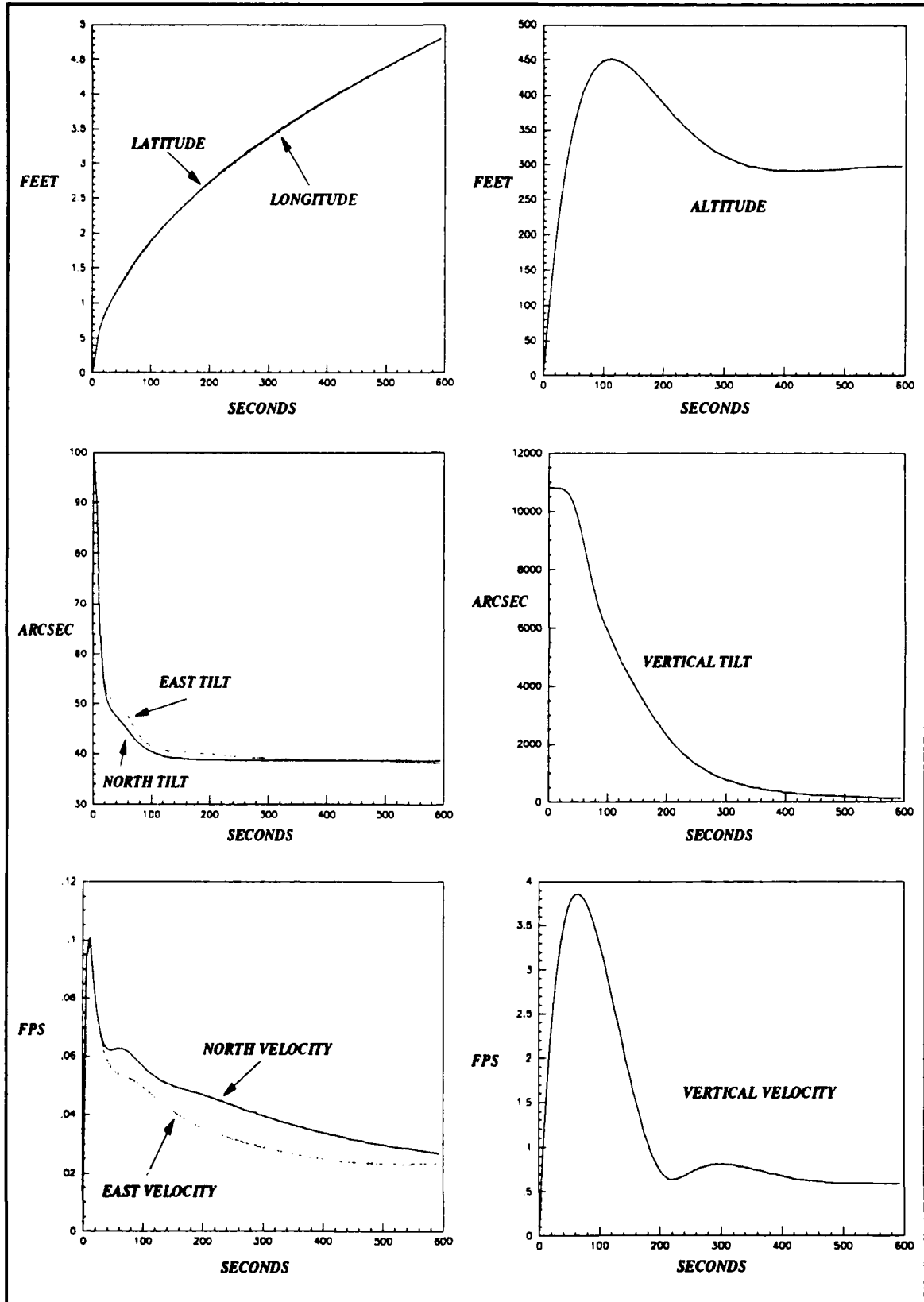


Figure 3-1. RMS Errors for Alignment Simulation

Aircraft Trajectory Simulations

A covariance analysis is conducted with the INS model using two different aircraft trajectories. In these simulations the initial covariance matrix generated by the alignment simulation is used. This simulation propagates the covariance of the error states *without* any measurement updating (deterministic baro-altimeter aiding is included in the INS model). The results of this simulation define the baseline error growth for the *unaided* INS subjected to the two respective aircraft trajectories.

Static Profile. In this simulation, the true trajectory variables L , λ , H , V_x , V_y , V_z , A_x , A_y , and A_z are constants and set to 32.8 deg North, 106 deg West, 4200 ft, 0, 0, 0, 0, 0, and 32.08744 fps^2 , respectively. MSOFE is used to propagate the stochastic differential equation over a 10 hour period. The 1σ error state covariance values of interest for this simulation are shown in Figure 3-2.

The latitude, longitude, North tilt, East tilt, North velocity, and East velocity 1σ error state covariance value plots are compared to the corresponding Litton Monte Carlo 1σ error state covariance value plots in the Litton report (21:79-82). The shape and magnitude are very similar, indicating the MSOFE INS error dynamics are properly modeled.

Fighter Profile. In this simulation, the true trajectory variables are generated using the PROFGEN trajectory simulation software. The fighter profile defined in the Litton report (21:41) is approximated as closely as possible. Due to the complexity of this profile, it could not be exactly replicated. However, it is approximated sufficiently for the INS error growth to be similar. This 2-hour fighter profile is shown in Figure 3-3.

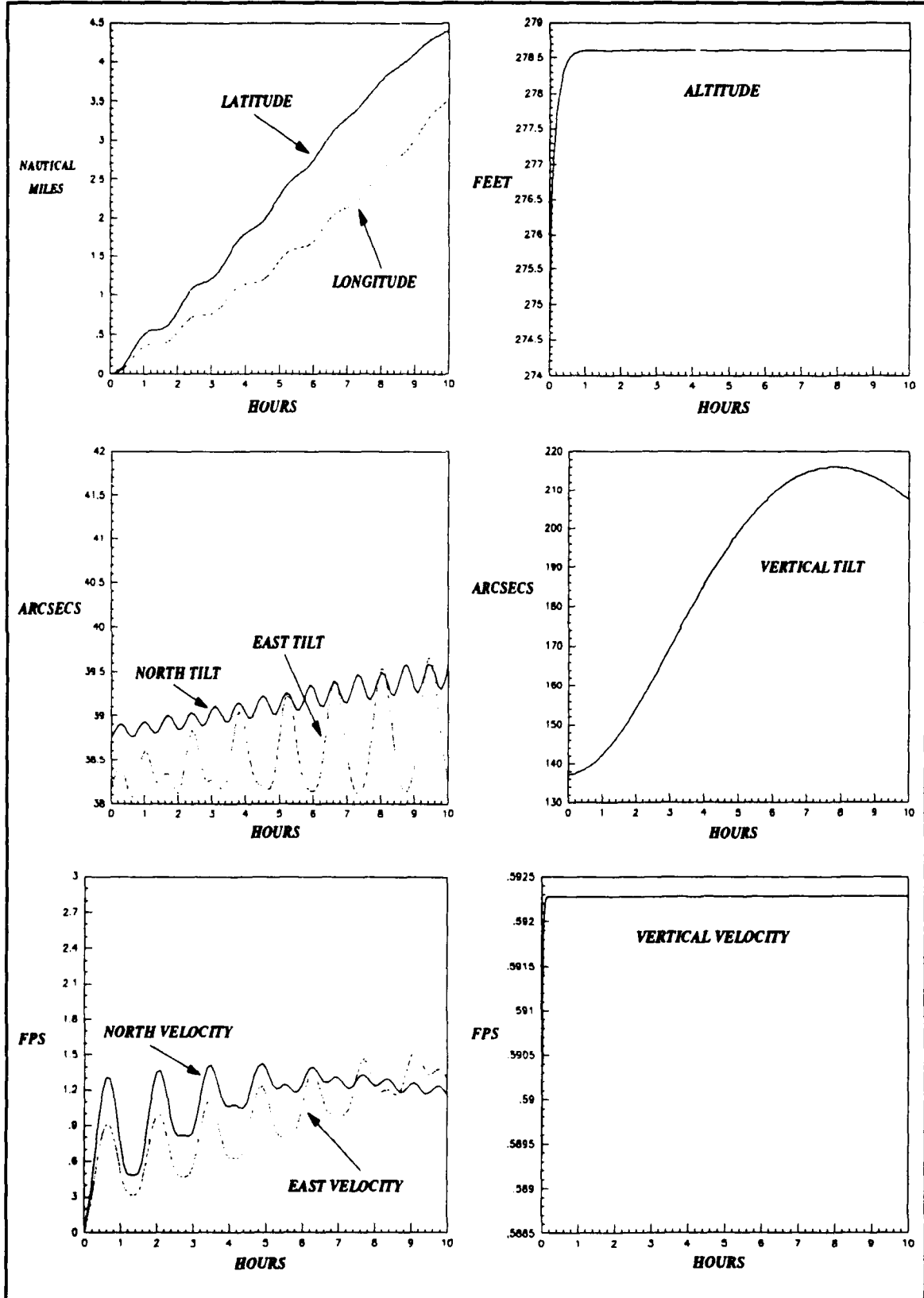


Figure 3-2. 1σ Values for the Static Simulation

The simulation software (MSOFE) is used to propagate the stochastic differential equation over the 2-hour trajectory period. The resulting 1σ error state covariance value plots are shown in Figure 3-4.

The latitude, longitude, North tilt, East tilt, North velocity, and East velocity 1σ error state covariance value plots are compared to the corresponding Litton Monte Carlo 1σ error state covariance value plots in the Litton report (21:105-108). The shapes and magnitudes are very similar, thus validating the MSOFE INS error model.

Summary

The stochastic differential equation and all associated parameters are defined in detail. The 10 minute gyrocompass alignment is simulated to generate an accurate initial covariance matrix for the navigation simulations. Finally, a MSOFE covariance simulation is conducted for the static and fighter profiles defined in the Litton report. The results of the MSOFE simulations closely agree with the Monte Carlo simulations in the Litton report. Therefore, the INS model is considered to be properly modeled and coded into MSOFE.

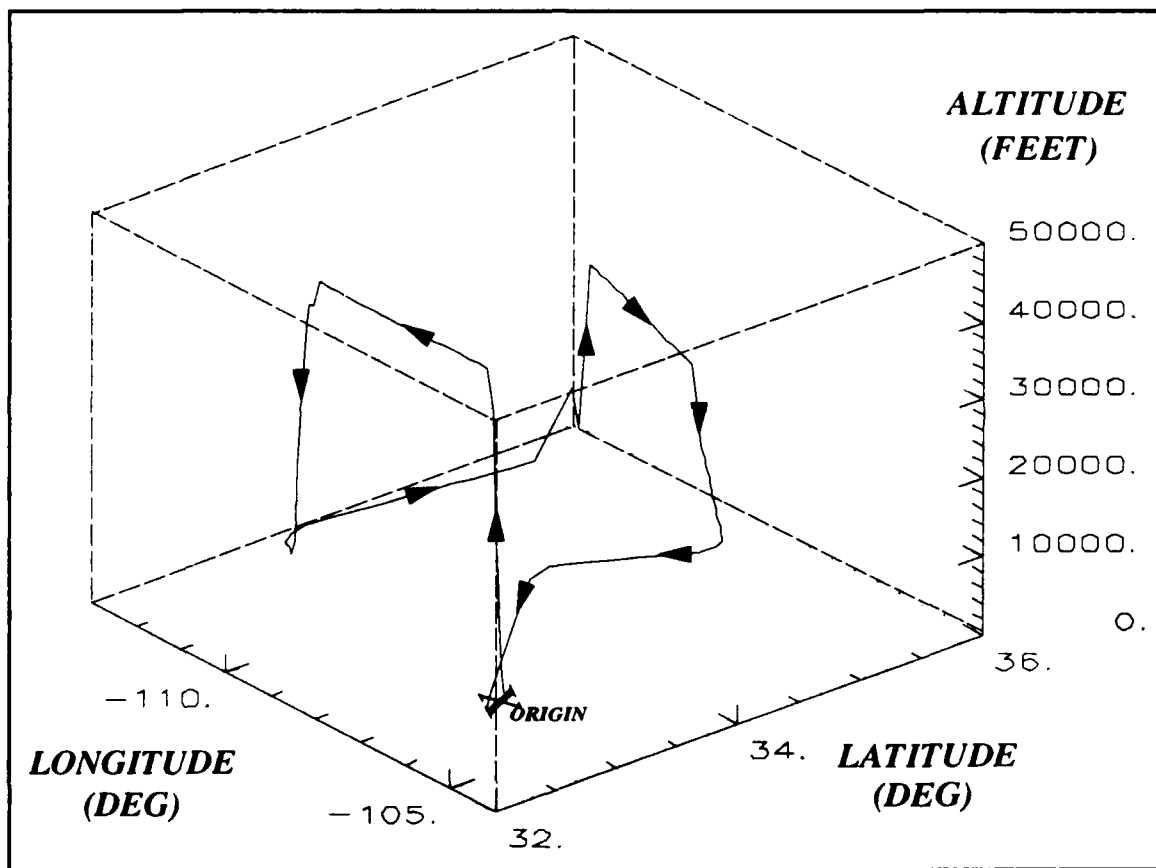


Figure 3-3. PROFGEN Fighter Profile

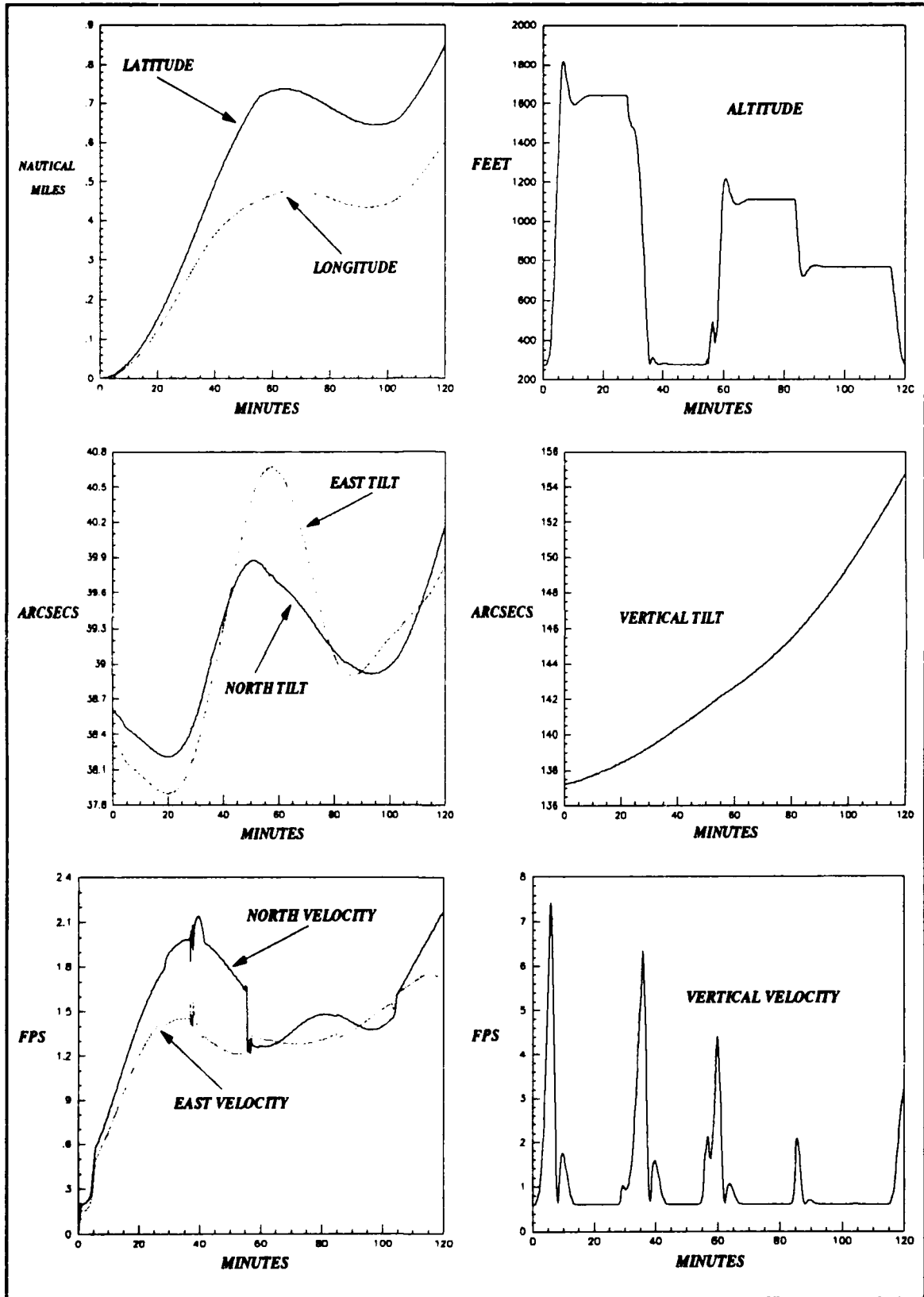


Figure 3-4. 1σ Values for the Fighter Simulation

IV. INS/Transponder "Truth" Model Design/Verification

This chapter defines the range and range-rate measurement models. It augments these models to the INS "truth" model to form the full-ordered extended Kalman filter model. The full-ordered filter is used to process empirical data from a CIRIS flight. The results of this simulation are analyzed in detail and compared to the data from the current CIRIS filter.

Range Measurement Model

Since this is a linearized Kalman filter, the measurement input to the Kalman filter is the error in the range measurement. This quantity is formed by differencing the calculated range and the range measurement available from the Cubic RRS.

The calculated range is based on the aircraft's INS position data and the transponder position data. This measurement is depicted in Figure 4-1. The INS and each ground transponder position vector are defined in the ECEF frame as follows:

$$\underline{P}_A = \begin{bmatrix} X_A \\ Y_A \\ Z_A \end{bmatrix}$$
$$\underline{P}_T = \begin{bmatrix} X_T \\ Y_T \\ Z_T \end{bmatrix}$$

The A and T subscripts indicate aircraft position and transponder position respectively.

The nonlinear range measurement based on these positions is defined as:

$$R_C(\underline{P}_A, \underline{P}_T) = |\underline{P}_T - \underline{P}_A| = \sqrt{(X_T - X_A)^2 + (Y_T - Y_A)^2 + (Z_T - Z_A)^2} \quad (4-1)$$

The equation defining the error in this measurement is obtained by performing a Taylor series expansion of Eq (4-1) about the true values. This results in:

$$R_C = R_{TRUE} + \frac{\partial R_C(P_A, P_T)}{\partial P_A} \Big|_{P_A, P_T(True)} \delta P_A + \frac{\partial R_C(P_A, P_T)}{\partial P_T} \Big|_{P_A, P_T(True)} \delta P_T + \text{H.O.T.} \quad (4-2)$$

Truncating to first order and expanding the partials results in:

$$R_C = R_{TRUE} - \frac{X_T - X_A}{R_C} \delta X_A - \frac{Y_T - Y_A}{R_C} \delta Y_A - \frac{Z_T - Z_A}{R_C} \delta Z_A + \frac{X_T - X_A}{R_C} \delta X_T + \frac{Y_T - Y_A}{R_C} \delta Y_T + \frac{Z_T - Z_A}{R_C} \delta Z_T \quad (4-3)$$

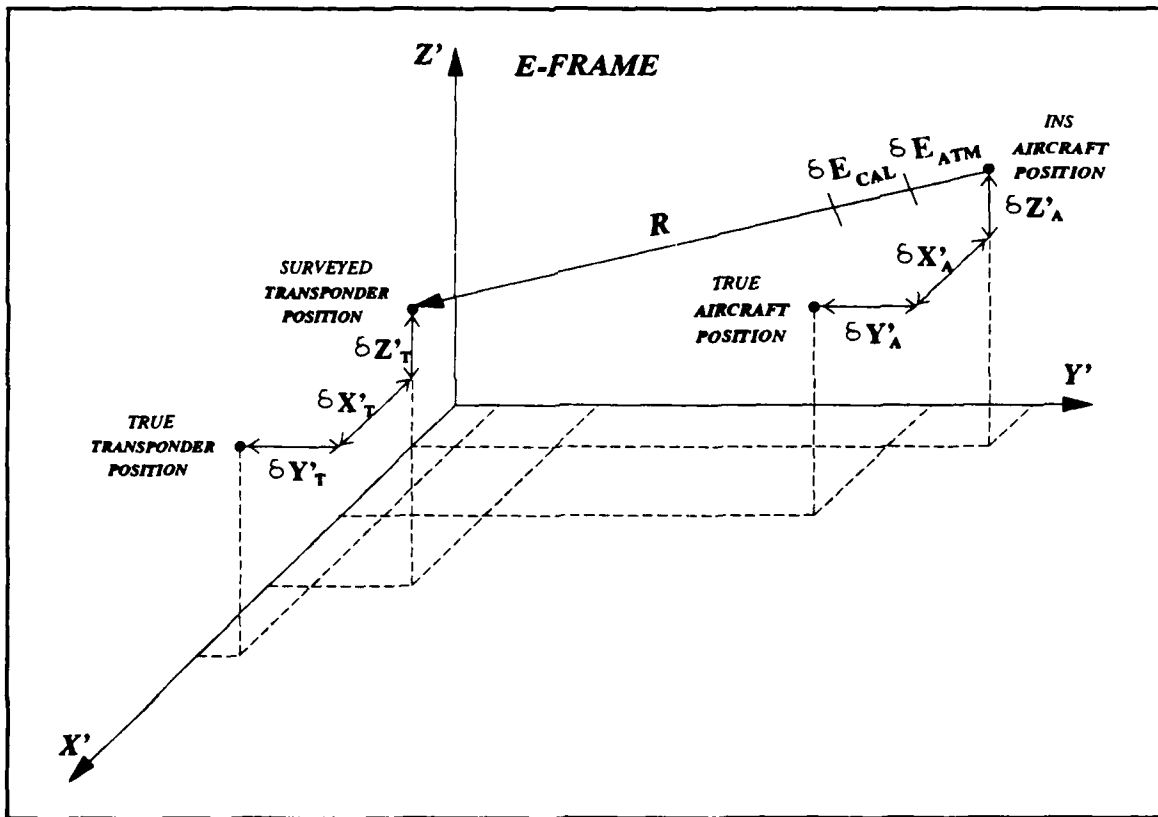


Figure 4-1. Errors in Calculated Measurement

The Cubic RRS measured range contains the true range plus an error due to a RRS calibration bias (δE_{CALR}), an error due to atmospheric propagation delays (δE_{ATM}), and a random error (V_R). This measurement is defined as:

$$R_M = R_{TRUE} + \delta E_{CALR} + \delta E_{ATM} - V_R \quad (4-4)$$

The measurement to the Kalman filter is formed by differencing R_C and R_M . This differencing cancels the true range quantity and leaves only the error which the Kalman filter is estimating. This measurement is defined as:

$$\begin{aligned} \delta Z_1 &= \delta Z_{RANGE} = R_C - R_M = \\ &- \frac{X_T - X_A}{R} \delta X_A - \frac{Y_T - Y_A}{R} \delta Y_A - \frac{Z_T - Z_A}{R} \delta Z_A \\ &+ \frac{X_T - X_A}{R} \delta X_T + \frac{Y_T - Y_A}{R} \delta Y_T + \frac{Z_T - Z_A}{R} \delta Z_T \\ &- \delta E_{CALR} - \delta E_{ATM} + V_R \end{aligned} \quad (4-5)$$

The stochastic differential equations are now developed for the errors shown in Eq (4-5) that are not already modeled in the INS "truth" model. The INS (vehicle) position errors ($\delta X_A, \delta Y_A, \delta Z_A$) are the only errors already modeled. The transponder position errors ($\delta X_T, \delta Y_T, \delta Z_T$) are modeled as random biases with an initial mean of 0 ft and initial 1σ value of 5 ft. The describing stochastic differential equation is:

$$\begin{aligned} \delta \underline{P}_T &= \begin{bmatrix} \delta X_T \\ \delta Y_T \\ \delta Z_T \end{bmatrix} \\ \delta \underline{P}_T(t) &= \underline{0} \\ \delta \underline{P}_T(t_0) &= \underline{0} \\ P_{\delta \underline{P}_T}(t_0) &= \begin{bmatrix} 25 & 0 & 0 \\ 0 & 25 & 0 \\ 0 & 0 & 25 \end{bmatrix} \end{aligned} \quad (4-6)$$

The Cubic RRS calibration error is modeled as a random bias with an initial mean of 0 ft and initial 1σ of 5 ft. The describing stochastic differential equation is:

$$\delta \dot{E}_{\text{CALR}}(t) = 0 \quad (4-7)$$

$$\delta \hat{E}_{\text{CALR}}(t_0) = 0$$

$$P_{\delta E_{\text{CALR}}}(t_0) = 1$$

The Cubic RRS atmospheric error is modeled as a first order Markov time varying error with a correlation time of 300 seconds, noise strength of 0.1667 ft²/sec, initial mean of 0 ft, and initial 1σ value of 5 ft. The correlation time for this model is derived from static testing data recorded at CIGTF. Range data was recorded between transponders separated by different distances. After removing the true range, the power spectral density (PSD) on this error data indicated an average correlation time of 300 seconds.

$$\delta \dot{E}_{\text{ATM}}(t) = -\frac{1}{300} \delta E_{\text{ATM}}(t) + W_{\text{ATM}} \quad (4-8)$$

$$\delta \hat{E}_{\text{CAL}}(t_0) = 0$$

$$P_{\delta E_{\text{CAL}}}(t_0) = 25$$

$$E\{W_{\text{ATM}}(t)\} = 0$$

$$E\{W_{\text{ATM}}(t)W_{\text{ATM}}(t+\tau)\} = 0.1667 \delta(\tau)$$

The random measurement noise (V_R) is modeled as Gaussian, "white" noise with a mean of 0 ft and a noise strength of 4 (ft)² (R_R). These models are augmented to the INS "truth" model to form the final model for the full-ordered Kalman filter. The measurement gradient matrix (H_R) is taken directly from Eq (4-5). The details of this process are shown in the "Full-Ordered Kalman Filter "Truth" Model" section that follows.

Range-Rate Measurement Model

Again, the measurement input to the linearized Kalman filter must be the error in the range-rate measurement. This quantity is formed by differencing the calculated range-rate and the range-rate measurement available from the Cubic RRS.

The calculated range-rate measurement is based on the INS position and velocity data. The nonlinear range-rate measurement equation is obtained by differentiating Eq (4-1). This results in:

$$\dot{R}_C = \frac{dR_C}{dt} = \frac{-(X_T - X_A) V_{AX} - (Y_T - Y_A) V_{AY} - (Z_T - Z_A) V_{AZ}}{R_C} \quad (4-9)$$

The nonlinear equation defining the error in this measurement is obtained by performing a Taylor series expansion on Eq (4-7). This results in:

$$\begin{aligned} \dot{R}_C = \dot{R}_{TRUE} &+ \left. \frac{\partial \dot{R}_C(P_A, V_A)}{\partial P_A} \right|_{P_A, V_A(TRUE)} \delta P_A \\ &+ \left. \frac{\partial \dot{R}_C(P_A, V_A)}{\partial V_A} \right|_{P_A, V_A(TRUE)} \delta V_A + \text{H.O.T.} \end{aligned} \quad (4-10)$$

Truncating to first order and expanding the partials results in:

$$\begin{aligned} \dot{R}_C = \dot{R}_{TRUE} & - \frac{(X_T - X_A)^2 V_{AX} + (X_T - X_A)(Y_T - Y_A) V_{AY} + (X_T - X_A)(Z_T - Z_A) V_{AZ} - V_{AX} R_C^2}{R_C^3} \delta X_A \\ & - \frac{(Y_T - Y_A)^2 V_{AY} + (Y_T - Y_A)(X_T - X_A) V_{AX} + (Y_T - Y_A)(Z_T - Z_A) V_{AZ} - V_{AY} R_C^2}{R_C^3} \delta Y_A \\ & - \frac{(Z_T - Z_A)^2 V_{AZ} + (Z_T - Z_A)(X_T - X_A) V_{AX} + (Z_T - Z_A)(Y_T - Y_A) V_{AY} - V_{AZ} R_C^2}{R_C^3} \delta Z_A \\ & - \frac{(X_T - X_A)}{R_C} \delta V_{AX} - \frac{(Y_T - Y_A)}{R_C} \delta V_{AY} - \frac{(Z_T - Z_A)}{R_C} \delta V_{AZ} \end{aligned} \quad (4-11)$$

The Cubic RRS measured range-rate contains the true range-rate, an error due to a RRS calibration bias (δE_{CAL}), and a random error (V_{RR}). This measurement is defined as:

$$\dot{R}_M = \dot{R}_{TRUE} + \delta E_{CALRR} - V_{RR} \quad (4-12)$$

The measurement to the Kalman filter is formed by differencing \dot{R}_C and \dot{R}_M . This differencing cancels the true range-rate quantity and leaves only the error which the Kalman filter estimates. This measurement is defined as:

$$\begin{aligned}
\delta Z_2 &= \delta Z_{RATE} = \dot{R}_C - \dot{R}_M = \\
&- \frac{(X_T - X_A)^2 V_{AX} + (X_T - X_A)(Y_T - Y_A) V_{AY} + (X_T - X_A)(Z_T - Z_A) V_{AZ} - V_{AX} R_C^2}{R_C^3} \delta X_A \\
&- \frac{(Y_T - Y_A)^2 V_{AY} + (Y_T - Y_A)(X_T - X_A) V_{AX} + (Y_T - Y_A)(Z_T - Z_A) V_{AZ} - V_{AY} R_C^2}{R_C^3} \delta Y_A \\
&- \frac{(Z_T - Z_A)^2 V_{AZ} + (Z_T - Z_A)(X_T - X_A) V_{AX} + (Z_T - Z_A)(Y_T - Y_A) V_{AY} - V_{AZ} R_C^2}{R_C^3} \delta Z_A \\
&- \frac{(X_T - X_A)}{R_C} \delta V_{AX} - \frac{(Y_T - Y_A)}{R_C} \delta V_{AY} - \frac{(Z_T - Z_A)}{R_C} \delta V_{AZ} \\
&- \delta E_{CALRR} + V_{RR} \tag{4-13}
\end{aligned}$$

The Cubic RRS calibration error is modeled as a random bias with an initial mean of 0 fps and initial uncertainty 1σ of .1 fps. The describing stochastic differential equation is:

$$\begin{aligned}
\delta \dot{E}_{CALRR}(t) &= 0 \tag{4-14} \\
\delta \hat{E}_{CALRR}(t_0) &= 0 \\
P_{\delta E_{CALRR}}(t_0) &= 0.01
\end{aligned}$$

The random noise (V_{RR}) is modeled as Gaussian, "white" noise with a mean of 0 fps and a noise strength of $0.09 \text{ (fps)}^2 (R_{RR})$. These models are augmented to the INS "truth" model to form the final model for the full-ordered Kalman filter. The measurement gradient matrix (H_{RR}) is taken directly from Eq (4-13). The details of this process are shown in the "Full-Ordered Kalman Filter "Truth" Model" section that follows.

Full-Ordered Kalman Filter "Truth" Model

The additional states required to model the correlated errors in the range and range-rate measurements are augmented to the INS "truth" model stochastic differential equation to form the full-ordered "truth" model stochastic differential equations. The calibration range and range-rate random biases are assumed to be in the interrogator on

the aircraft. Therefore, these errors are common to all the transponders interrogated and require only 2 states. The transponder survey errors and atmospheric error are unique to each transponder. Therefore, each transponder interrogated requires 4 unique states.

A typical CIRIS flight uses from 10 to 30 different transponders. It normally sequences through a 5-10 transponder window at a 1 Hz rate. It deletes/adds transponders to this window to optimize the transponder geometry. Providing 4 states for each transponder is computationally burdensome. To keep the computational load manageable, 4 states are provided for only 10 different transponders (maximum number possible in a window) for a total of 40 additional states. When a transponder is deleted and replaced with a new one, the four rows and columns of the covariance matrix for the respective transponder error states are set to zero. The mean for each of the respective states is set to zero when the transponder is first used in the flight. However, the algorithm saves the mean of the current transponder before switching to a new transponder and if this transponder is encountered again in the flight, it reinitializes the error state means with the saved values. The covariance diagonal element for each of the four states is reinitialized to its initial value of 25 ft². With this procedure, any number of transponders encountered during a flight are accommodated without additional states.

The 127 (85+42) state augmented stochastic differential equation is:

$$\delta \underline{\dot{X}}(t) = \underline{F}(\underline{\hat{X}}, t) \delta \underline{X}(t) + \underline{W}(t) \quad (4-15)$$

$$\underline{\delta X} = \begin{bmatrix} \underline{\delta X}_{INS} \\ \underline{\delta X}_{MEAS} \end{bmatrix} \quad \underline{F} = \begin{bmatrix} \underline{F}_{INS} & \underline{0} \\ \underline{0} & \underline{F}_{MEAS} \end{bmatrix} \quad \underline{W} = \begin{bmatrix} \underline{W}_{INS} \\ \underline{W}_{MEAS} \end{bmatrix}$$

$$\underline{\delta \hat{X}}(t_0) = \underline{0} \quad \underline{P}_{\delta \underline{X}}(t_0) = \begin{bmatrix} \underline{P}_{INS} & \underline{0} \\ \underline{0} & \underline{P}_{MEAS} \end{bmatrix}$$

$$E\{\underline{W}(t_0)\} = \underline{0}$$

$$E\{\underline{W}(t_0) \underline{W}^T(t_0 + \tau)\} = \underline{Q}(t_0) \delta(\tau) = \begin{bmatrix} \underline{Q}_{INS} & \underline{0} \\ \underline{0} & \underline{Q}_{MEAS} \end{bmatrix} \delta(\tau)$$

The variables designated INS are defined in Chapter 3. Note that the F matrix is calculated based on \hat{X} which is the best estimate of the true states. This full state vector is defined as:

$$\underline{\hat{X}} = \underline{X} - \underline{\delta X} \quad (4-16)$$

The variables subscripted "MEAS" are defined in Appendix C.

The measurement equations are defined as:

$$\delta Z_1(t_i) = \delta Z_{\text{RANGE}}(t_i) = H_R(\hat{P}_{\underline{A}}, \hat{P}_{\underline{T}}, t_i) \delta X(t_i) + V_R(t_i) \quad (4-17)$$

$$\hat{P}_{\underline{A}} = P_{\underline{A}} - \delta \hat{P}_{\underline{A}}$$

$$\hat{P}_{\underline{T}} = P_{\underline{T}} - \delta \hat{P}_{\underline{T}}$$

$$E\{V_R(t_i)\} = 0$$

$$E\{V_R(t_i) V_R(t_j)\} = \begin{cases} R_R & t_i = t_j \\ 0 & t_i \neq t_j \end{cases}$$

$$\delta Z_2(t_i) = \delta Z_{\text{RATE}}(t_i) = H_{RR}(\hat{P}_{\underline{A}}, \hat{P}_{\underline{T}}, \hat{V}_{\underline{A}}, t_i) \delta X(t_i) + V_{RR}(t_i) \quad (4-18)$$

$$\hat{V}_{\underline{A}} = V_{\underline{A}} - \delta \hat{V}_{\underline{A}}$$

$$E\{V_{RR}(t_i)\} = 0$$

$$E\{V_{RR}(t_i) V_{RR}(t_j)\} = \begin{cases} R_{RR} & t_i = t_j \\ 0 & t_i \neq t_j \end{cases}$$

Eqs (4-17) and (4-18) are scalar equations. Again note that the best estimate of the full states are used to calculate the measurement gradient matrices (H_R and H_{RR}). The H_R and H_{RR} matrices are defined in Appendix C. The Kalman filter is updated with these equations, for a single transponder, every second.

The last quantity required to execute the Kalman filter algorithm is the residual. Because the measurements are nonlinear, the extended Kalman filter form of the residual equation is used. This form is defined as:

$$RES_1(t_i) = \hat{R}_C(\hat{P}_{\underline{A}}, \hat{P}_{\underline{T}}, t_i) + \delta \hat{E}_{CALR}(t_i) + \delta \hat{E}_{ATM}(t_i) - R_M(t_i) \quad (4-19)$$

$$RES_2(t_i) = \hat{R}_C(\hat{P}_{\underline{A}}, \hat{P}_{\underline{T}}, \hat{V}_{\underline{A}}, t_i) + \delta \hat{E}_{CALRR}(t_i) - R_M(t_i) \quad (4-20)$$

The range (Eq (4-1)) and range-rate (Eq (4-9)) nonlinear equations are used with the best estimate of the full states. This form of the residual calculation takes into account the nonlinearities of the quantity and results in a better estimate of the true residual. This is in comparison with the linearized error residual update form (15)

CIRIS Flight Simulation

A CIRIS flight tape was provided by CIGTF. This data tape contains the INS position, INS velocity, baro altimeter, range measurement, and delta range measurement data for the flight. The tape also contains the error state means, error state covariances, and measurement residuals from the current CIRIS filter for this flight. The flight trajectory for this data is illustrated in Figure 4-2.

The flight is approximately 4.5 hours in length. CIRIS flight time is designated in seconds; it begins at time 26132 and ends at time 42000. Since the full-ordered filter is computationally intensive and because most of the high dynamic maneuvers occur early in the flight, only the first 2.25 hours of the flight are processed by the filter; beginning at 26132 and ending at 34000. The T=34000 point is shown in Figure 4-2. This simulation required 17 hours of CPU time on a VAX 8650 computer. The latitude vs longitude and altitude vs longitude position trajectory plots, including transponder locations, for the abbreviated CIRIS flight profile are shown in Figure 4-3.

The data from 3 transponders is selected for a detailed residual and correlated error analysis. These transponders are designated 181, 185, and 186; their locations are circled in Figure 4-3.

The INS acceleration data is not available on the CIRIS flight tape, but is required for the full-ordered Kalman filter INS error dynamics model. This data is obtained from the INS velocities using the following equations (21:34,37):

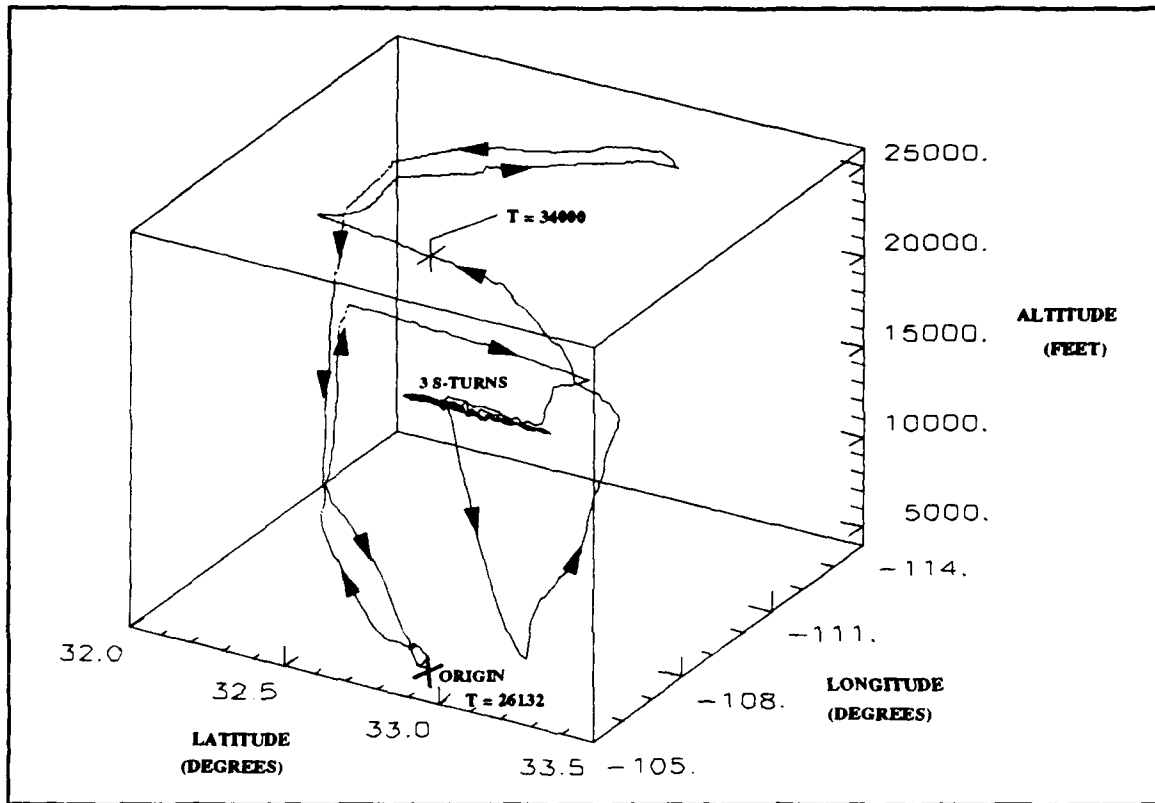


Figure 4-2. CIRIS Flight Trajectory

$$A_x = \frac{\Delta V_x}{\Delta t} + (\omega_{I_{P_Y}} + \omega_{I_{E_Y}}) V_z - (\omega_{I_{P_Z}} + \omega_{I_{E_Z}}) V_y \quad (4-21)$$

$$A_y = \frac{\Delta V_y}{\Delta t} + (\omega_{I_{P_Z}} + \omega_{I_{E_Z}}) V_x - (\omega_{I_{P_X}} + \omega_{I_{E_X}}) V_z \quad (4-22)$$

$$A_z = \frac{\Delta V_z}{\Delta t} + (\omega_{I_{P_X}} + \omega_{I_{E_X}}) V_y - (\omega_{I_{P_Y}} + \omega_{I_{E_Y}}) V_x + G \quad (4-23)$$

The full-ordered filter also requires range-rate measurement instead of the delta range measurements provides on the CIRIS flight tape. The delta range measurements are converted to range-rate measurements using the following equation:

$$\text{RANGE RATE} = \frac{\text{DELTA RANGE}}{T_M - T_R} \quad (4-24)$$

T_R = Start of Measurement Cycle

T_M = End of Measurement Cycle

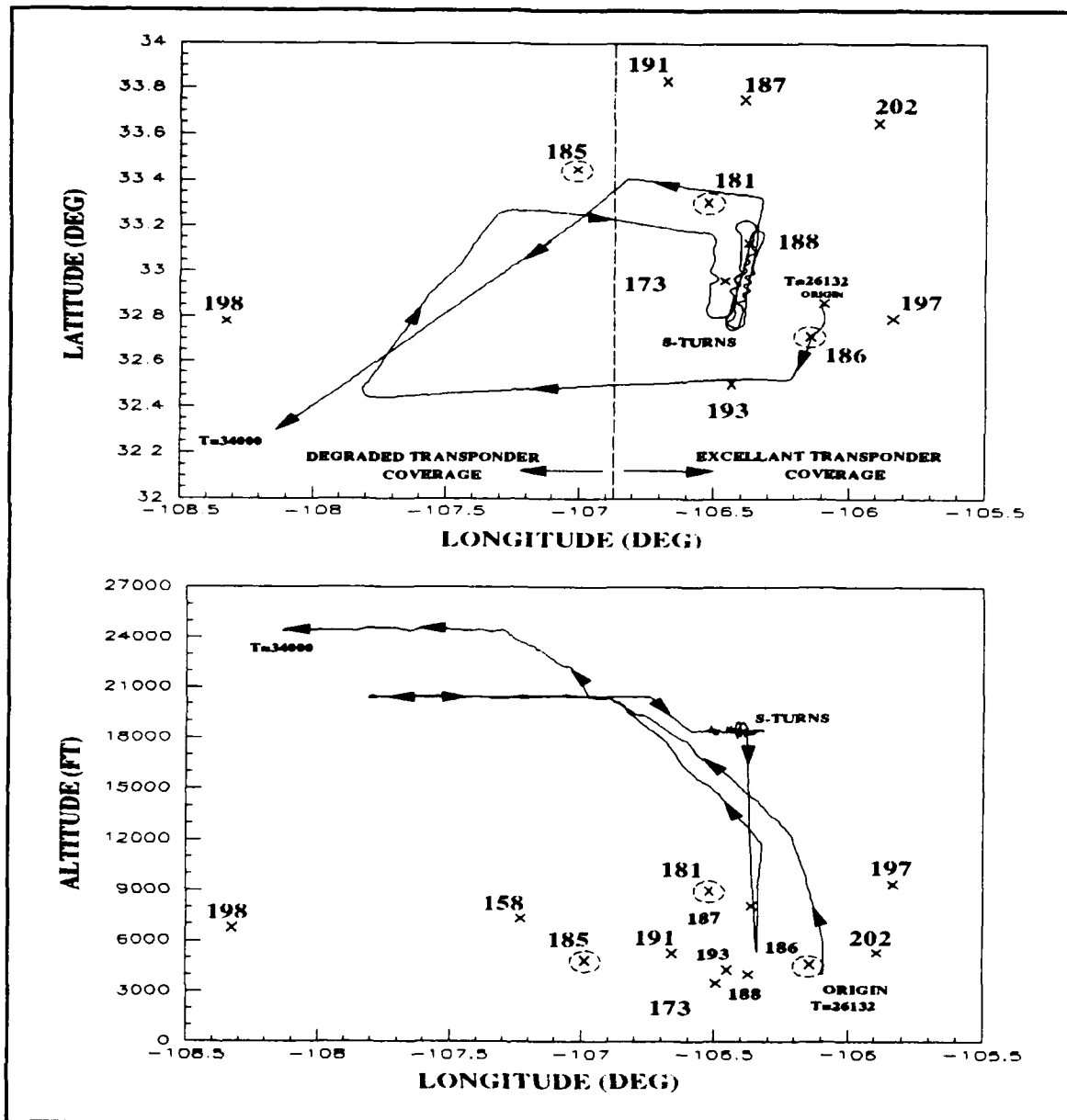


Figure 4-3. CIRIS Abbreviated Flight Profile

The measurement cycle times (T_R and T_M) are available on the CIRIS flight tape.

A FORTRAN program is used to preprocess the CIRIS flight tape. This program generates the acceleration data using Eqs (4-21), (4-22), and (4-23). It converts the delta range measurements into range-rate measurements (Eq(4-24)). Finally, the programs writes the flight trajectory data (INS position, velocity, acceleration, and baro altimeter)

to an MSOFE flight file, and the range and range-rate data to a MSOFE measurement data file. This INS data and the transponder mapping for this flight are shown in Appendix D.

These data files are processed in MSOFE from takeoff at time 26132 to time 34000 (2.25 hours). The range and range-rate measurements are updated from 1 transponder every second. A 7σ tolerance is used for residual monitoring. Any measurement greater than 7 times the predicted residual σ is rejected for both range and range-rate measurements. This residual monitoring technique resulted in 14% of the 16,060, range and range-rate measurements from all transponders, being rejected by the filter; this number of rejected measurements is considered acceptable and does not affect the overall quality of the filter estimated errors. The error state means, error state covariances, and residuals are analyzed in the following sections.

Residual Analysis

The range and range-rate residuals are a direct indication of how well the Kalman filter model is representing the real world. If the Kalman filter model matches the real world model, the residuals become a "white" noise process with a mean of zero and a 1σ value equal to $(HPH^T + R)^{\frac{1}{2}}$. In most cases it is not possible to model the real world error sources, therefore the correctness of the model is directly related the residual statistics proximity to the ideal statistics.

The current CIRIS residuals are also examined to compare and emphasize any differences. The range and range-rate residuals are analyzed for transponders 181, 185, and 186. The locations of these transponders, with respect to the flight trajectory, are shown in Figure 4-3 (locations are circled). The current CIRIS filter uses delta range measurements instead of range-rate measurements, but since the two quantities are linearly related (Eq (4-24)), the overall envelopes should be similar. The full-ordered filter residuals are designated "TRUTH" and the current CIRIS filter residuals are designated "CIRIS."

The range residuals are shown in Figure 4-4. The left column contains the range residuals for the full-ordered filter and the right column contains the range residuals for the current CIRIS filter. The 1σ values shown in the plots are the filter calculated $(HPH^T + R)^{\frac{1}{2}}$ values.

The predicted and actual means and 1σ values for the full-ordered filter and the current CIRIS filter range residuals are shown in Table 4-1. The full-ordered filter residuals fit the predicted 1σ very well, but the current CIRIS filter residuals do not fit the predicted 1σ values. The current CIRIS filter residuals are also biased and exhibit correlated errors. This indicates the full order filter is doing a much better job in estimating the correlated errors.

Table 4-1
Range Residual Statistical Comparison

Transponder	"Truth"		CIRIS	
	Mean ft	1σ Value ft	Mean ft	1σ Value ft
181	+0.14	6.56	+1.97	6.49
185	+0.28	4.58	+11.02	5.51
186	-0.04	6.09	+6.55	6.74
Filter Predicted	0.00	3.0	0.00	16.0

The actual 1σ values for the "truth" and CIRIS filters are very close. This indicates that the magnitude of the random error in both filters is the same, as expected. Overall, the "truth" model filter range residual characteristics are closer to the ideal (filter predicted) residual characteristics. Therefore, the position and velocity estimated errors predicted by the filter based on the "truth" model are closer to the real world true errors than the current CIRIS filter error estimates.

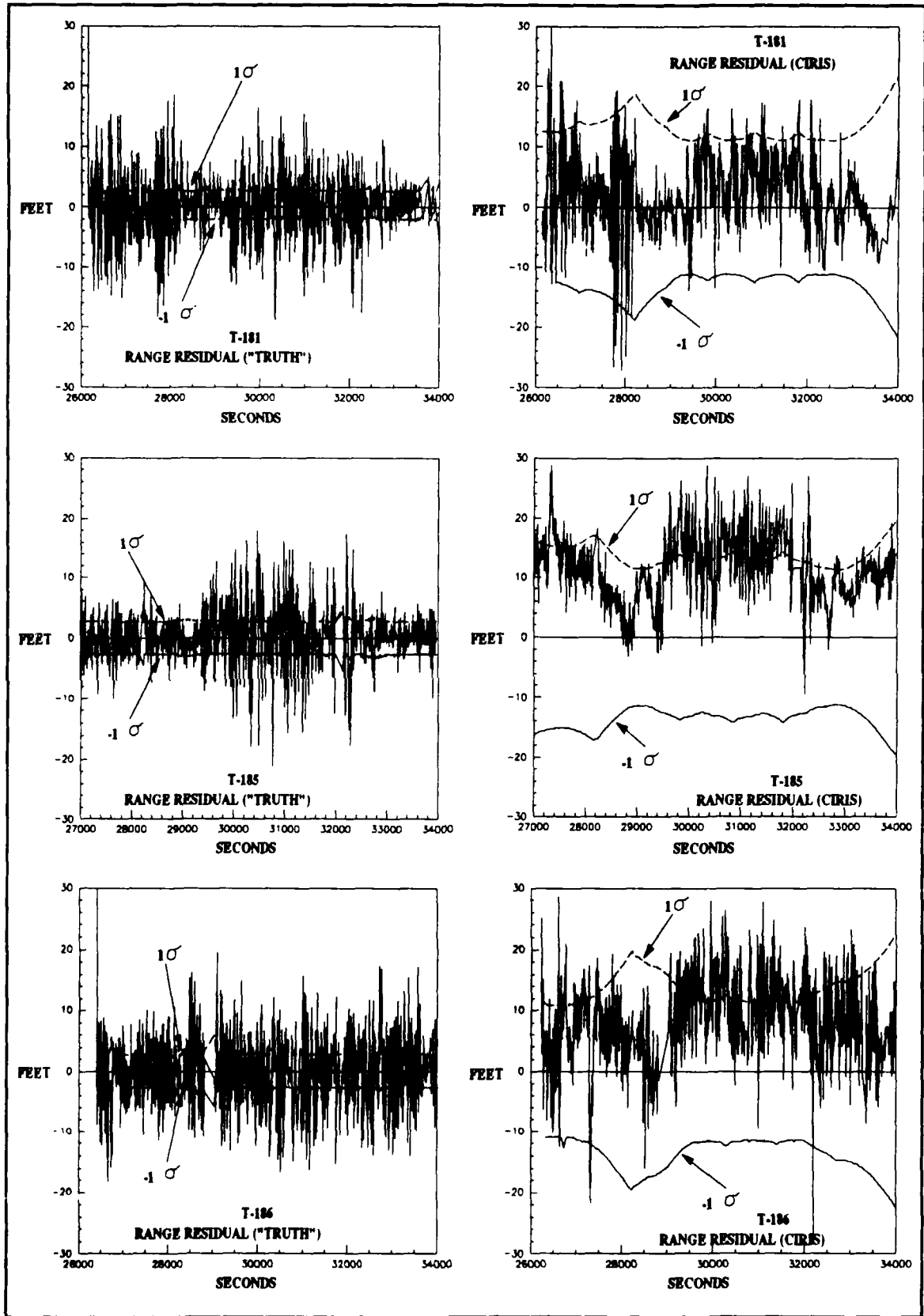


Figure 4-4. Range Residuals (CIRIS and "TRUTH")

The range-rate residuals are shown in Figure 4-5. The left column contains the range-rate residuals for the full-ordered filter and the right column contains the delta range residuals for the current CIRIS filter. The 1σ values shown in the plots are the filter calculated $(HPH^T + R)^{\frac{1}{2}}$ values.

The predicted and actual means and 1σ values for the full-ordered filter and the current CIRIS filter range-rate residuals are shown in Table 4-2. The full-ordered filter residuals fit the predicted 1σ very well, but the current CIRIS filter residuals do not fit the predicted 1σ values very well. The current CIRIS filter residuals are also biased and exhibit correlated errors. Again, this indicates the full order filter is doing a much better job in estimating the correlated errors.

Table 4-2
Range-Rate Residual Statistical Comparison

Transponder	"Truth"		CIRIS	
	Mean fps	1σ Value fps	Mean ft	1σ Value ft
181	+0.07	0.48	-0.08	0.20
185	+0.05	0.43	-0.14	0.18
186	+0.01	0.47	-0.12	0.20
Filter Predicted	0.00	0.3	0.00	0.3

The actual 1σ values for the "truth" and CIRIS filters are significantly different in this case. This is due to the residual calculations being based on different equations and presented in different units (ft vs fps). Basically, the delta range measurement is the integral of the range-rate measurement over the applicable measurement cycle. Therefore, this difference is reasonable. Overall, the "truth" model filter range-rate residual characteristics are closer to the ideal (predicted) residual characteristics. Therefore, the position and velocity estimated errors predicted by the filter based on the "truth" model are closer to the real world true errors than the current CIRIS filter error estimates.

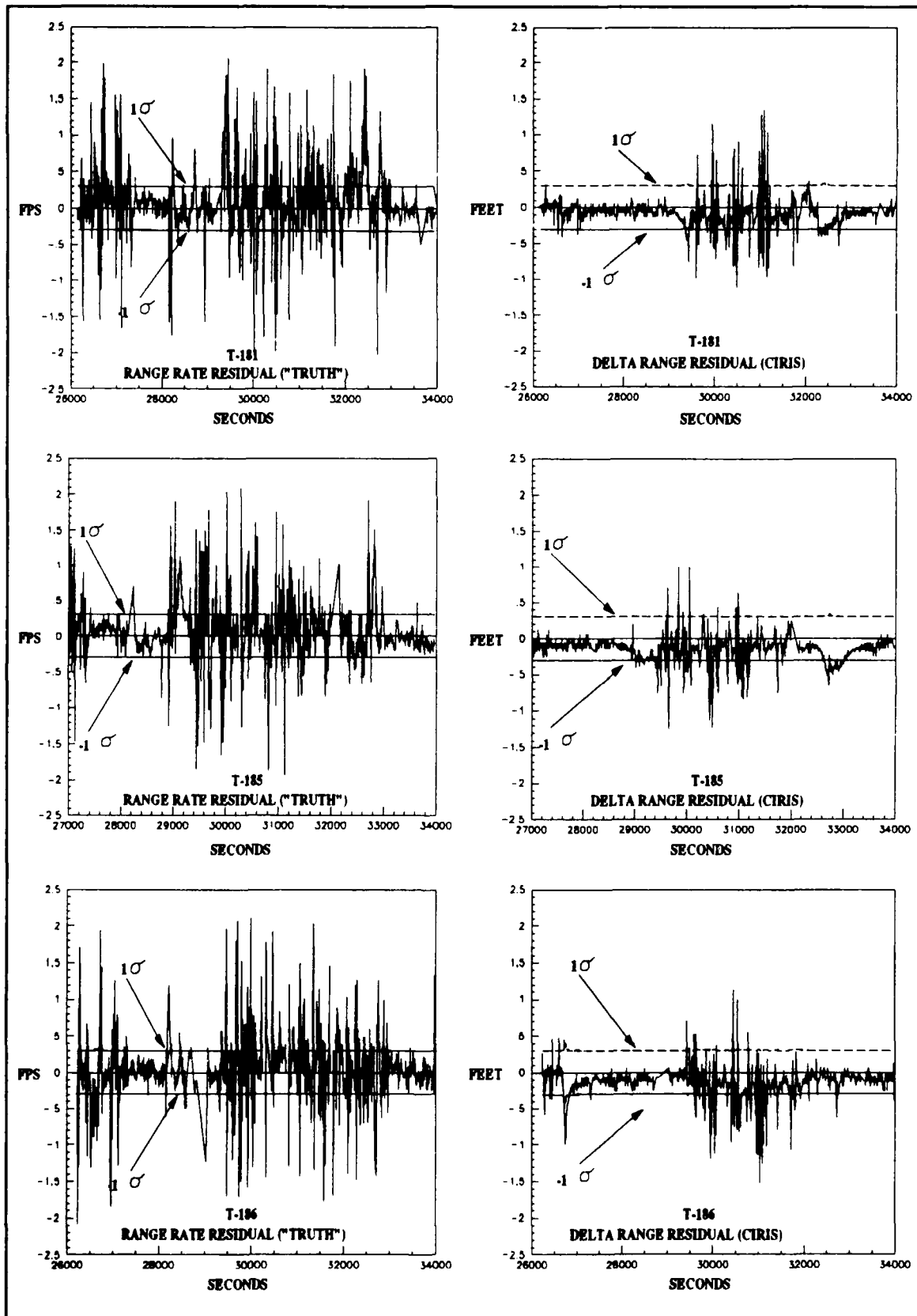


Figure 4-5. Range-Rate Residuals (CIRIS and "TRUTH")

Overall, the "truth" model residual statistics are closer to the filter predicted than the current CIRIS filter. The measurement white noise strengths (R_R and R_{RR}) could be adjusted to draw the "truth" model filter residual statistics even closer to the predicted. However, this process is very time consuming and the possible gain in accuracy is not significant enough to warrant this additional time. This topic is discussed further in Chapter 6.

Full-Ordered Filter Data

The full-ordered filter's means and 1σ values for the position and velocity error states are examined first. Next, the differences between the full-ordered filter and the current CIRIS filter means and 1σ values are plotted to compare the two filters.

Means and 1σ Values. The position error state means and 1σ values are shown in Figure 4-6. The INS latitude error growth increases from 0 to approximately -2700 ft in the 2.25 hour period and the filter's assigned 1σ value varies from 2.5 to 8 ft; note that the Schuler mode is clearly visible in the error growth. The longitude error growth increases from 0 to -3000 ft and the filter's assigned 1σ value varies from 3 to 6.7 ft. The altitude error growth (ignoring initial transient) varies from 0 to -900 ft and the filter's assigned 1σ value varies from 10 to 90 ft. The general shape, magnitude, and sign of the "truth" model filter's position error means follow closely the current CIRIS filter means. The increasing position error is characteristic of the INS. The 1σ values of the "truth" model filter position error estimates are less than the current CIRIS position error 1σ values; indicating the higher accuracy in the "truth" model position error estimates. The areas of lower accuracy in the 1σ plots corresponds with the degraded transponder coverage areas shown in Figure 4-3.

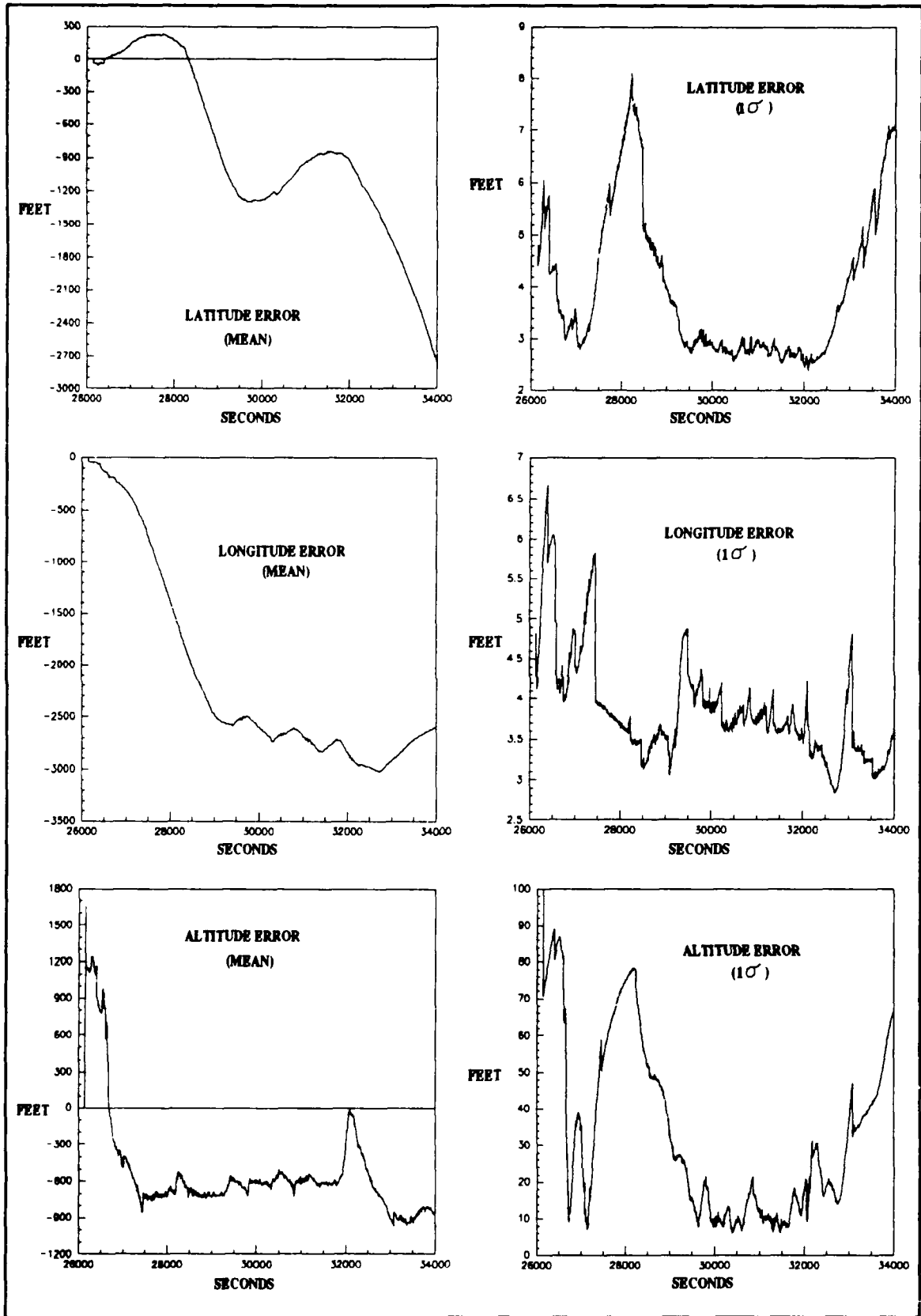


Figure 4-6. Position Error States ("TRUTH")

The velocity error state means and 1σ values are shown in Figure 4-7. The North velocity error growth varies from +0.6 to -1.2 fps and the filter's assigned 1σ value varies from 0.025 to 0.057 fps. The West velocity error growth varies from +0.6 to -1.2 fps and the filter's assigned 1σ value varies from 0.035 to 0.057 fps. The vertical velocity error growth varies from +3 to -3 fps and the filter's assigned 1σ value varies from 0.1 to 0.51 fps. The general shape, magnitude, and sign of the "truth" model filter's velocity error means follow closely the current CIRIS filter means. The 1σ values of the "truth" model filter position error estimates are less than the current CIRIS velocity error 1σ values; indicating the higher accuracy in the "truth" model velocity error estimates.

Means and 1σ Value Differences. The difference in position and velocity error state means and 1σ values between the full-ordered filter and the current CIRIS filter are shown in Figure 4-8 and 4-9 respectively. The differences are formed by subtracting current CIRIS filter data from the full-ordered filter data ("TRUTH" - CIRIS). A large initial transient is exhibited in all the difference plots. This large initial error is caused by the CIRIS flight tape recording start time. Due to delays before takeoff of the aircraft, the flight tape recorder is not started until just before takeoff. A significant amount of time can elapse between the end of INS alignment and the tape turn on. The INS data at the beginning of the tape can already contain substantial error growth. The initial transient is the amount of time required by the full-ordered filter to estimate this error. The current CIRIS filter does not experience this anomaly because it is operating in real time and receives all the data starting from the end of INS alignment. Therefore this initial transient is ignored in the analysis that follows.

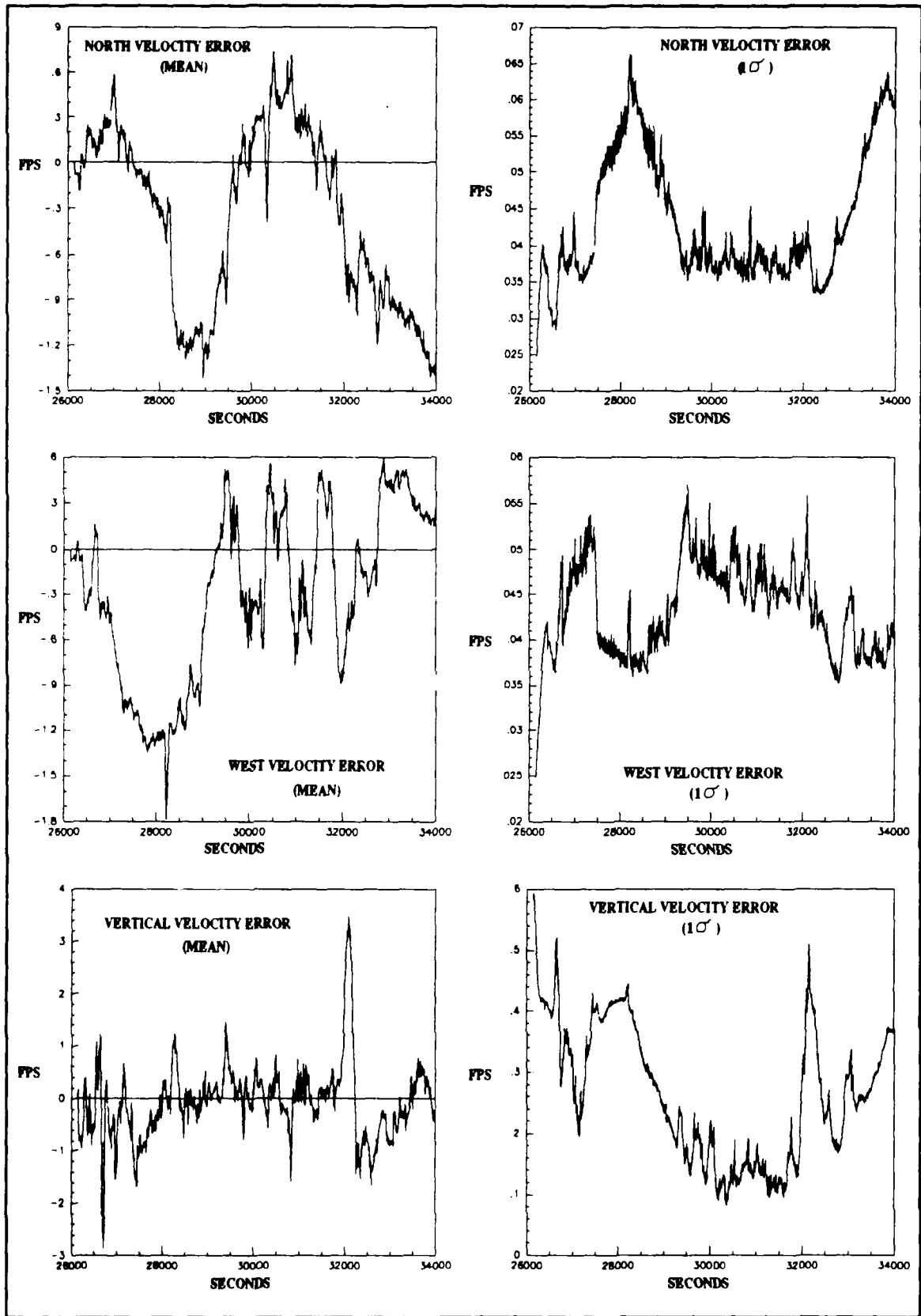


Figure 4-7. Velocity Error States ("TRUTH")

The position difference time histories are shown in Figure 4-8. These plots reflect the time varying characteristics of the filter position error state estimate difference. This magnitude of the difference is highly dependent on the aircraft trajectory and transponder geometry; in addition to the differences in the filter modeling of the correlated errors. To quantify the differences the mean and standard deviation is calculated for the position means and 1σ values. These position difference statistics are shown in Table 4-3. The magnitude of the average difference is less than the independently verified position accuracies of the current CIRIS filter. This average mean difference is representative of how much the "truth" model filter's position error state means are moving towards the true error.

The velocity difference time histories are shown in Figure 4-9. These plots reflect the time varying characteristics of the filter velocity error state estimate difference. This magnitude of the difference is highly dependent on the aircraft trajectory and transponder geometry; in addition to the differences in the filter modeling of the correlated errors.

Table 4-3
Position Error State Differences

Position Error States	Mean Difference		1σ Value Difference	
	Mean ft	1σ Value ft	Mean ft	1σ Value ft
Latitude	+3.37	7.98	+0.03	0.42
Longitude	+5.73	10.29	0.00	0.39
Altitude	+25.66	63.86	+6.82	5.04
Note: All differences are "Truth" - CIRIS				

To quantify the differences the mean and standard deviation are calculated for the velocity means and 1σ value differences. These velocity difference statistics are shown in Table 4-4. The magnitude of the average difference is less than the independently verified velocity accuracies of the current CIRIS filter. This average mean difference is representative of how much the "truth" model filter's velocity error state means are moving towards the true error.

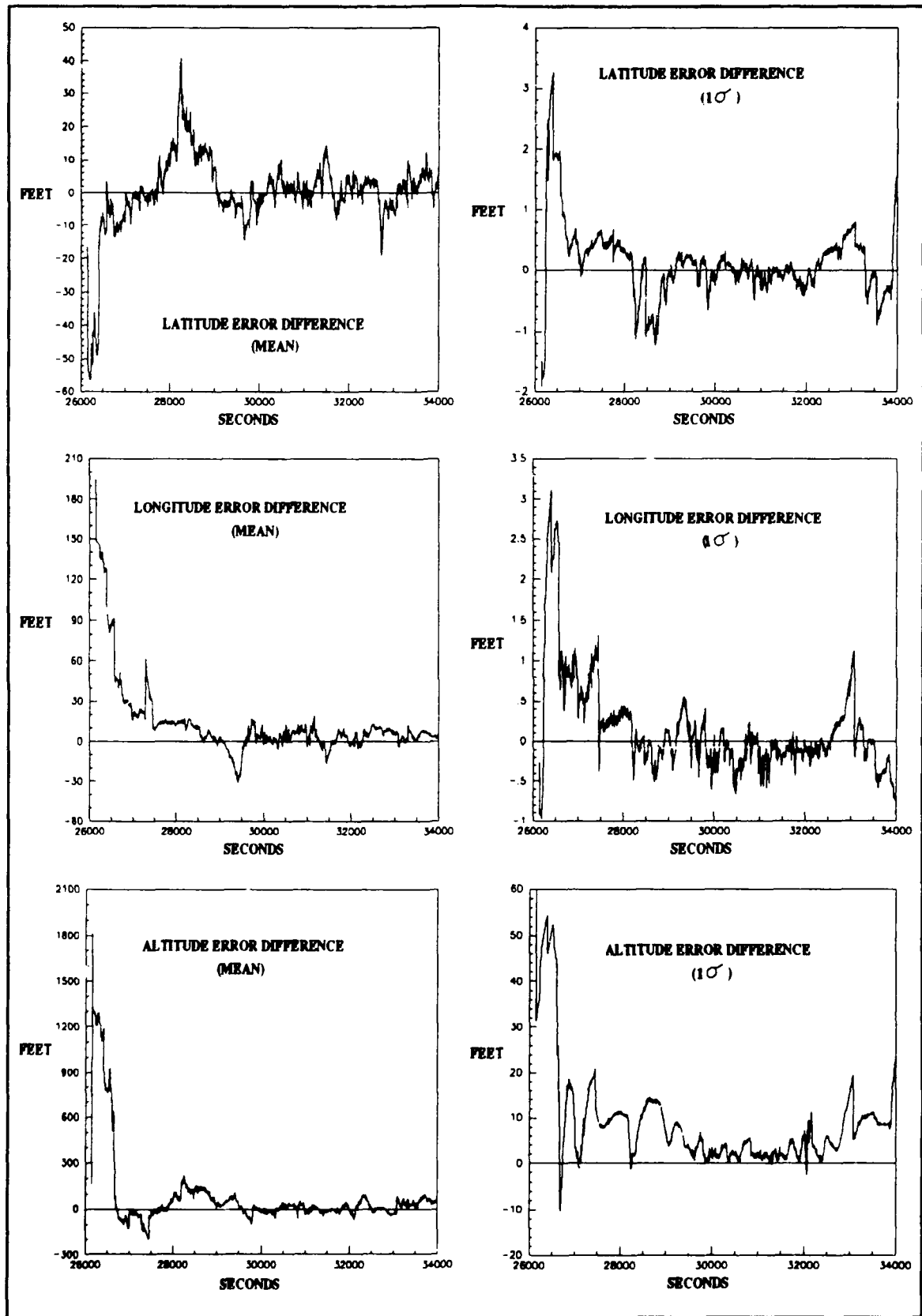


Figure 4-8. Position Differences ("TRUTH" - CIRIS)

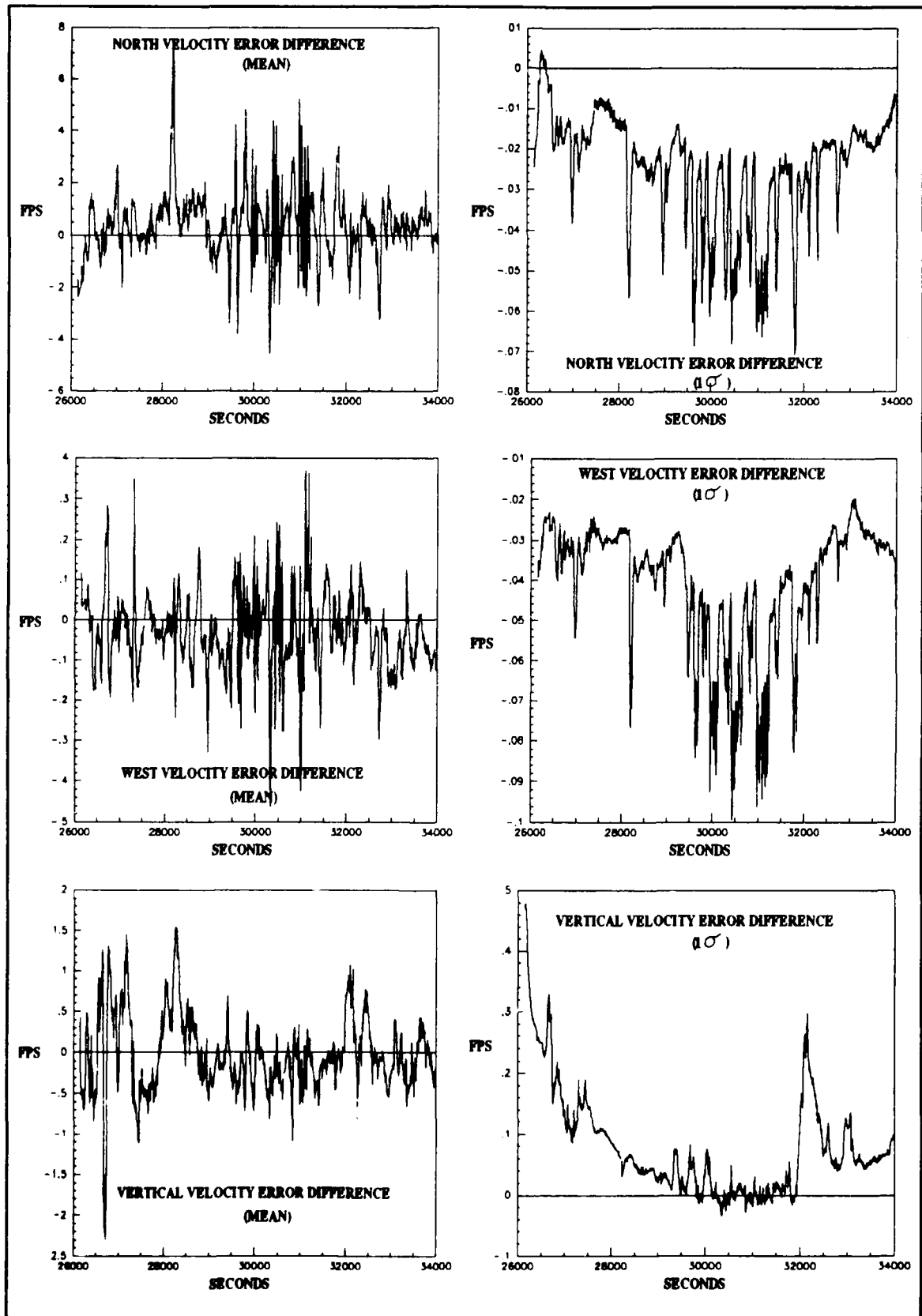


Figure 4-9. Velocity Differences ("TRUTH" - CIRIS)

Table 4-4
Velocity Error State Differences

Velocity Error States	Mean Difference		1 σ Value Difference	
	Mean fps	1 σ Value fps	Mean fps	1 σ Value fps
North	+0.05	0.13	-0.03	0.01
West	-0.03	0.10	-0.04	0.02
Vertical	+0.01	0.47	+0.06	0.05

Note: All differences are "Truth" - CIRIS

Correlated Measurement Error Analysis

The correlated measurement errors are the calibration range and range-rate biases; X', Y', and Z' (E-frame) transponder survey errors; and the transponder atmospheric error. These transponder errors are analyzed for the 3 transponders defined in the "Residual Analysis" section.

Transponder Survey Errors. The Kalman filter estimates the error in the X', Y', and Z' coordinates of the transponder survey. These error values should remain constant in time. How well the filter estimates these errors is a function of the trajectory of the aircraft with respect to the transponder and the ECEF axes. The values obtained at the end of the time history are considered representative of the error magnitudes and are presented in the following sections.

The error state means and 1 σ values for transponder 181 survey errors are shown in Figures 4-10 and 4-11. The aircraft trajectory with respect to this transponder is defined in Figure 4-3. The aircraft trajectory completely encircles this transponder and traverses it at different altitudes. The geometric relationship is very good and the accuracy of the filter estimates should be high. The final X' error attained a mean of -12 ft and a 1 σ value of 2.3 ft. The Y' error attained a mean of +3 ft and a 1 σ value of 3.95 ft. The Z' error attained a mean of 0 ft and a 1 σ value of 3.2 ft. The envelopes of the horizontal

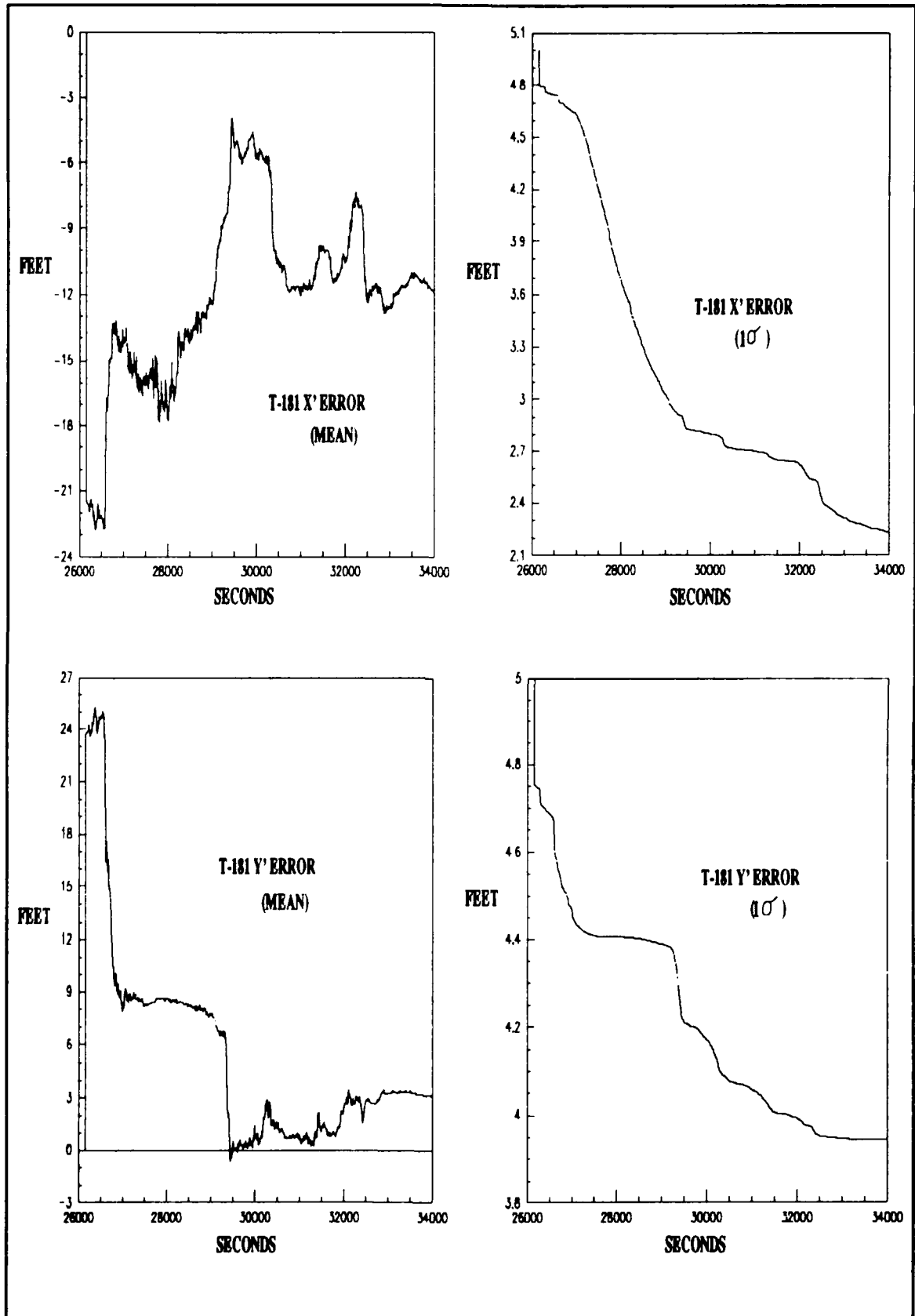


Figure 4-10. T-181 X' and Y' Correlated Errors

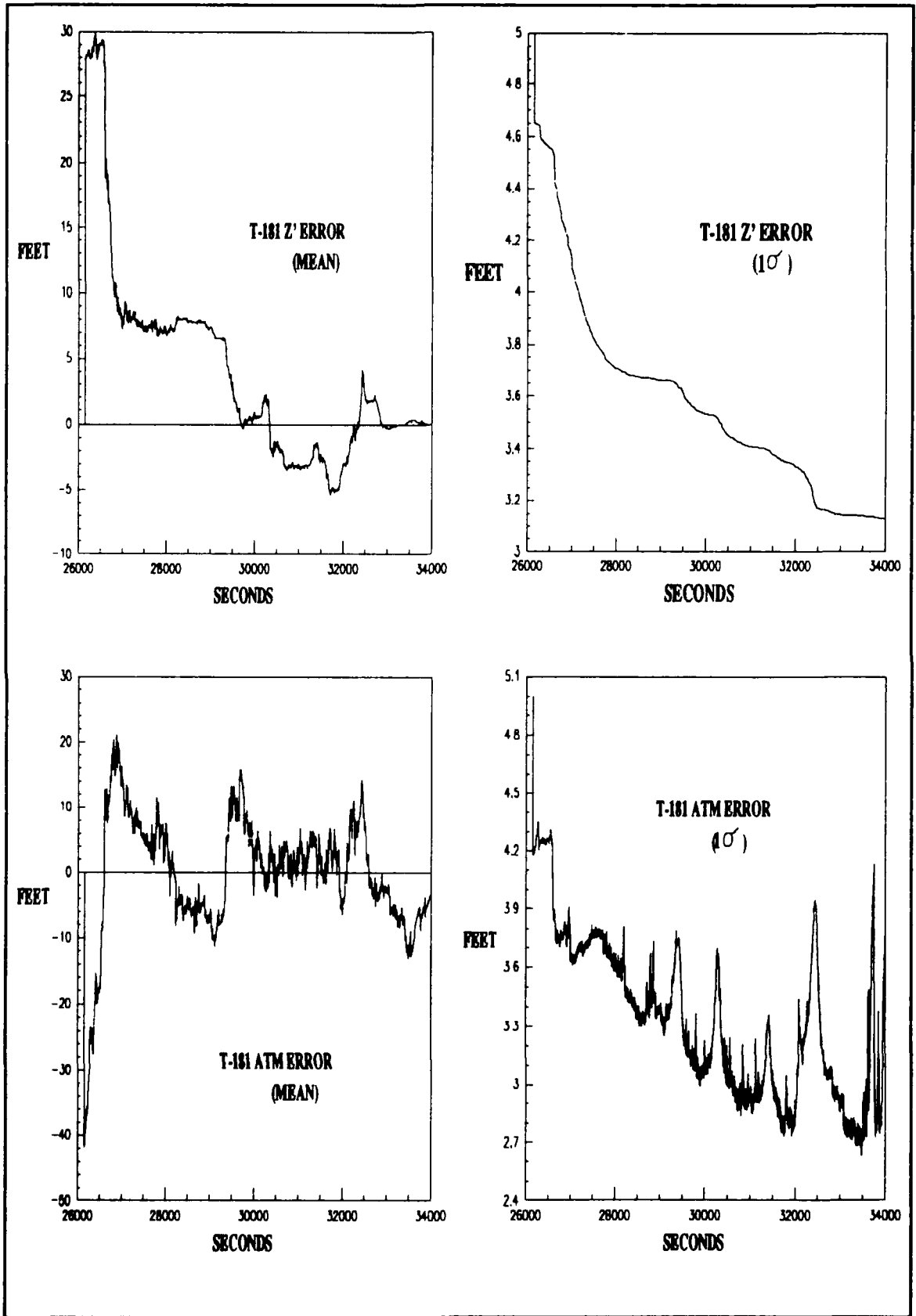


Figure 4-11. T-181 Z' and Atmospheric Correlated Errors

errors quickly move toward a steady state value indicating the filter is accurately determining the error magnitude. However, the Z' error does not quickly converge to a steady value of zero. This may indicate a negligible survey error in the Z' direction or an observability problem due to the aircraft trajectory.

The error state means and 1σ values for transponder 185 are shown in Figures 4-12 and 4-13. The aircraft trajectory with respect to this transponder is shown in Figure 4-3. The aircraft transverse the transponder only to the South of it. This geometric relationship is the worst of the 3 transponders and the filter should have the most trouble estimating these survey errors in all 3 ECEF axes. The final X' error attained a mean of -5 ft and a 1σ value of 2.6 ft. The Y' error attained a mean of -4 ft and a 1σ value of 4 ft. The Z' error attained a mean of -13 ft and a 1σ value of 3.5 ft. The envelopes of all 3 errors are continuously varying and do not approach a steady state value. The accuracy of these filter error estimates is not high, as expected.

The error state means and 1σ values for transponder 186 are shown in Figures 4-14 and 4-15. The aircraft trajectory with respect to this transponder is shown in Figure 4-3. The aircraft transverse this transponder to the North, but it does directly overfly it. The final X' error attained a mean of -14 ft and a 1σ value of 2.2 ft. The Y' error attained a mean of +5 ft and a 1σ value of 4 ft. The Z' error attained a mean of +5 ft and a 1σ value of 3 ft. The envelopes of these errors resemble the T-185 survey error envelopes, indicating the difficulty the filter is having estimating the survey errors due to the poor geometry.

This data indicates the transponder survey errors are observable and the filter's random bias shaping filter model is estimating the error magnitudes. The the geometric relationship of the line-of-sight vectors (aircraft to transponder) with transponder survey error vector determines how well the error is estimated. Therefore, the ultimate accuracy of the survey error magnitudes is directly related to the aircraft/transponder geometric relationship as described above.

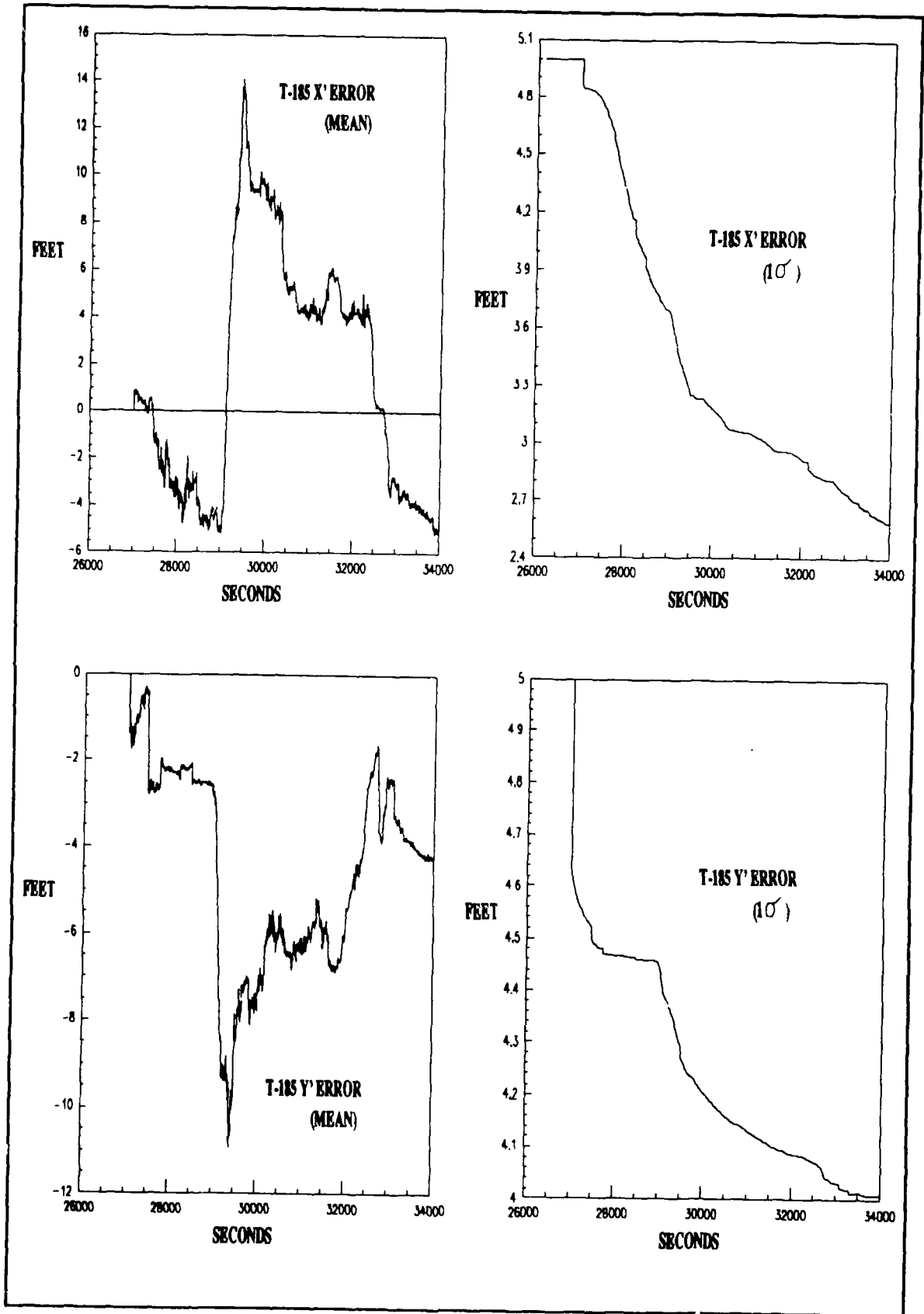


Figure 4-12. T-185 X' and Y' Correlated Errors

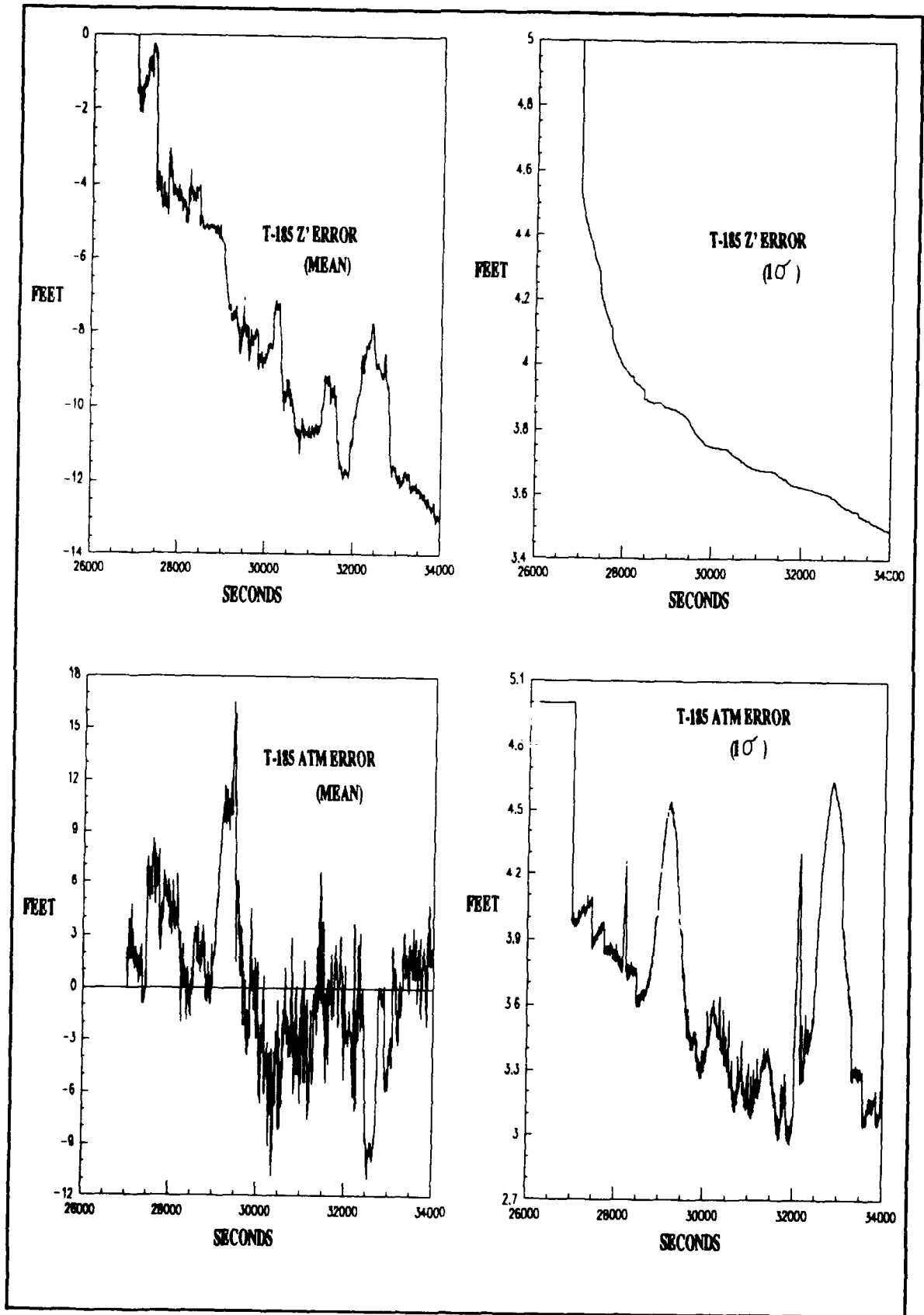


Figure 4-13. T-185 Z' and Atmospheric Correlated Errors

Atmospheric Errors. The Kalman filter is estimating the line of sight error in the range measurement due to propagation delays caused by atmospheric conditions. This is a time varying error and is a function of weather conditions and aircraft distance from the transponder. The range of the error and the corresponding average 1σ value are noted in the following sections.

The atmospheric error state plots are shown in Figures 4-11, 4-13, and 4-15 for transponders 181, 185, and 186 respectively. This error is attributed to the changing atmospheric index of refraction (n) which causes a decrease in the electromagnetic wave propagation velocity, erroneously causing a increase in the measured range magnitudes. Therefore, the filter estimated atmospheric error normally is expected to be a negative value. However, the CIRIS computer makes an open loop correction to the range measurement before it is processed by the filter. This allows the atmospheric error to vary between negative and positive magnitudes. This characteristic is clearly observable in the atmospheric error time histories.

The atmospheric error state mean for transponder 181 varies from -10 to +17 ft with an average 1σ value of 3.5 ft. The atmospheric error state mean for transponder 185 varies from -10 to +17 ft with an average 1σ value of 3.5 ft. The atmospheric error state mean for transponder 181 varies from -18 to +18 ft with an average 1σ value of 3.6 ft. The magnitude and shape of the error time histories are reasonable for this type of error. Therefore, this error is observable and the first-order Markov shaping filter is allowing the filter to derive an accurate estimate for this error.

Calibration Errors. The Kalman filter is estimating the line of sight error in range or range-rate due to a calibration error in the aircraft transponder interrogator. This error is small and a function of the condition of the aircraft hardware.

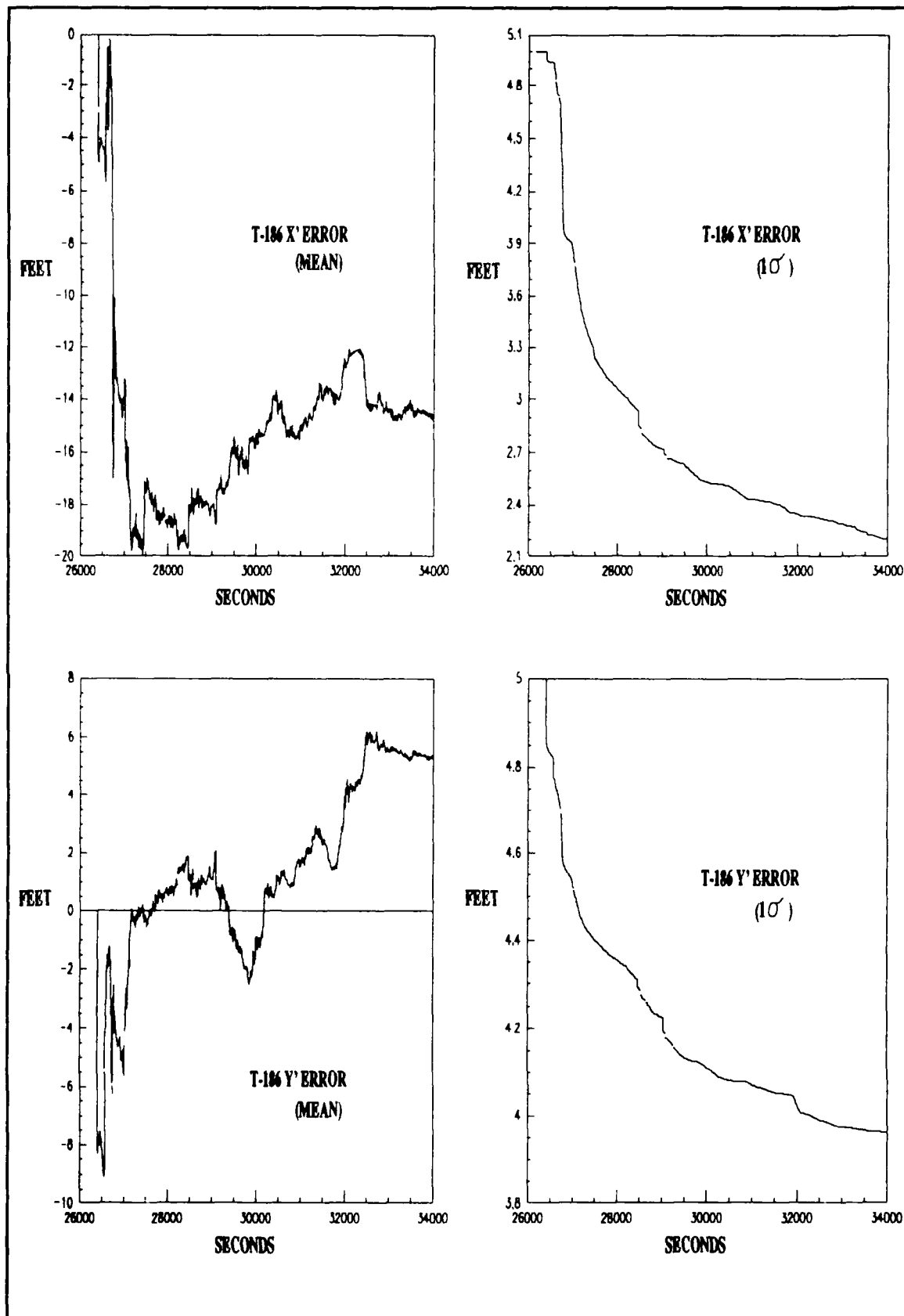


Figure 4-14. T-186 X' AND Y' Correlated Errors

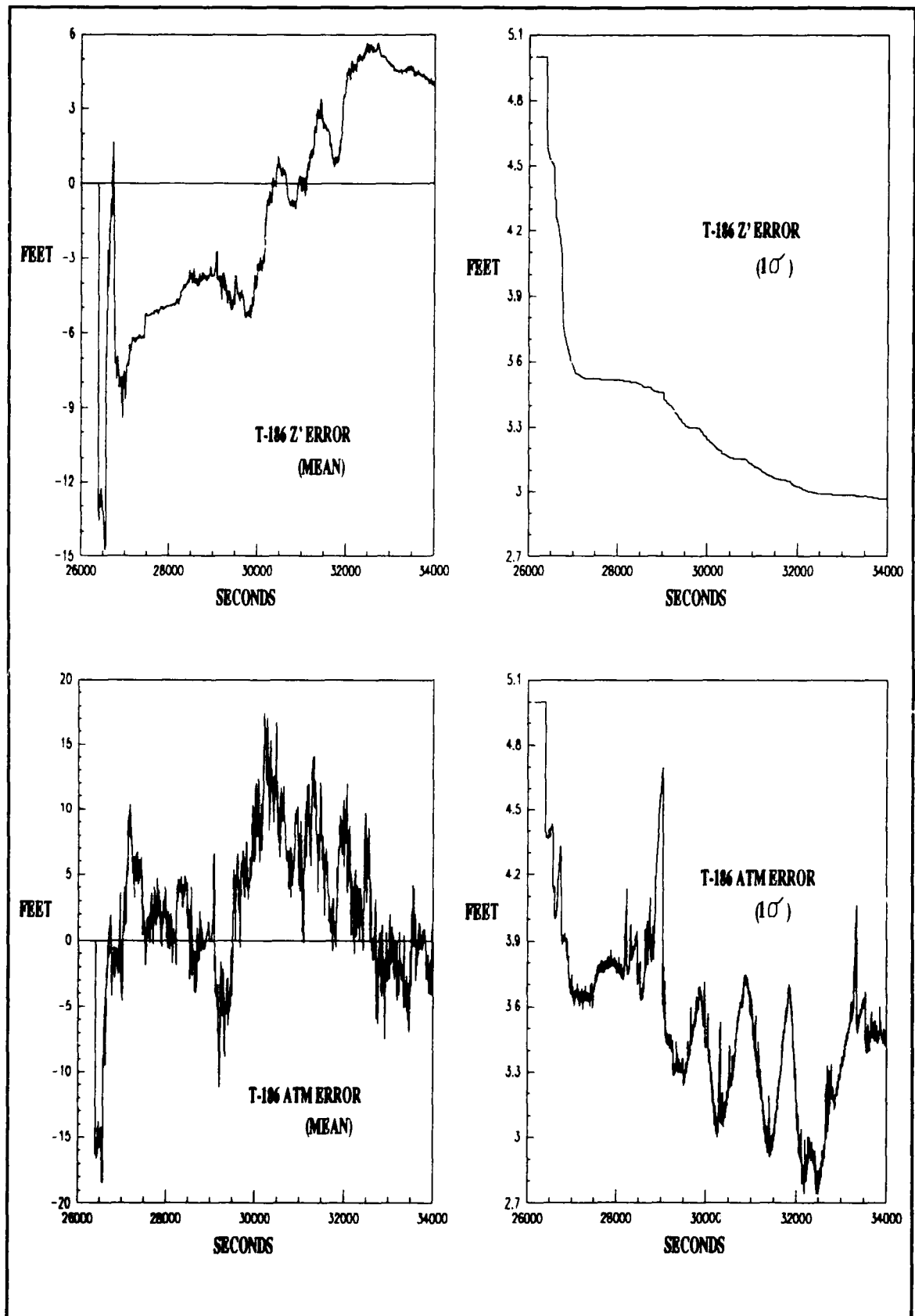


Figure 4-15. T-186 Z' and Atmospheric Correlated Errors

The range and range-rate calibration error state means and 1σ values are shown in Figure 4-16. The range calibration error state mean ranges from -2.5 to +0.5 ft with an average accuracy of 0.75 ft (1σ). The range-rate calibration error state mean ranges from -0.13 to +0.09 fps with an accuracy of 0.006 fps (1σ). The shape and magnitude of these curves are reasonable for this type of error. This indicates the random bias shaping filter model is adequate for estimating this error.

Summary

This chapter develops the "truth" model for the range and range-rate measurements. This model is augmented to the INS "truth" model to form the full-ordered filter. The full-ordered filter is used to process 2.25 hours of empirical data from a CIRIS flight tape.

The means and 1σ values for position and velocity error states are plotted and compared to the current CIRIS filter data. The correlated error states for the transponder calibration, survey, and atmospheric error sources are plotted and significant characteristics noted. Final conclusions based on this data are discussed in Chapter 6.

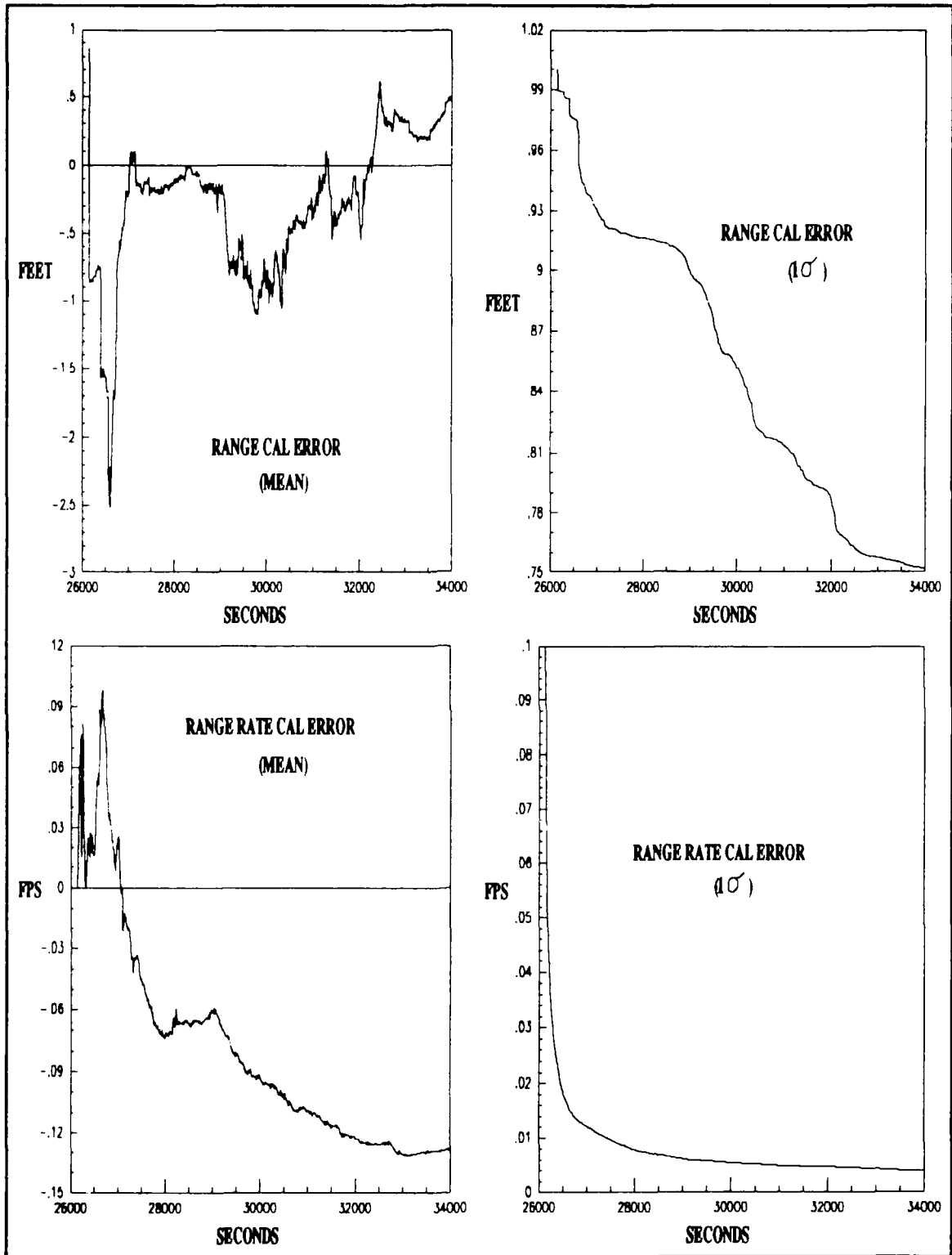


Figure 4-16. Range and Range-Rate Correlated Errors

V. Reduced-Order Filter Design/Simulation

This chapter develops the reduced-order filter model from the 127-state "truth" model described in Chapter 4. The state reduction method is described and a 70-state reduced-order filter model defined. The CIRIS flight data, processed by the filter based on the 127-state "truth" model, is processed by the reduced-order filter based on a 70-state model. The 127-state filter data is compared to the 70-state filter data to quantify the change in performance. The comparison concentrates on the differences in the position error states, velocity error states, and selected residuals.

Selection of States

This reduced-order filter is designed to function as a post processor of CIRIS flight data. The main objective of this reduced-order filter design is to decrease the 34 hours of CPU time (VAX 8650 computer) required to process the data from a 4.5 hour CIRIS flight, using the 127-state filter, without a significant reduction in filter estimation accuracy. An acceptable processing length of time is considered to be 8-12 hours (or less) of CPU time (on a VAX 8650 computer).

The first step in eliminating states from the "truth" model is to define the states that are not candidates for elimination. These states consist of all 42 error measurement states (δX_{MEAS}) defined in Appendix C; the INS (δX_{INS}) 13 general error states (1-13), 10 correlated error states (14-23), and 2 baro altimeter bias error states (72,73) defined in Appendix B. The magnitudes of these error states are significant and required to preserve the accuracy of the basic filter model. This defines a total of 67 states as the minimum number of states in the reduced-order filter.

The remaining 60 states (24-71,74-85) are considered based on their respective mean and covariance error state magnitudes. The error state time history data obtained from the 127-state filter described in Chapter 4 is used to determine these magnitudes. The means and 1σ values for these 60 states are plotted and compared.

Many of these error states indicate a lack of observability because of a constant mean and time invariant 1σ value. Other states mean magnitudes are sufficiently small to be considered insignificant. Only 3 of these 60 states have mean magnitudes which warrant their inclusion in the reduced-order filter. The 3 gyro drift rate bias repeatability error states (24-26) are kept. This defines the 70 error states in the reduced-order filter model.

Filter Model

The stochastic differential equation defining the reduced-order filter's dynamics model is shown in Eq (5-1). The primed matrices and vectors ($\delta\mathbf{X}'_{INS}$, \mathbf{F}'_{INS} , \mathbf{Q}'_{INS} , \mathbf{P}'_{INS} , and \mathbf{W}'_{INS}) represent a 28 error state subset of the INS matrices and vectors defined in Eq (4-15).

$$\delta\dot{\mathbf{X}}(t) = \mathbf{F}(\hat{\mathbf{X}}, t) \delta\mathbf{X}(t) + \mathbf{W}(t) \quad (5-1)$$

$$\delta\mathbf{X} = \begin{bmatrix} \delta\mathbf{X}'_{INS} \\ \delta\mathbf{X}_{MEAS} \end{bmatrix} \quad \mathbf{F} = \begin{bmatrix} \mathbf{F}'_{INS} & \mathbf{0} \\ \mathbf{0} & \mathbf{F}_{MEAS} \end{bmatrix} \quad \mathbf{W} = \begin{bmatrix} \mathbf{W}'_{INS} \\ \mathbf{W}_{MEAS} \end{bmatrix}$$

$$\delta\hat{\mathbf{X}}(t_0) = \mathbf{0} \quad \mathbf{P}_{\delta\mathbf{X}}(t_0) = \begin{bmatrix} \mathbf{P}'_{INS} & \mathbf{0} \\ \mathbf{0} & \mathbf{P}_{MEAS} \end{bmatrix}$$

$$E\{\mathbf{W}(t_0)\} = \mathbf{0}$$

$$E\{\mathbf{W}(t_0) \mathbf{W}^T(t_0 + \tau)\} = \mathbf{Q}(t_0)\delta(\tau) = \begin{bmatrix} \mathbf{Q}'_{INS} & \mathbf{0} \\ \mathbf{0} & \mathbf{Q}_{MEAS} \end{bmatrix} \delta(\tau)$$

The error state model for states 1 thru 26 is identical to the INS/Transponder "truth" model defined in Chapter 4. Error states 27 and 28 in the reduced-order model are assigned to states 72 and 73 in the INS/Transponder "truth" model. Finally, the 42 measurement states from the INS/Transponder "truth" model (86 thru 127) are assigned to error states 29 thru 70 in the reduced-order filter model. The matrix and vector parameter/element values are identical to the INS/Transponder "truth" model.

The measurement model's structure for the reduced-order filter is identical to the structure defined in Eqs (4-17) and (4-18). The only difference is the error state numbers (29 thru 70 instead of 86 thru 127). Finally, the residual calculations are defined in Eqs (4-19) and (4-20). The 70-state reduced-order filter is referred to as "Reduced" throughout the remainder of this chapter.

Comparison of Reduced to "Truth"

The CIRIS flight data defined in Chapter 4 for time 26139 to 34200 is processed with the reduced-order filter. This simulation required only 8 hours of CPU time on the VAX 8650 computer, achieving the first part of the primary objective. The second part, minimizing the filter estimation performance degradation, is examined next. The range and range-rate residuals are compared first. The transponders selected for analysis in Chapter 4 (T-181, T-185, and T-186) are again analyzed. The time histories, calculated means, and calculated 1σ values for the reduced-order and "truth" model filters are compared. The differences between the two sets of residual statistics are insignificant. Therefore, the deletion of the 57 INS error states has no significant effect on the residual magnitudes and 1σ values. This indicates the change between the "truth" and reduced-order filters' position and velocity error state estimates should be small.

Another indicator of performance change is defined by inspecting the differences between the position and velocity error states of the 127-state filter and the 70-state filter. The filters' position and velocity error state means are differenced ("Truth" - Reduced) and the time histories presented in Figure 5-1. The position and velocity error state 1σ value differences are approximately zero for the entire time histories and are not presented.

The differences all exhibit a large negative spike at approximately time 28300. The cause of this spike can not be attributed directly to any aspect of the aircraft trajectory, since the flight trajectory is the same for both filters. It must be a direct result of the deletion of a state(s) that absorbed this error in the "truth" model. This anomaly is not considered critical and is not investigated further.

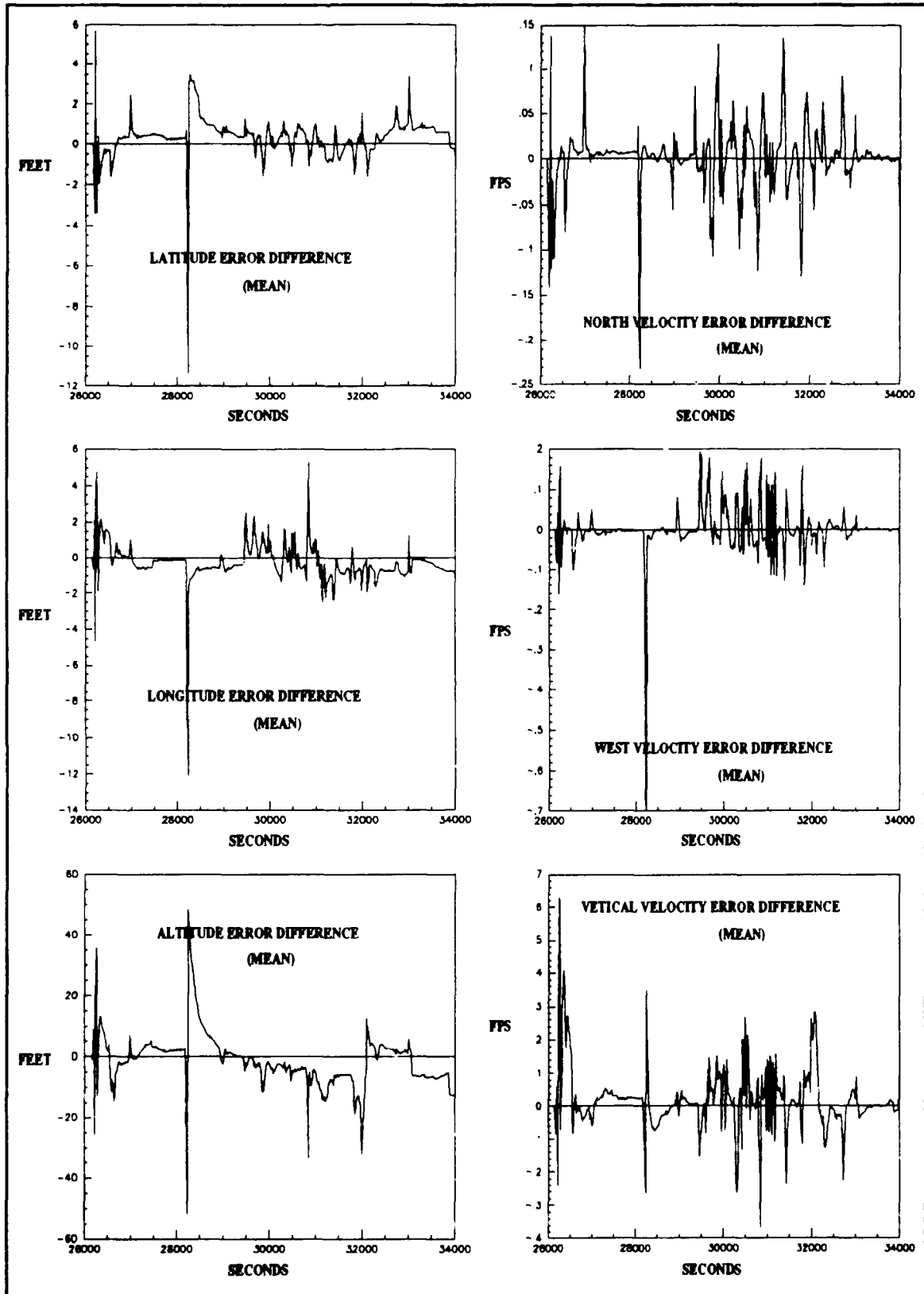


Figure 5-1. Position and Velocity Differences ("TRUTH" - REDUCED)

Generally, the differences all display a small time varying bias. The difference grows during hard aircraft maneuvers. The small bias is directly attributed to the deletion of the 57 INS error states in formulating the reduced-order filter design. To quantify this difference the mean and standard deviation of the differences are calculated and presented in Table 5-1.

Table 5-1
"Truth"/Reduced Position/Velocity Error State Differences

Position Error States	Mean Difference		Velocity Error States	1 σ Value Difference	
	Mean ft	1 σ Value ft		Mean fps	1 σ Value fps
Latitude	+0.41	1.03	North	0.000	0.030
Longitude	-0.14	0.90	West	0.000	0.050
Altitude	-4.44	11.63	Vertical	0.010	0.100
Note: All differences are "Truth" - Reduced					

The horizontal position error mean differences are less than a half foot with a standard deviation of approximately 1 foot. The horizontal velocity error mean differences are also very small. The vertical position and velocity states display the largest average difference with a position difference on the order of 5 ft and the velocity difference of approximately 0.01 fps.

The resulting change in performance between the "truth" and the reduced-order filter is small. The reduction in required computer time is significant. The "truth" model based filter required approximately 17 hours of CPU time compared to 4 hours for the reduced-order model filter on the VAX 8650 computer system. This is a 84% reduction in computer time with a small loss in performance.

Covariance Analysis Consideration

Ideally, the next step to complete the design of the reduced-order filter is to optimally tune it using a covariance analysis (16:325). This consists of running the reduced-order filter with measurements from the "truth" model and tuning the noise strengths (Q and

R) of the reduced-order filter until the the "true" error covariance is as close as possible to the reduced-order filter's error covariance magnitude. In the previous section, only the diagonal elements, of the error covariance matrix are compared resulting in a negligible difference. The effects of the off-diagonal elements are ignored in this analysis. Therefore, a covariance analysis and filter tuning can produce an increase in performance.

The MSOFE program is capable of performing this analysis. However, this analysis requires the 127-state filter and the 70-state filter to be operated simultaneously in the analysis. This requires the simulation of a filter on the order of 200 states.

This analysis is computationally intensive and time consuming. The comparison in the previous section indicates only a small gain in performance. Based on these considerations no attempt is made to increase the performance of the reduced-order filter through this technique.

Comparison of the Reduced and CIRIS filters

The reduction in required computer time allows the reduced-order filter to easily process the entire 4.5 hour flight trajectory. This simulation required only 8 hours of CPU time on the VAX 8650 computer system. To quantify the performance of the reduced filter, its position and velocity error state statistics are compared to the data from the current CIRIS filter. In addition, since this complete CIRIS flight required 18 transponders, transponder switching in and out of the 10 transponder correlated error state window is required. The performance of this technique is also presented and examined in this section.

Position and Velocity Differences. The data position and velocity error state data from the filter are compared to the current CIRIS filter for the entire flight. The differences in the mean and 1σ values for the entire flight (time 26139 to 42300) are shown in Figures 5-2 and 5-3.

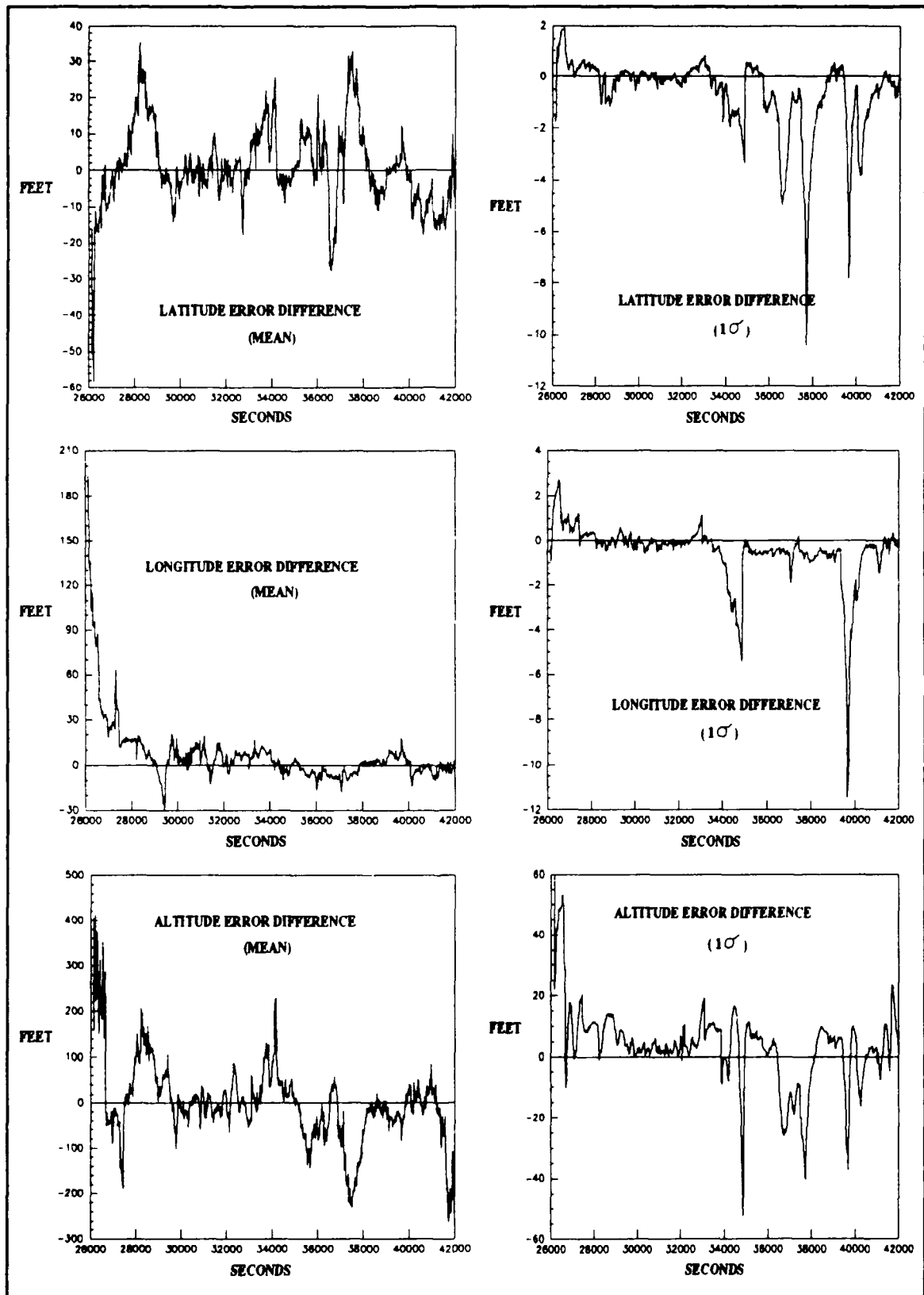


Figure 5-2. Position Differences (REDUCED - CIRIS)

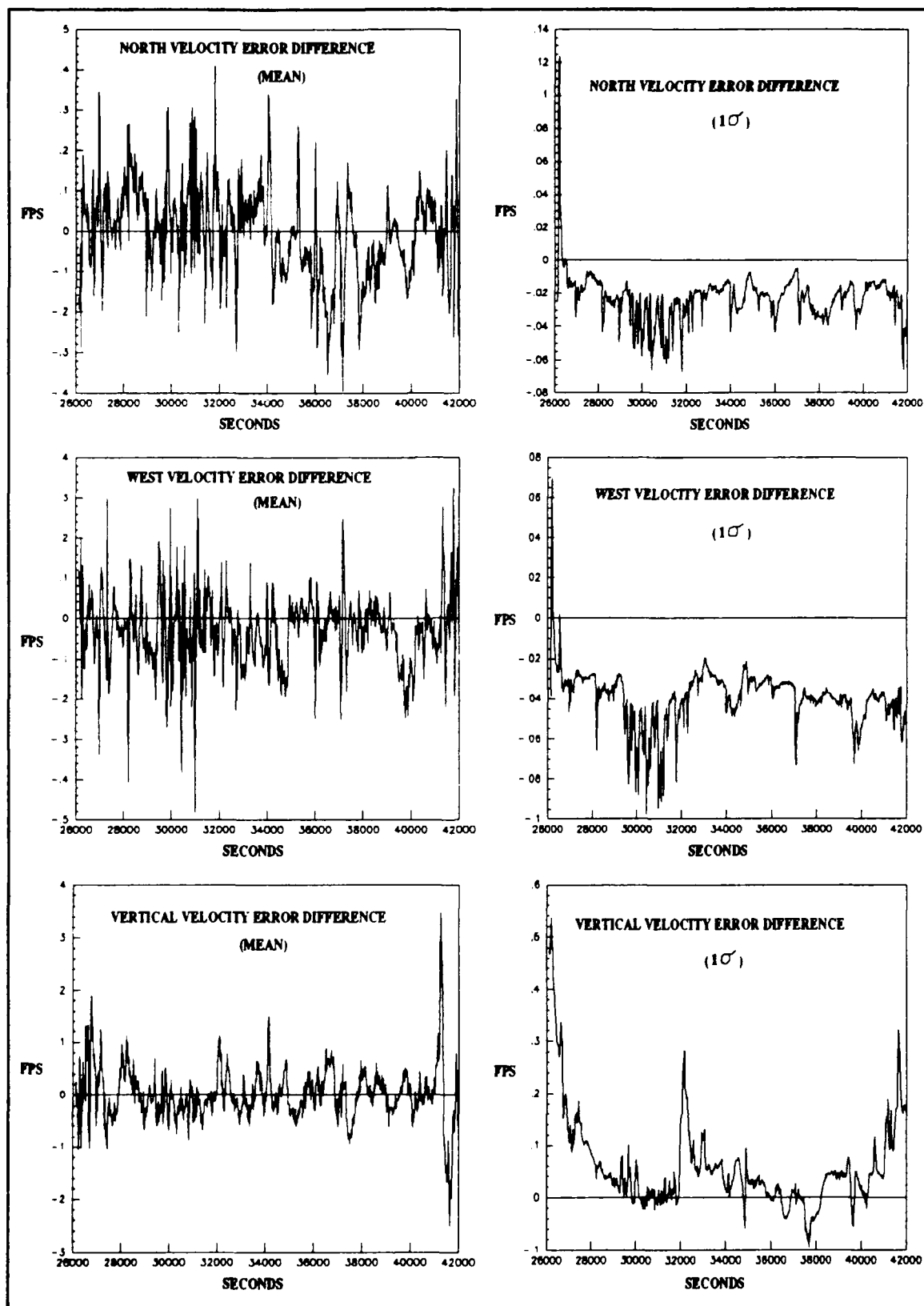


Figure 5-3. Velocity Differences (REDUCED - CIRIS)

The characteristics of the differences are very similar to the characteristics exhibited in Chapter 4 between the "truth" model and the current CIRIS filter (Figures 4-8 and 4-9). The difference time histories for flight segment not shown in Chapter 4 (time 34200 to 42300) closely resemble the segment examined in Chapter 4 (time 26139 to 34200). No significant anomalies are identified. However, the position 1σ value differences grow in magnitude for this later flight portion. The cause of the error growth is not obvious, but since the error growth is small, this anomaly is not considered critical.

To quantify the differences, the position and velocity error state differences for the respective mean and 1σ value differences are calculated and presented in Tables 5-2 and 5-3.

Table 5-2
Reduced/CIRIS Position Error State Differences

Position Error States	Mean Difference		1σ Value Difference	
	Mean ft	1σ Value ft	Mean ft	1σ Value ft
Latitude	+1.66	10.26	-0.71	1.42
Longitude	+2.98	9.56	-0.58	1.29
Altitude	-15.89	83.46	+2.29	10.95
Note: All differences are Reduced - CIRIS				

The position error state difference means are well with the current CIRIS accuracies, indicating the increase in performance defined by these values as being reasonable. Since the residual characteristics of the reduced-order filter are identical to the "truth" model filter and both are closer to the ideal residual characteristics, the differences defined in this section indicate the magnitude of movement of the error state estimate in the reduced-order filter towards the true real world error.

The velocity error state differences are also similar in magnitude to the values calculated in Chapter 4 for the "truth" model. Again, these differences indicate a reasonable movement of the filter velocity error state estimates toward the true error in the real world.

Correlated Error Model Performance. The correlated measurement errors for 1 transponder are examined in this section for the entire flight. Transponder 181 is chosen for analysis. This transponder shares its assigned correlated error states with another transponder (transponder 163). The major thrust of this section is to examine the correlated errors' time history for the entire CIRIS flight and to note any transponder switching anomalies.

Table 5-3
Reduced/CIRIS Velocity Error State Differences

Velocity Error States	Mean Difference		1 σ Value Difference	
	Mean fps	1 σ Value fps	Mean fps	1 σ Value fps
North	-0.006	0.113	-0.024	0.011
West	-0.029	0.089	-0.041	0.013
Vertical	+0.000	0.521	+0.048	0.065

Note: All differences are Reduced - CIRIS

The range residuals for transponders 181 and 163 are shown in Figure 5-4. The characteristic statistics of both residuals are identical to the characteristics presented in Chapter 4 for the "truth" model. They are shown to identify the switching times from 181 to 163 for the correlated errors.

Transponder 163 is assigned to 181 because their measurements never overlap throughout the CIRIS flight. The 10 slot correlated measurement error window is large enough to allow sets of non-overlapping transponders to be identified and assigned to one of the slots for any number of transponders. The dashed lines in the figure indicate the times when each transponder measurements are being used by the filter. The dashed lines also indicate areas when the filter is not using either transponder.

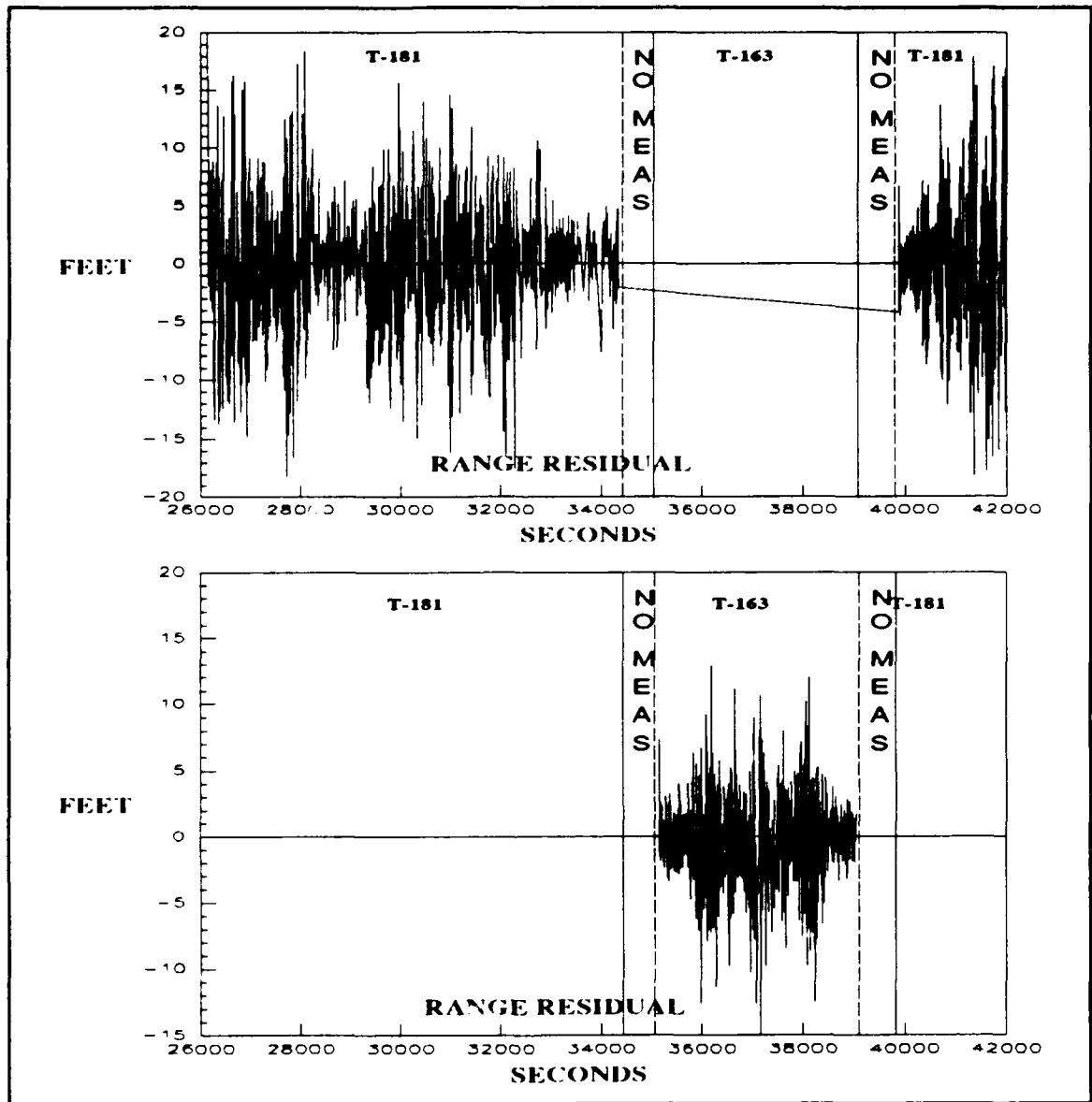


Figure 5-4. Range Residual T-181 and T-163

The correlated measurement error time histories from the filter exhibit both the error means and 1σ values for both transponders. The correlated measurement error plots for the X', Y', Z' transponder survey errors and the atmospheric error (ATM) in Figures 5-5 and 5-6.

Only one set of dashed lines is shown in these figure to indicate the approximate transitions from transponder 181 to 163. The areas when neither transponder is supplying measurements is small and lost in the transponder switching transient. The differences

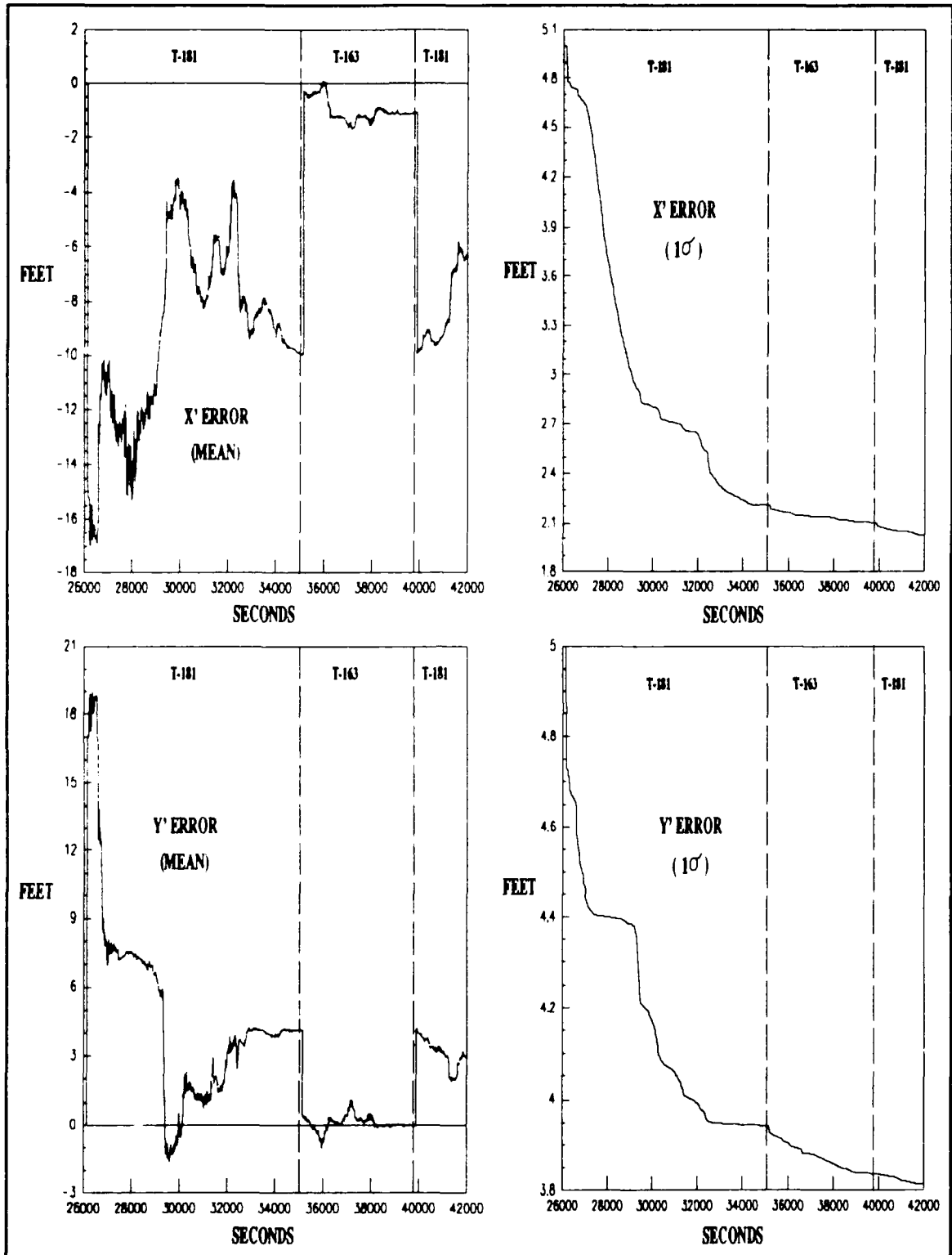


Figure 5-5. T-181/T-163 X' and Y' Correlated Errors

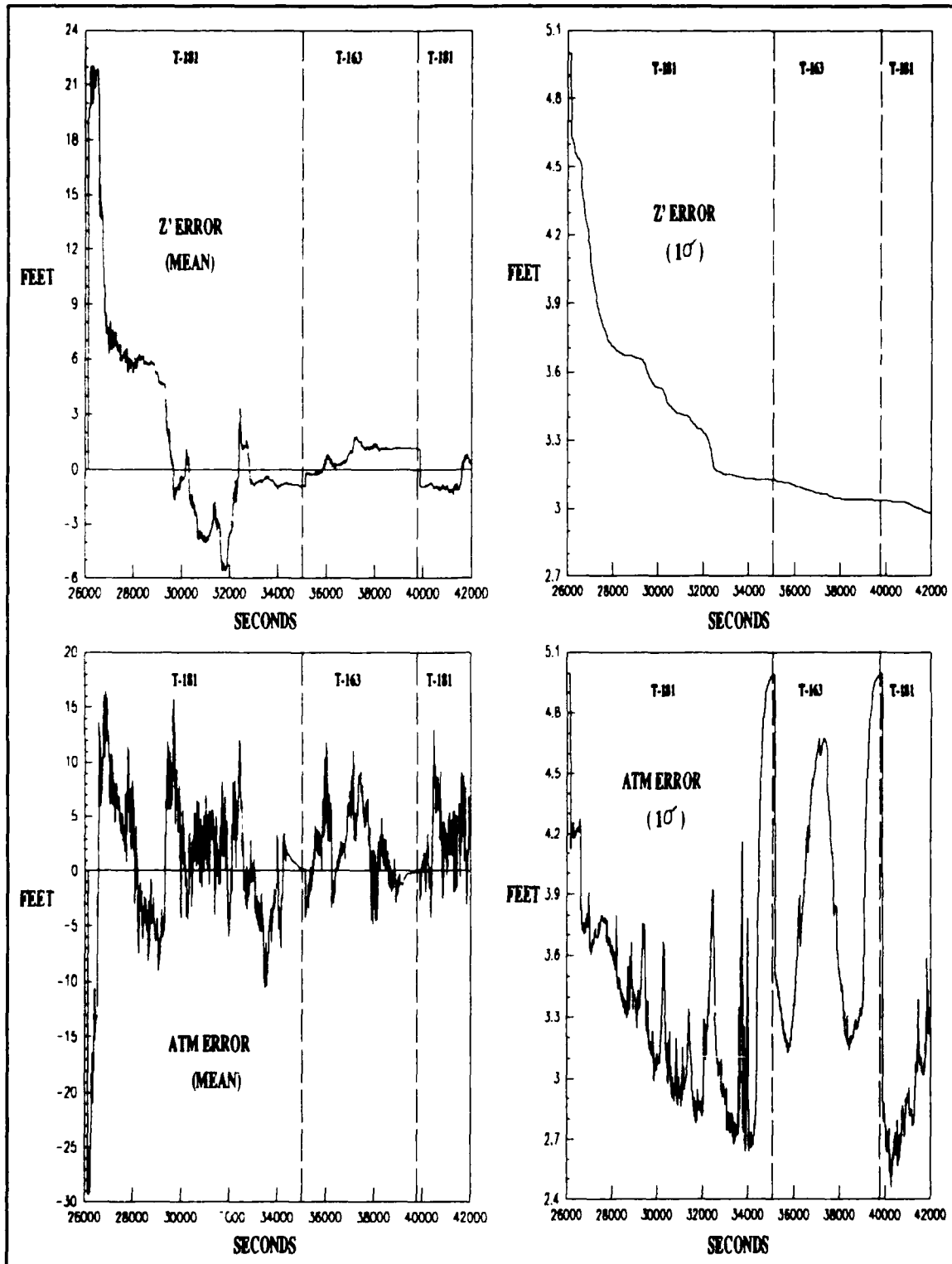


Figure 5-6. T-181/T-163 Z' and Atmospheric Correlated Errors

in the error state means is apparent between the two transponders. The 1σ value changes are less pronounced. This is due to the favorable transponder geometry when the switch takes place. This results in a small change in the filter's confidence in its estimate. The large transient at the beginning of flight is due to the unfavorable transponder geometry during takeoff and this characteristic is not expected to occur during inflight switching of transponders, as verified by these plots.

The general characteristics of the transponder survey and atmospheric errors are the same as those shown in Chapter 4. The magnitudes are very reasonable for the type of error being estimated. The transients when switching from 181 to 163 and back to 181 are clearly visible. The transients disappear very quickly as the filter begins tracking the error for the new transponder. The reinitialization of the covariance matrix and mean for these error states seems to work quite well. No anomalies are presents in this data.

Summary

In this chapter the reduced-order filter design is presented. The reasons for deleting the 57 INS error states are explained and the reduced-order filter model defined. The performance change is quantified by comparing the residuals, position error states, and velocity error states statistics between the "truth" and reduced-order filters.

A covariance analysis is considered for further tuning of the reduced-order filter and the reasons for rejecting this option explained. The reduced-order filter's performance is compared to the current CIRIS filter to quantify the performance gains. Finally, the correlated measurement errors for 2 transponders are examined for the entire CIRIS flight. Special attention is given to the transponder switching effects on the correlated measurement error mean and 1σ value time histories.

VI. Conclusions and Recommendations

This chapter restates the major goals of this research and the level of attainment for each. This analysis is integrated into the conclusions section that follows. Based on the results of this research, areas for future exploration and improvement are defined in the recommendations section.

Conclusions

The primary goal of this research effort is to develop a full ordered "truth" model which represents the errors found in the real world as close as possible. This goal is attained with both the 127-state and 70-state filters developed. This claim is based on how well the filter range and range rate residual statistics resemble the ideal residual statistics and the comparison to the current CIRIS filter error estimates and residuals.

The residual statistics for the 127-state and the 70-state filter are nearly identical. The residual statistics are very close to zero mean and the filter predicted 1σ value, indicating that the filter models are correctly estimating the real world errors. The current CIRIS residuals are found to be biased and with clearly visible correlated errors. The current CIRIS residuals' 1σ values are significantly different from the predicted filter 1σ values. *This indicates the position and velocity error state estimates for the 127-state and 70-state filters are closer to the true error.*

To quantify the increase in performance the differences between the "truth"/reduced order filter and current CIRIS filter, position and error state means are calculated and presented in Tables 6-1 and 6-2. The differences between the filter predicted 1σ values are not significant and not presented here.

The horizontal position error increase in accuracy is on the order of 2 ft for both the 127-state and 70-state filters. The vertical position error increase in accuracy is on the order of 20 ft for both filters. This increase in accuracy is well within the current CIRIS independently verified position accuracies. Therefore, the values obtained are very reasonable.

Table 6-1
"Truth"/Reduced/CIRIS Position Error State Differences

Position Error States	Mean Difference ("Truth" - CIRIS)		Mean Difference (Reduced - CIRIS)	
	Mean ft	1 σ Value ft	Mean ft	1 σ Value ft
Latitude	+2.11	10.55	+1.66	10.26
Longitude	+2.29	9.43	+2.98	9.56
Altitude	-20.61	83.49	-15.89	83.46
Note: All differences are Reduced/"Truth" - CIRIS				

The North velocity error increase in estimation accuracy is on the order of 0.005 fps for both the 127-state and 70-state filters. The West velocity error in estimation accuracy is 0.03 fps for both filters. The vertical velocity error increase in estimation accuracy is negligible for both filters. This increase in accuracy is well within the current CIRIS independently verified velocity accuracies. Therefore, the values obtained are reasonable.

The correlated measurement survey and atmospheric errors are observable to the filter and the filter is attempting to estimate these errors. The error mean and 1 σ values magnitudes seem reasonable for this type of error. At this time, there is no precise method of determining the accuracy of these estimates. However, based on the "whiteness" of the filter residuals, these estimates most likely are close to the real world errors.

The performance differences between the 127-state and 70-state filter are very small. However, the difference in required computer time is significant. Either model could serve as a "truth" model in the development of a Kalman filter that includes aiding measurements from the GPS system.

Table 6-2
 "Truth"/Reduced/CIRIS Velocity Error State Differences

Velocity Error States	Mean Difference ("Truth" - CIRIS)		Mean Difference (Reduced - CIRIS)	
	Mean fps	1 σ Value fps	Mean fps	1 σ Value fps
North	-0.002	0.105	-0.006	0.113
West	-0.029	0.104	-0.029	0.089
Vertical	+0.005	0.522	+0.000	0.521
Note: All differences are "Truth"/Reduced - CIRIS				

Recommendations

Additional CIRIS Flights. All the research in this thesis is based on the data from a single CIRIS flight. In order to validate this model, data from different CIRIS flights, with varying flight dynamics, should be processed with the filter. Ideally, a comparison of this data with data from a higher accuracy system would definitely define the true increase in accuracy. Only a differential GPS system or some other ground test system such as the high speed test track, can provide sufficiently accurate reference.

Correlated Errors. The correlated measurement model for the survey and atmospheric errors is providing estimates that appear reasonable for this type of error. Based on the data from more flights, these models may be tuned (initial conditions, correlation times, and noise strengths) to improve performance.

Filter Tuning. The "truth" models parameters (such as noise strengths, correlation times, and initial conditions) could be adjusted, using numerous CIRIS flights, to draw the residual statistics closer to the ideal statistics. The remaining increase in performance may be limited by hardware limitations (INS and RRS). Therefore the expected performance increase remaining through the tuning of this "truth" model is small.

The reduced order filter could be tuned using a covariance analysis to move the performance of the reduced order filter estimates closer to the "truth" model. Again, the differences between the "truth" and reduced order filters is small and this tuning may not be worth the effort.

Acceleration Data. The acceleration data directly available from the LN-39 INS is not being used to drive the filter model. Instead, the acceleration data is computed from the INS velocity data. There may be some benefits to using the raw INS acceleration data, especially in high flight dynamic environment. The benefit, if any, is unknown at this point.

Higher Sampling Rate. Currently measurement and INS data is processed at a 1 Hz rate due to computer limitations. This sampling rate seems adequate for the benign flight envelopes of the large cargo aircraft. However, when the CIRIS system is used in high dynamic fighters a higher sampling rate may allow the filter to accurately estimate the rapidly changing INS position and velocity errors. At this time the expected increase in performance cannot be estimated.

Smoothing Algorithm. The most promising way to increase the accuracy of the 127-state or 70-state filter is to implement the Kalman filter using a smoother algorithm. The smoothing algorithm utilizes a forward and backward Kalman filter to estimate the error states (17:1-5). This algorithm can only be used in post processing, but it takes into consideration the measurements for the entire flight when it makes its error estimates.

This algorithm would greatly reduce the areas of poor accuracy due to degraded transponder coverage. It would also do a better job estimating the transponder survey errors. This research direction will obtain the best results in the shortest time.

GPS Measurements. The 127-state or 70-state filters designed in this research effort more accurately estimate the INS position and velocity errors as is evident in a comparison of the range and range rate residuals. Therefore, either model can serve as a basis for the GPS aided CIRIS system. The filters designed in this thesis have the added benefit of providing a check on the transponder survey locations. If any of the transponder survey points is in error it would be flagged and the error estimated in the correlated survey error states.

The 70-state filter is recommended for the basis of GPS research. This is because of the large decrease in computer time and a negligible decrease in performance (as compared to the 127-state filter). The GPS research should be given higher priority over the tuning of the INS/Transponder filter. The only significant gains in accuracy, convergence, and reliability will be achieved when GPS measurements are added to the model. Initial work in this area is presented in Reference (20).

Appendix A

A Historical Review of the CIRIS Development and Operation

This appendix presents a brief review of the major characteristics of the CIRIS development and operation. This appendix is taken directly from References (11) and (12).

Introduction

The Completely Integrated Reference Instrumentation System (CIRIS) provides a highly accurate, real-time, position, velocity, and attitude reference for flight tests of inertial navigation, guidance, and radar systems. CIRIS was developed as an in-house project by the Central Inertial Guidance Test Facility (CIGTF) of Holloman AFB, New Mexico in 1975.

This airborne automated system is configured to be carried aboard both cargo and fighter testbed aircraft, and is also used in a mobile testing van. Utilizing ground-based transponders positioned in a triangular pattern along the flight path of the aircraft, the CIRIS provides reference coverage throughout most of the continental United States. This enables the testing of inertial systems over a very long distance and time duration. Position accuracies are provided at 13 ft (1σ) horizontal and 40 ft (1σ) vertical. Velocity accuracies are provided at 0.1 fps (1σ) horizontal and 0.4 fps (1σ) vertical. It provides the Department of Defense with a valuable airborne test facility for use in development and verification of inertial systems.

Past Reference Systems Compared to CIRIS

Air Force flight testing of inertial navigation systems began in 1965 at Holloman AFB, New Mexico. From 1965 to 1975 four primary methods were used by CIGTF in generating reference data: checkpoint, radar, cinetheodolite, and Doppler velocity. The checkpoint method utilizes an airborne vertical camera mounted in the testbed aircraft. High resolution photographs are taken of precisely surveyed landmarks. Post flight evaluation of the photographs, correlated with time and test system data, enabled the analyst to determine system errors. In the radar method, radar facilities are used to track the aircraft during a test, the data is correlated with the system data for evaluation. In the cinetheodolite method, cinetheodolite instrumentation (CINE) enables ground-based

precision-pointed cameras to track the aircraft. Picture analysis determines aircraft position and velocity. The Doppler Velocity and Positionary System (DOVAP) measures the incremental position changes based on the frequency shift of a signal between the aircraft transponder and ground-based receivers. Table A-1 summarizes the characteristics of these four reference systems and compares them with CIRIS.

Table A-1
Reference System Comparison

	Checkpoint	Radar	CINE	DOVAP	CIRIS
Position (ft)	50-200	50-100	5-15	15	13
Velocity (fps)	----	10-20	0.5-1.0	0.5	0.1
Attitude (arcmin)	----	----	-----	----	6
Data Available (days)	2-3	7	21	28	Real Time
Personnel Req'd	2	10	10	20	1
Weather Dep.	Yes	No	Yes	No	No
Coverage (mins) - North-South*	> 84**	42	6	20	> 84
East-West	> 84	84	2	5	> 84
* Assume constant track starting at Holloman AFB, NM, 300-400 Knots groundspeed.					
** 84 minute is defined as the Schuler period. Test durations are measured in increments of Schuler periods.					

Development of CIRIS

The data presented in Table 1 indicates the reference systems, used prior to CIRIS, involved long time data turnaround, limited the range of testing, and often used more support personnel. These facts combined with advances in digital techniques, specifically Kalman filtering, led to the conceptualization of a self-contained, real-time airborne reference system. The CIRIS system was developed as an in-house project of CIGTF. The CIRIS development effort was completed in March 1975 with four verification flight

tests conducted over the White Sands Missile Range. Dense transponder coverage combined with extensive CINE data verified the CIRIS position accuracy. Since this time CIRIS has been reconfigured for fighter and B52 aircraft, and is used heavily for inertial system's flight testing.

CIRIS in an Operational Flight Test

CIRIS is configured for installation in NC130, NC141, B52, and RF-4C testbed aircraft. On board cargo aircraft CIRIS is installed on a pallet along with four test system pallets. In the RF-4C the CIRIS is modified for containment in a pod secured to the aircraft. Two test systems are carried on board the F-4. All test systems are time synchronized with CIRIS for data correlation. The actual flight is conducted over areas where CIRIS transponders are positioned in a triangular pattern, 100-200 miles apart. This reference system provides steering information to the aircrew to fly precise ground tracks. Transponder ranges are available at many different locations throughout the United States land mass. CIRIS personnel are also able to reposition ground based transponders to provide coverage in a specific area of test activity. New transponder sites need only be surveyed prior to placement of the transponder units. Routes and area can change subject to test activity in that region.

CIRIS System Description

The major components of CIRIS are the Inertial Navigation System (INS), the Air Data Computer (ADC), the Radio-Range/Range Rate/Interrogator System (RRS), and the time generator interface with the CIRIS computer. There are currently two versions of CIRIS being used designated CIRIS I and CIRIS II.

The Litton LN-15 INS, a Sperry ADC, the Cubic RRS, and a 11-state Kalman filter (initially designed by Intermetrics) are used in CIRIS I to combine all the available data to produce the most accurate aircraft trajectory data possible. The Sperry ADC provides

barometric altitude to the INS for vertical channel stabilization. The Kalman filter combines the INS position, velocity, and acceleration data; the barometric altimeter data; and the very accurate line-of-sight range and range rate measurements from the Cubic RRS to estimate the error in the INS position and velocity data. These Kalman filter estimated errors are used to correct the INS data trajectory data. The CIRIS filter algorithm is implemented on a Hewlet Packard HP2100 minicomputer.

A mass producible high reliability and maintainability improvement to the previous CIRIS I design resulted in an improved system designated CIRIS II. This system was developed and fabricated by the Navigational Reference Branch (GDN). Its old INS is replaced with the newer, depot supported LN-39 INS. It also removes the non-standard computer interface to the old INS and replaces a non-available ADC with a depot supported F-16 ADC. The accuracy of CIRIS I and CIRIS II are identical, only the reliability and maintainability of the CIRIS II system is increased.

CIRIS Applications

With its ability to be used anywhere, dependent only upon positioning of transponders, CIRIS has been heavily used in the past. Flight testing of inertial navigation systems for the A-10, B-52, F-15, F-16, B-1, and KC135 have been accomplished using CIRIS as the reference. A GPS system was tested onboard a C141 with CIRIS providing reference data. Currently CIRIS is extensively used in testing strapdown systems by CIGTF, as well as being used in the B52 upgrade (B52-OAS Program). Evaluation of mid course and terminal guidance systems use CIRIS not only as the reference, but as a source of data for in flight alignment prior to simulated weapons delivery.

The fighter CIRIS is completely automated thus insuring optimum reference data in high g-force fighter tactics environment. Plans to miniaturize the CIRIS call for installation of microcomputer and cassette type recording system. The fighter CIRIS is

being configured for the F-15B testbed aircraft and more efficient cooling for the fighter unit is also in research. Placement of more transponder units is increasing range and capability of CIRIS. CIRIS engineers are constantly modifying software to meet requirements for both standard and special test programs. Plans for GPS update of CIRIS in minimal transponder coverage are also seen in the CIRIS future. Research sponsored by CIGTF is conducted by the Air Force Institute of Technology (AFIT) to quantify the gains in filter error estimation accuracy possible by adding GPS aiding measurements to CIRIS.

In summary, CIRIS is a valuable tool in the testing of inertial systems. The highly accurate, real-time reference data provides the Air Force and Department of Defense with a standard by which commercially built inertial systems can be verified and new systems can be developed and tested.

Appendix B

Initial Covariance, Noise Strengths, and Dynamics Matrix Elements for the INS "Truth" Model

This appendix defines the elements of the initial covariance matrix for the INS "truth" model. The diagonal matrix $P_{INS}(t_0)$ is shown in Eq (3-6). The submatrices P_{11} thru P_{66} are also diagonal matrices. The 1σ error values for each diagonal element are defined in Tables B-1 thru B-9. Note that the actual covariance diagonal element is equal to σ_{ii}^2 .

The elements of the initial noise strength matrix are also defined. The block diagonal matrix, $Q_{INS}(t_0)$, is shown in Eq (3-7). The nonzero block diagonal elements (Q_{11} and Q_{22}) are also diagonal matrices. The diagonal element values are defined in Tables B-10 thru B-11 with the applicable parameters defined in Chapter 3.

Finally, the nonzero elements of the F_{INS} matrix are defined. The structure of this matrix is shown in Eq (3-3). The submatrices F_{11} thru F_{66} are defined in Tables B-12 thru B-24 with the applicable parameters defined in Chapter 3.

Table B-1
Definition of Submatrix P₁₁

Element	State	Definition	Value (1 σ)
1,1	$\delta\Theta_x$	Magnitude of error between the true frame's X axis and the computer frame's X axis.	0.0 arcsecs
2,2	$\delta\Theta_y$	Magnitude of error between the true frame's Y axis and the computer frame's Y axis.	0.0 arcsecs
3,3	$\delta\Theta_z$	Magnitude of error between the true frame's Z axis and the computer frame's Z axis.	0.0 arcsecs
4,4	ϕ_x	Magnitude of error between the true frame's X axis and the platform frame's X axis.	100 arcsecs
5,5	ϕ_y	Magnitude of error between the true frame's Y axis and the platform frame's Y axis.	100 arcsecs
6,6	ϕ_z	Magnitude of error between the true frame's Z axis and the platform frame's Z axis.	180 arcmins
7,7	δV_x	Magnitude of error between the true X velocity and the computer X velocity.	0 fps
8,8	δV_y	Magnitude of error between the true Y velocity and the computer Y velocity.	0 fps
9,9	δV_z	Magnitude of error between the true Z velocity and the computer Z velocity.	0 fps
10,10	δH	Magnitude of error between the true altitude and the computer altitude.	0 ft
11,11	δH_L	Magnitude of error between the true altitude and the computer altitude (1 sec delay).	0 ft
12,12	δS_3	Magnitude of vertical channel aiding state.	0 ft
13,13	δS_4	Magnitude of vertical channel aiding state.	0 fps ²
<i>All other elements are zero.</i>			

Table B-2
Definition of Submatrix P_{22}

Element	State	Definition	Value (1 σ)
14,14	B_{XC}	Magnitude of gyro correlated drift rate along X axis.	0.002 deg/hr
15,15	B_{YC}	Magnitude of gyro correlated drift rate along Y axis.	0.002 deg/hr
16,16	B_{ZC}	Magnitude of gyro correlated drift rate along Z axis.	0.005 deg/hr
17,17	Δ_{XC}	Magnitude of accelerometer and velocity quantizer correlated noise along X axis.	3 μg
18,18	Δ_{YC}	Magnitude of accelerometer and velocity quantizer correlated noise along Y axis.	3 μg
19,19	Δ_{ZC}	Magnitude of accelerometer and velocity quantizer correlated noise along Z axis.	3 μg
20,20	δG_X	Magnitude of gravity vector error along X axis.	35 μg
21,21	δG_Y	Magnitude of gravity vector error along Y axis.	35 μg
22,22	δG_Z	Magnitude of gravity vector error along Z axis.	35 μg
23,23	δH_C	Magnitude of baro-altimeter correlated bias noise.	100 ft

All other elements are zero.

Table B-3
Definition of Submatrix P_{33a}

Element	State	Definition	Value (1 σ)
24,24	B_X	Magnitude of gyro drift rate bias repeatability along X axis.	0.0045 deg/hr
25,25	B_Y	Magnitude of gyro drift rate bias repeatability along Y axis.	0.0045 deg/hr
26,26	B_Z	Magnitude of gyro drift rate bias repeatability along Z axis.	0.01 deg/hr
27,27	S_{GX}	Magnitude of gyro torquing scale factor error along X axis.	0.021 %
28,28	S_{GY}	Magnitude of gyro torquing scale factor error along Y axis.	0.021 %
29,29	S_{GZ}	Magnitude of gyro torquing scale factor error along Z axis.	0.021 %
30,30	X_1	Magnitude of gyro misalignment about Y axis.	7 arcsec
31,31	X_2	Magnitude of gyro misalignment about X axis.	7 arcsec
32,32	X_3	Magnitude of gyro misalignment about X axis.	7 arcsec
33,33	N_1	Magnitude of gyro misalignment about Z axis.	7 arcsec
34,34	N_2	Magnitude of gyro misalignment about Z axis.	7 arcsec
35,35	N_3	Magnitude of gyro misalignment about Y axis.	7 arcsec

Table B-4
Definition of Submatrix P_{33b}

Element	State	Definition	Value (1 σ)
36,36	H_{XX}	Magnitude of error due to gyro mass imbalance along X axis (g-sensitivity).	0.016 deg/hr/g
37,37	H_{YY}	Magnitude of error due to gyro mass imbalance along Y axis (g-sensitivity).	0.016 deg/hr/g
38,38	H_{ZZ}	Magnitude of error due to gyro mass imbalance along Z axis (g-sensitivity).	0.016 deg/hr/g
39,39	H_{XY}	Magnitude of error due to gyro quadrature along X axis (g-sensitivity).	0.015 deg/hr/g
40,40	H_{YX}	Magnitude of error due to gyro quadrature along Y axis (g-sensitivity).	0.015 deg/hr/g
41,41	H_{ZY}	Magnitude of error due to gyro quadrature along Z axis (g-sensitivity).	0.015 deg/hr/g
42,42	K_{XZ}	Magnitude of error due to gyro anisoelasticity along X axis (g^2 -sensitivity).	0.02 deg/hr/ g^2
43,43	K_{YZ}	Magnitude of error due to gyro anisoelasticity along Y axis (g^2 -sensitivity).	0.02 deg/hr/ g^2
44,44	K_{ZX}	Magnitude of error due to gyro anisoelasticity along Z axis (g^2 -sensitivity).	0.02 deg/hr/ g^2
<i>All other elements are zero.</i>			

Table B-5
Definition of Submatrix P₄₄

Element	State	Definition	Value (1 σ)
45,45	Δ_{BX}	Magnitude of accelerometer bias repeatability along X axis.	200 μg
46,46	Δ_{BY}	Magnitude of accelerometer bias repeatability along Y axis.	200 μg
47,47	Δ_{BZ}	Magnitude of accelerometer bias repeatability along Z axis.	200 μg
48,48	S_{Ax}	Magnitude of accelerometer and velocity quantizer scale factor error along X axis.	0.023 %
49,49	S_{Ay}	Magnitude of accelerometer and velocity quantizer scale factor error along Y axis.	0.023 %
50,50	S_{Az}	Magnitude of accelerometer and velocity quantizer scale factor error along Z axis.	0.023 %
51,51	S_{QA_x}	Magnitude of accelerometer and velocity quantizer scale factor asymmetry error along X axis.	0.01 %
52,52	S_{QA_y}	Magnitude of accelerometer and velocity quantizer scale factor asymmetry error along Y axis.	0.01 %
53,53	S_{QA_z}	Magnitude of accelerometer and velocity quantizer scale factor asymmetry error along Z axis.	0.01 %
54,54	S_{Qx_2}	Magnitude of accelerometer and velocity nonlinear quantizer scale factor asymmetry error along X axis.	3 $\mu g/g^2$
55,55	S_{Qy_2}	Magnitude of accelerometer and velocity nonlinear quantizer scale factor asymmetry error along Y axis.	3 $\mu g/g^2$
56,56	S_{Qz_2}	Magnitude of accelerometer and velocity nonlinear quantizer scale factor asymmetry error along Z axis.	3 $\mu g/g^2$

Table B-6
Definition of Submatrix P_{44b}

Element	State	Definition	Value (1 σ)
57,57	F_{XX}	Magnitude of error proportional to the square of the measured acceleration along X axis.	8 $\mu g/g^2$
58,58	F_{YY}	Magnitude of error proportional to the square of the measured acceleration along Y axis.	8 $\mu g/g^2$
59,59	F_{ZZ}	Magnitude of error proportional to the square of the measured acceleration along Z axis.	8 $\mu g/g^2$
60,60	F_{XY}	Magnitude of error proportional to products of acceleration along and orthogonal to sensitive axes of accelerometers (XZ).	33 $\mu g/g^2$
61,61	F_{XZ}	Magnitude of error proportional to products of acceleration along and orthogonal to sensitive axes of accelerometers (XY).	33 $\mu g/g^2$
62,62	F_{YX}	Magnitude of error proportional to products of acceleration along and orthogonal to sensitive axes of accelerometers (YZ).	33 $\mu g/g^2$
63,63	F_{YZ}	Magnitude of error proportional to products of acceleration along and orthogonal to sensitive axes of accelerometers (YX).	33 $\mu g/g^2$
64,64	F_{ZX}	Magnitude of error proportional to products of acceleration along and orthogonal to sensitive axes of accelerometers (ZX).	33 $\mu g/g^2$
65,65	F_{ZY}	Magnitude of error proportional to products of acceleration along and orthogonal to sensitive axes of accelerometers (ZY).	33 $\mu g/g^2$

Table B-7
Definition of Submatrix P_{44c}

Element	State	Definition	Value (1 σ)
66,66	μ_1	Magnitude of error due to accelerometer misalignment along X axis (mean).	7 arcsec
67,67	μ_2	Magnitude of error due to accelerometer misalignment along Y axis (mean).	7 arcsec
68,68	μ_3	Magnitude of error due to accelerometer misalignment along Z axis (mean).	7 arcsec
69,69	σ_1	Magnitude of error due to accelerometer misalignment along X axis (1 sigma).	7 arcsec
70,70	σ_2	Magnitude of error due to accelerometer misalignment along Y axis (1 sigma).	7 arcsec
71,71	σ_3	Magnitude of error due to accelerometer misalignment along Z axis (1 sigma).	7 arcsec
72,72	δH_B	Magnitude of baro-altimeter bias error.	300 ft
73,73	δH_{SF}	Magnitude of baro-altimeter scale factor error.	4 %
<i>All other elements are zero.</i>			

Table B-8
Definition of Submatrix P₅₅

Element	State	Definition	Value (1 σ)
74,74	Δ_{xQ}	Magnitude of initial accelerometer bias thermal transient error along X axis.	200 μg
75,75	Δ_{yQ}	Magnitude of initial accelerometer bias thermal transient error along Y axis.	200 μg
76,76	Δ_{zQ}	Magnitude of initial accelerometer bias thermal transient error along Z axis.	200 μg
77,77	B_{xQ1}	Magnitude of initial gyro drift rate bias thermal transient along X axis (component 1).	0.33 deg/hr
78,78	B_{xQ2}	Magnitude of initial gyro drift rate bias thermal transient along X axis (component 2).	0.01 deg/hr
79,79	B_{yQ1}	Magnitude of initial gyro drift rate bias thermal transient along Y axis (component 1).	0.33 deg/hr
80,80	B_{yQ2}	Magnitude of initial gyro drift rate bias thermal transient along Y axis. (component 2).	0.01 deg/hr
81,81	B_{zQ1}	Magnitude of initial gyro drift rate bias thermal transient along Z axis (component 1).	0.33 deg/hr
82,82	B_{zQ2}	Magnitude of initial gyro drift rate bias thermal transient along Z axis (component 2).	0.01 deg/hr
<i>All other elements are zero.</i>			

Table B-9
Definition of Submatrix P₆₆

Element	State	Definition	Value (1 σ)
83,83	B_{XTA}	Magnitude of gyro turn-around drift rate along X axis.	0.002 deg/hr
84,84	B_{YTA}	Magnitude of gyro turn-around drift rate along X axis.	0.002 deg/hr
85,85	B_{ZTA}	Magnitude of gyro turn-around drift rate along X axis.	0.005 deg/hr
<i>All other elements are zero.</i>			

Table B-10
Definition of Submatrix Q_{11}

Element	State	Definition	Value
4,4	Φ_x	Magnitude of gyro drift rate white noise along X axis.	$\sigma_{\eta_{B_x}}^2$
5,5	Φ_y	Magnitude of gyro drift rate white noise along Y axis.	$\sigma_{\eta_{B_y}}^2$
6,6	Φ_z	Magnitude of gyro drift rate white noise along Z axis.	$\sigma_{\eta_{B_z}}^2$
7,7	δV_x	Magnitude of accelerometer white noise along X axis.	$\sigma_{\eta_{A_x}}^2$
8,8	δV_y	Magnitude of accelerometer white noise along Y axis.	$\sigma_{\eta_{A_y}}^2$
9,9	δV_z	Magnitude of accelerometer white noise along Z axis.	$\sigma_{\eta_{A_z}}^2$
13,13	δS_4	Magnitude of vertical aiding channel white noise component.	$2 K_4^2 \beta_{\delta H_c} \sigma_{\delta H_c}^2$
<i>All other elements are zero.</i>			

Table B-11
Definition of Submatrix Q_{22}

Element	State	Definition	Value
14,14	B_{XC}	Magnitude of white noise along X axis.	$2\beta_{B_{XC}} \sigma_{B_{XC}}^2$
15,15	B_{YC}	Magnitude of white noise along Y axis.	$2\beta_{B_{YC}} \sigma_{B_{YC}}^2$
16,16	B_{ZC}	Magnitude of white noise along Z axis.	$2\beta_{B_{ZC}} \sigma_{B_{ZC}}^2$
17,17	Δ_{XC}	Magnitude of white noise along X axis.	$2\beta_{\Delta_{XC}} \sigma_{\Delta_{XC}}^2$
18,18	Δ_{YC}	Magnitude of white noise along Y axis.	$2\beta_{\Delta_{YC}} \sigma_{\Delta_{YC}}^2$
19,19	Δ_{ZC}	Magnitude of white noise along Z axis.	$2\beta_{\Delta_{ZC}} \sigma_{\Delta_{ZC}}^2$
20,20	δG_X	Magnitude of white noise along X axis.	$2\beta_{\delta G_X} \sigma_{\delta G_X}^2$
21,21	δG_Y	Magnitude of white noise along Y axis.	$2\beta_{\delta G_Y} \sigma_{\delta G_Y}^2$
22,22	δG_Z	Magnitude of white noise along Z axis.	$2\beta_{\delta G_Z} \sigma_{\delta G_Z}^2$
23,23	δH_C	Magnitude of baro-altimeter correlated bias white noise.	$2\beta_{\delta H_C} \sigma_{\delta H_C}^2$
<i>All other elements are zero.</i>			

Table B-12
Definition of Submatrix F_{11}

	1	2	3	4	5	6
	$\delta\theta_x$	$\delta\theta_y$	$\delta\theta_z$	ϕ_x	ϕ_y	ϕ_z
1	$\delta\dot{\theta}_x$		$-\omega_{EPY}$			
2	$\delta\dot{\theta}_y$		ω_{EPX}			
3	$\delta\dot{\theta}_z$	$-\omega_{EPX}$				
4	$\dot{\phi}_x$	$-\omega_{IEZ}$	ω_{IEY}		ω_{IPZ}	$-\omega_{IPY}$
5	$\dot{\phi}_y$		$-\omega_{IEX}$	$-\omega_{IPZ}$		ω_{IPX}
6	$\dot{\phi}_z$	ω_{IEY}		ω_{IPY}	$-\omega_{IPX}$	
7	$\delta\dot{V}_x$	$2V_Y\omega_{IEX}$ $-2V_Z\omega_{IEZ}$	$2V_Z\omega_{IEX}$		$-A_z$	A_y
8	$\delta\dot{V}_y$	$2V_X\omega_{IEY}$	$2V_Z\omega_{IEY}$	A_z		$-A_x$
9	$\delta\dot{V}_z$	$2V_X\omega_{IEZ}$	$-2V_Y\omega_{IEY}$ $-2V_X\omega_{IEX}$	$-A_y$	A_x	
10	$\delta\dot{H}$					
11	$\delta\dot{H}_L$					
12	$\delta\dot{\delta}_3$					
13	$\delta\dot{\delta}_4$					

Table B-13
Definition of Submatrix F_{116}

	7	8	9	10	11	12	13
1	$\delta\dot{\theta}_x$	δV_y	δV_z	δH	δH_L	δS_3	δS_4
2	$\delta\dot{\theta}_y$	$-C_{RY}$					
3	$\delta\dot{\theta}_z$	C_{RX}					
4	$\dot{\phi}_x$	$-C_{RY}$					
5	$\dot{\phi}_y$	C_{RX}					
6	$\dot{\phi}_z$						
7	$\delta\dot{V}_x$	$-V_z C_{RX}$	$2\omega_{JEZ}$	$2\omega_{JEZ}$	$-\omega_{EPY} - 2\omega_{JEY}$		
8	$\delta\dot{V}_y$	$-2\omega_{JEZ}$	$-V_z C_{RY}$	$-\omega_{EPX} + 2\omega_{JEX}$			
9	$\delta\dot{V}_z$	$\omega_{EPY} + 2\omega_{JEY}$ $+V_x C_{RX}$	$-\omega_{EPX} - 2\omega_{JEX}$ $+V_y C_{RY}$	$\frac{2G_0}{A}$	$-K_2$	-1.0	K_2
10	$\delta\dot{H}$		1.0		$-K_1$		$K_1 - 1.0$
11	$\delta\dot{H}_L$			1.0	-1.0		
12	$\delta\dot{S}_3$				K_3		$-K_3$
13	$\delta\dot{S}_4$			K_4	$-K_4$		$K_4 - 1.0$

Table B-14
Definition of Submatrix F_{12}

	14	15	16	17	18	19	20	21	22	23
1	B_{XC}									
2		B_{YC}								
3			B_{ZC}							
4	1.0			Δ_{XC}						
5		1.0			Δ_{YC}					
6			1.0			Δ_{ZC}				
7				1.0			1.0			
8					1.0			1.0		
9						1.0			1.0	
10										K_2
11										K_1
12										$-K_3$
13										$K_4 \delta \beta_{Hc}$

Table B-15
Definition of Submatrix F_{13}

	24	25	26	27	28	29	30	31	32	33	34	35
	B_x	B_y	B_z	S_{GX}	S_{GY}	S_{GZ}	X_1	X_2	X_3	N_1	N_2	N_3
1	$\delta\dot{\theta}_x$											
2	$\delta\dot{\theta}_y$											
3	$\delta\dot{\theta}_z$											
4	$\dot{\phi}_x$	1.0		ω_{PX}			ω_{PZ}			$-\omega_{PY}$		
5	$\dot{\phi}_y$	1.0		ω_{PY}				$-\omega_{PZ}$			ω_{PX}	
6	$\dot{\phi}_z$		1.0			ω_{PZ}			ω_{PY}			$-\omega_{PX}$
7	$\delta\dot{V}_x$											
8	$\delta\dot{V}_y$											
9	$\delta\dot{V}_z$											
10	$\delta\dot{H}$											
11	$\delta\dot{H}_L$											
12	$\delta\dot{S}_3$											
13	$\delta\dot{S}_4$											

Table B-16
Definition of Submatrix F_{136}

	36	37	38	39	40	41	42	43	44
1	H_{xx}								
2		H_{yy}							
3			H_{zz}						
4	A_x			A_y			$A_x A_z$		
5		A_y			A_x			$A_y A_z$	
6			A_z			$\frac{A_y - A_x}{\sqrt{2}}$			$\frac{(A_x + A_y)A_z}{\sqrt{2}}$
7	$\delta\dot{\theta}_x$								
8	$\delta\dot{\theta}_y$								
9	$\delta\dot{\theta}_z$								
10	$\delta\dot{H}$								
11	$\delta\dot{H}_L$								
12	$\delta\dot{S}_3$								
13	$\delta\dot{S}_4$								

Table B-17
Definition of Submatrix F_{14}

	45	46	47	48	49	50	51	52	53	54	55	56
1	$\delta\dot{\theta}_x$											
2	$\delta\dot{\theta}_y$											
3	$\delta\dot{\theta}_z$											
4	$\dot{\phi}_x$											
5	$\dot{\phi}_y$											
6	$\dot{\phi}_z$											
7	$\delta\dot{V}_x$	1.0		A_x		S_{A_z}	S_{QA_x}	S_{QA_y}	S_{QA_z}	$S_{Q_{xz}}$	$S_{Q_{rz}}$	$S_{Q_{zz}}$
8	$\delta\dot{V}_y$		1.0		A_y			$ A_y $			$A_y A_y $	
9	$\delta\dot{V}_z$			1.0		A_z			$ A_z $			$A_z A_z $
10	$\delta\dot{H}$											
11	$\delta\dot{H}_L$											
12	$\delta\dot{S}_3$											
13	$\delta\dot{S}_4$											

Table B-18
Definition of Submatrix F_{146}

	57	58	59	60	61	62	63	64	65
	F_{xx}	F_{yy}	F_{zz}	F_{xy}	F_{xz}	F_{yx}	F_{yz}	F_{zx}	F_{zy}
1	$\delta\theta_x$								
2	$\delta\theta_y$								
3	$\delta\theta_z$								
4	ϕ_x								
5	ϕ_y								
6	ϕ_z								
7	$\delta\dot{V}_x$	A_x^2		$A_x A_y$	$A_x A_z$				
8	$\delta\dot{V}_y$		A_y^2			$A_y A_x$	$A_y A_z$		
9	$\delta\dot{V}_z$		$(A_z)^2$					$A_x A_z$	$A_y A_z$
10	$\delta\dot{H}$								
11	$\delta\dot{H}_L$								
12	$\delta\dot{S}_3$								
13	$\delta\dot{S}_4$								

Table B-19
Definition of Submatrix F_{14c}

	66	67	68	69	70	71	72	73
1	$\delta\theta_x$							
2	$\delta\theta_y$							
3	$\delta\theta_z$							
4	$\dot{\phi}_x$							
5	$\dot{\phi}_y$							
6	$\dot{\phi}_z$							
7	$\delta\dot{V}_x$	A_y		$-A_z$				
8	$\delta\dot{V}_y$	$-A_x$			A_z			
9	$\delta\dot{V}_z$		A_y			A_x	K_2	HK_2
10	$\delta\dot{H}$						K_1	HK_1
11	$\delta\dot{H}_L$							
12	$\delta\dot{S}_3$						$-K_3$	$-HK_3$
13	$\delta\dot{S}_4$							$-K_4V_z$

Table B-20
Definition of Submatrix F_{15}

	74	75	76	77	78	79	80	81	82
1	Δ_{xQ}								
2		Δ_{yQ}							
3			Δ_{zQ}						
4				B_{xQ1}	B_{xQ2}				
5				1.0	1.0				
6						1.0	1.0		
7	δV_x							1.0	1.0
8	δV_y	1.0							
9	δV_z		1.0						
10	δH								
11	δH_L								
12	δS_3								
13	δS_4								

Table B-21
Definition of Submatrix F_{16}

		83	84	85
1	$\delta\dot{\theta}_x$	B_{xTA}	B_{yTA}	B_{zTA}
2	$\delta\dot{\theta}_y$			
3	$\delta\dot{\theta}_z$			
4	$\dot{\phi}_x$	1.0		
5	$\dot{\phi}_y$		1.0	
6	$\dot{\phi}_z$			1.0
7	$\delta\dot{V}_x$			
8	$\delta\dot{V}_y$			
9	$\delta\dot{V}_z$			
10	$\delta\dot{H}$			
11	$\delta\dot{H}_L$			
12	$\delta\dot{S}_3$			
13	$\delta\dot{S}_4$			

Table B-24
Definition of Submatrix F_{66}

		83	84	85
		B_{XTA}	B_{YTA}	B_{ZTA}
83	\dot{B}_{XTA}	0.0		
84	\dot{B}_{YTA}		0.0	
85	\dot{B}_{ZTA}			0.0

Appendix C
Initial Covariance, Noise Strengths, Dynamics Matrix,
and Measurement Gradient Matrix Elements
for the Measurement "Truth" Model

This appendix defines the elements of the initial covariance matrix for the measurement "truth" model. $P_{MEAS}(t_0)$ is a diagonal matrix and is shown in Eq (4-15). The submatrices P_{MEASs} thru P_{MEASd} are also diagonal matrices. The 1σ error values for each diagonal element are defined in Tables C-1 thru C-4. Note that the actual covariance element is equal to σ^2 .

The elements of the initial noise strength matrix are also defined. $Q_{MEAS}(t_0)$ is a diagonal matrix and is shown in Eq (4-15). The nonzero diagonal element values are defined in Table C-5.

The nonzero elements of the F_{MEAS} matrix are defined. The nonzero elements are defined in Table C-6.

The nonzero elements of the H_R and H_{RR} matrices are defined. The nonzero elements are defined in Tables C-7 and C-8.

Table C-1
Definition of Submatrix P_{MEAS}

Element	State	Definition	Value (1 σ)
86,86	δE_{CALR}	Magnitude of the transponder interrogator calibration error (range measurement).	1 ft
87,87	δX_{T_1}	Magnitude of transponder 1 survey error (X'-axis).	5 ft
88,88	δY_{T_1}	Magnitude of transponder 1 survey error (Y'-axis).	5 ft
89,89	δZ_{T_1}	Magnitude of transponder 1 survey error (Z'-axis).	5 ft
90,90	δE_{ATM_1}	Magnitude of transponder 1 atmospheric error (line of sight).	5 ft
91,91	δX_{T_2}	Magnitude of transponder 2 survey error (X'-axis).	5 ft
92,92	δY_{T_2}	Magnitude of transponder 2 survey error (Y'-axis).	5 ft
93,93	δZ_{T_2}	Magnitude of transponder 2 survey error (Z'-axis).	5 ft
94,94	δE_{ATM_2}	Magnitude of transponder 2 atmospheric error (line of sight).	5 ft
95,95	δX_{T_3}	Magnitude of transponder 3 survey error (X'-axis).	5 ft
96,96	δY_{T_3}	Magnitude of transponder 3 survey error (Y'-axis).	5 ft
97,97	δZ_{T_3}	Magnitude of transponder 3 survey error (Z'-axis).	5 ft
98,98	δE_{ATM_3}	Magnitude of transponder 3 atmospheric error (line of sight).	5 ft

Table C-2
Definition of Submatrix P_{MEASb}

Element	State	Definition	Value (1 σ)
99,99	δX_{T_4}	Magnitude of transponder 4 survey error (X'-axis).	5 ft
100,100	δY_{T_4}	Magnitude of transponder 4 survey error (Y'-axis).	5 ft
101,101	δZ_{T_4}	Magnitude of transponder 4 survey error (Z'-axis).	5 ft
102,102	δE_{ATM_4}	Magnitude of transponder 4 atmospheric error (line of sight).	5 ft
103,103	δX_{T_5}	Magnitude of transponder 5 survey error (X'-axis).	5 ft
104,104	δY_{T_5}	Magnitude of transponder 5 survey error (Y'-axis).	5 ft
105,105	δZ_{T_5}	Magnitude of transponder 5 survey error (Z'-axis).	5 ft
106,106	δE_{ATM_5}	Magnitude of transponder 5 atmospheric error (line of sight).	5 ft
107,107	δX_{T_6}	Magnitude of transponder 6 survey error (X'-axis).	5 ft
108,108	δY_{T_6}	Magnitude of transponder 6 survey error (Y'-axis).	5 ft
109,109	δZ_{T_6}	Magnitude of transponder 6 survey error (Z'-axis).	5 ft
110,110	δE_{ATM_6}	Magnitude of transponder 6 atmospheric error (line of sight).	5 ft

Table C-3
Definition of Submatrix P_{MEASc}

Element	State	Definition	Value (1 σ)
111,111	δX_T	Magnitude of transponder 7 survey error (X'-axis).	5 ft
112,112	δY_T	Magnitude of transponder 7 survey error (Y'-axis).	5 ft
113,113	δZ_T	Magnitude of transponder 7 survey error (Z'-axis).	5 ft
114,114	δE_{ATM}	Magnitude of transponder 7 atmospheric error (line of sight).	5 ft
115,115	δX_T	Magnitude of transponder 8 survey error (X'-axis).	5 ft
116,116	δY_T	Magnitude of transponder 8 survey error (Y'-axis).	5 ft
117,117	δZ_T	Magnitude of transponder 8 survey error (Z'-axis).	5 ft
118,118	δE_{ATM}	Magnitude of transponder 8 atmospheric error (line of sight).	5 ft
119,119	δX_T	Magnitude of transponder 9 survey error (X'-axis).	5 ft
120,120	δY_T	Magnitude of transponder 9 survey error (Y'-axis).	5 ft
121,121	δZ_T	Magnitude of transponder 9 survey error (Z'-axis).	5 ft
122,122	δE_{ATM}	Magnitude of transponder 9 atmospheric error (line of sight).	5 ft

Table C-4
Definition of Submatrix P_{MEASd}

Element	State	Definition	Value (1 σ)
124,124	$\delta X_{T_{10}}$	Magnitude of transponder 10 survey error (X'-axis).	5 ft
125,125	$\delta Y_{T_{10}}$	Magnitude of transponder 10 survey error (Y'-axis).	5 ft
126,126	$\delta Z_{T_{10}}$	Magnitude of transponder 10 survey error (Z'-axis).	5 ft
126,126	$\delta E_{ATM_{10}}$	Magnitude of transponder 10 atmospheric error (line of sight).	5 ft
127,127	δE_{CALRR}	Magnitude of the transponder interrogator calibration error (range-rate measurement).	.01 ft
<i>All other elements are zero.</i>			

Table C-5
Definition of Submatrix Q_{MEAS}

Element	State	Definition	Value
90,90	δE_{ATM_1}	Magnitude of transponder 1 atmospheric error white noise strength.	0.1667 ft ² /sec
94,94	δE_{ATM_2}	Magnitude of transponder 2 atmospheric error white noise strength.	0.1667 ft ² /sec
98,98	δE_{ATM_3}	Magnitude of transponder 3 atmospheric error white noise strength.	0.1667 ft ² /sec
102,102	δE_{ATM_4}	Magnitude of transponder 4 atmospheric error white noise strength.	0.1667 ft ² /sec
106,106	δE_{ATM_5}	Magnitude of transponder 5 atmospheric error white noise strength.	0.1667 ft ² /sec
110,110	δE_{ATM_6}	Magnitude of transponder 6 atmospheric error white noise strength.	0.1667 ft ² /sec
114,114	δE_{ATM_7}	Magnitude of transponder 7 atmospheric error white noise strength.	0.1667 ft ² /sec
118,118	δE_{ATM_8}	Magnitude of transponder 8 atmospheric error white noise strength.	0.1667 ft ² /sec
122,122	δE_{ATM_9}	Magnitude of transponder 9 atmospheric error white noise strength.	0.1667 ft ² /sec
126,126	$\delta E_{ATM_{10}}$	Magnitude of transponder 10 atmospheric error white noise strength.	0.1667 ft ² /sec
<i>All other elements are zero.</i>			

Table C-6
Definition of Submatrix F_{MEAS}

Element	State	Definition	Value
90,90	δE_{ATM_1}	Magnitude of transponder 1 atmospheric error time constant.	$-1/300$ sec^{-1}
94,94	δE_{ATM_2}	Magnitude of transponder 2 atmospheric error time constant.	$-1/300$ sec^{-1}
98,98	δE_{ATM_3}	Magnitude of transponder 3 atmospheric error time constant.	$-1/300$ sec^{-1}
102,102	δE_{ATM_4}	Magnitude of transponder 4 atmospheric error time constant.	$-1/300$ sec^{-1}
106,106	δE_{ATM_5}	Magnitude of transponder 5 atmospheric error time constant.	$-1/300$ sec^{-1}
110,110	δE_{ATM_6}	Magnitude of transponder 6 atmospheric error time constant.	$-1/300$ sec^{-1}
114,114	δE_{ATM_7}	Magnitude of transponder 7 atmospheric error time constant.	$-1/300$ sec^{-1}
118,118	δE_{ATM_8}	Magnitude of transponder 8 atmospheric error time constant.	$-1/300$ sec^{-1}
122,122	δE_{ATM_9}	Magnitude of transponder 9 atmospheric error time constant.	$-1/300$ sec^{-1}
126,126	$\delta E_{ATM_{10}}$	Magnitude of transponder 10 atmospheric error time constant.	$-1/300$ sec^{-1}
<i>All other elements are zero.</i>			

Table C-7
Definition of matrix H_R

Element	State	Definition
1,1	$\delta\theta_x$	H'_1
1,2	$\delta\theta_y$	H'_2
1,10	δH	H'_3
1,29	δE_{CALR}	-1
1,# x_i	δX_{T_i}	$+\frac{\hat{X}_T - \hat{X}_A}{\hat{R}_C}$
1,# y_i	δY_{T_i}	$+\frac{\hat{Y}_T - \hat{Y}_A}{\hat{R}_C}$
1,# z_i	δZ_{T_i}	$+\frac{\hat{Z}_T - \hat{Z}_A}{\hat{R}_C}$
1,# ATM_i	δE_{ATM_i}	-1
<i>All other elements are zero.</i>		

$$[H'_1 \ H'_2 \ H'_3] = \left[-\frac{\hat{X}_T - \hat{X}_A}{\hat{R}_C} \quad -\frac{\hat{Y}_T - \hat{Y}_A}{\hat{R}_C} \quad -\frac{\hat{Z}_T - \hat{Z}_A}{\hat{R}_C} \right] C_N^E(\hat{L}, \hat{\lambda}, \hat{\alpha}) \begin{bmatrix} T_i(\hat{\alpha}, \hat{L}) & 0 \\ 0 & 1 \end{bmatrix} \quad (C-1)$$

- Notes:
1. $i = 1, \dots, 10$ with element number selected from Tables C-1 thru C-4.
 2. $(\hat{X}_T, \hat{Y}_T, \hat{Z}_T)$ corresponds to transponder mapped to the i th element.
 3. H' transformation is required to transform from INS position frame to ECEF frame.
 4. C_N^E is defined in Eq (2-6).
 5. T_i is defined in Eq (3-29).
 6. The # symbol represents the number of the corresponding states in the 10 transponder window for the transponder being sampled at the applicable measurement update time.

Table C-8
Definition of matrix H_{RR}

Element	State	Definition
1,1	$\delta\Theta_x$	H_1''
1,2	$\delta\Theta_y$	H_2''
1,10	δH	H_3''
1,7	δV_x	H_4''
1,8	δV_y	H_5''
1,9	δV_z	H_6''
1,70	δE_{CALRR}	-1

All other elements are zero.

$$[H_1'' \ H_2'' \ H_3''] =$$

$$\left[\begin{array}{l} - \frac{(\hat{X}_T - \hat{X}_A)^2 \hat{V}_{AX} + (\hat{X}_T - \hat{X}_A)(\hat{Y}_T - \hat{Y}_A) \hat{V}_{AY} + (\hat{X}_T - \hat{X}_A)(\hat{Z}_T - \hat{Z}_A) \hat{V}_{AZ} - \hat{V}_{AX} \hat{R}_C^2}{\hat{R}_C^3} \\ - \frac{(\hat{Y}_T - \hat{Y}_A)^2 \hat{V}_{AY} + (\hat{Y}_T - \hat{Y}_A)(\hat{X}_T - \hat{X}_A) \hat{V}_{AX} + (\hat{Y}_T - \hat{Y}_A)(\hat{Z}_T - \hat{Z}_A) \hat{V}_{AZ} - \hat{V}_{AY} \hat{R}_C^2}{\hat{R}_C^3} \\ - \frac{(\hat{Z}_T - \hat{Z}_A)^2 \hat{V}_{AZ} + (\hat{Z}_T - \hat{Z}_A)(\hat{X}_T - \hat{X}_A) \hat{V}_{AX} + (\hat{Z}_T - \hat{Z}_A)(\hat{Y}_T - \hat{Y}_A) \hat{V}_{AY} - \hat{V}_{AZ} \hat{R}_C^2}{\hat{R}_C^3} \end{array} \right]$$

$$C_N^E(\hat{L}, \hat{\lambda}, \hat{\alpha}) \begin{bmatrix} T_A(\hat{\alpha}, \hat{L}) & 0 \\ 0 & 1 \end{bmatrix} \quad (C-2)$$

$$[H_4'' \ H_5'' \ H_6''] = \begin{bmatrix} -\frac{\hat{X}_T - \hat{X}_A}{\hat{R}_C} & -\frac{\hat{Y}_T - \hat{Y}_A}{\hat{R}_C} & -\frac{\hat{Z}_T - \hat{Z}_A}{\hat{R}_C} \end{bmatrix} C_P^E(\hat{L}, \hat{\lambda}, \hat{\alpha}) \quad (C-3)$$

- Notes:
1. $(\hat{X}_T, \hat{Y}_T, \hat{Z}_T)$ corresponds to the transponder position used in the range measurement update.
 2. H'' transformation is required to transform from INS position and velocity frame to ECEF frame.
 3. C_N^E is defined in Eq (2-6).

Appendix D

INS and Baro Altimeter CIRIS Flight Data

This appendix contains the CIRIS flight INS position, velocity, acceleration, and wander azimuth angle (α) time histories; the baro altimeter altitude rate time history is also included. This data is to drive the full ordered Kalman filter simulation. The data is shown in Figures D-1 thru D-11.

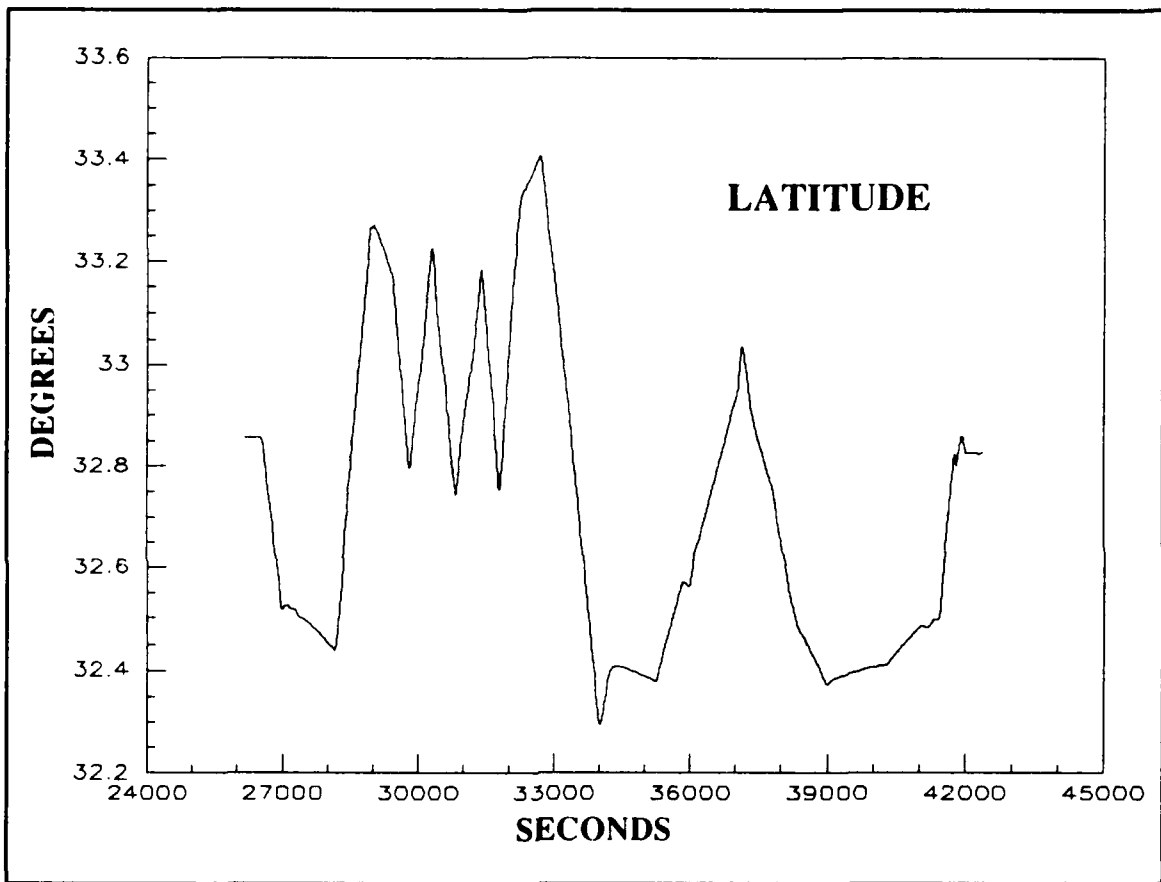


Figure D-1. Latitude Trajectory for CIRIS Flight

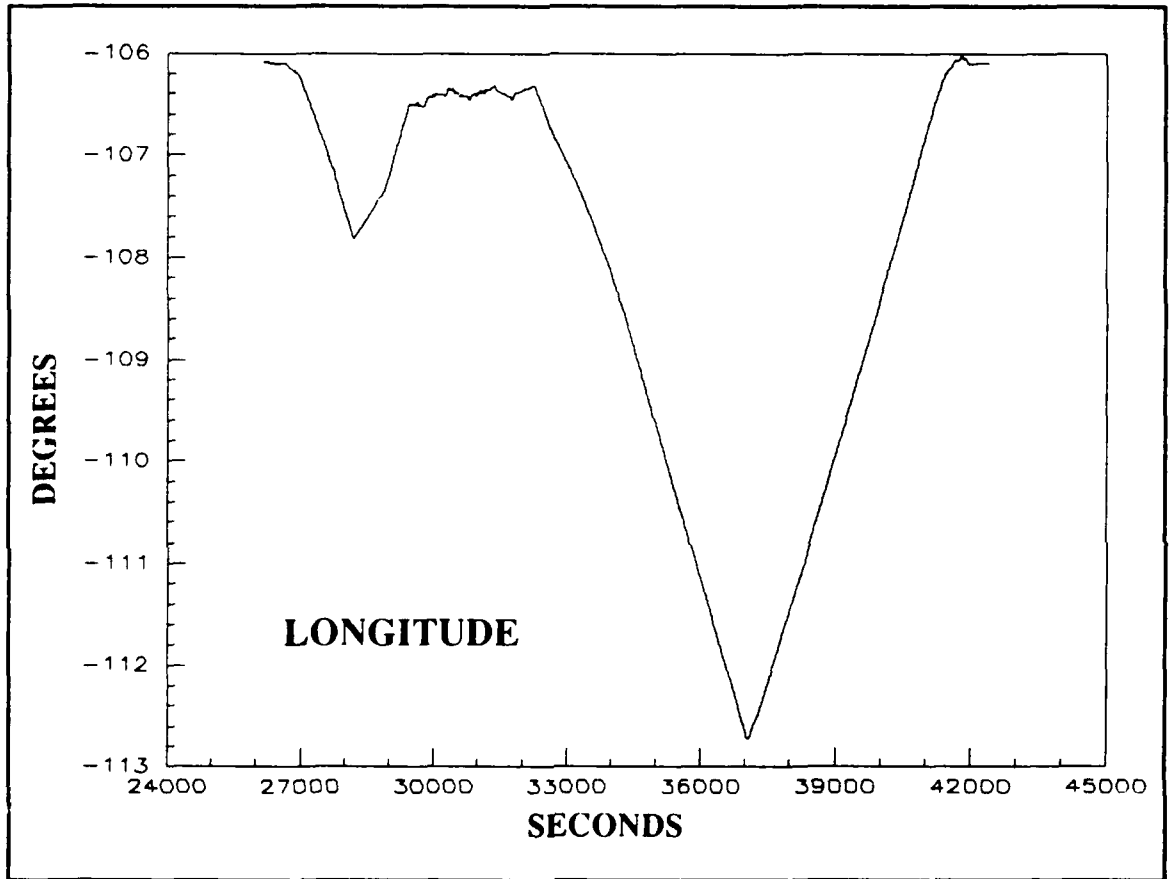


Figure D-2. Longitude Trajectory for CIRIS Flight

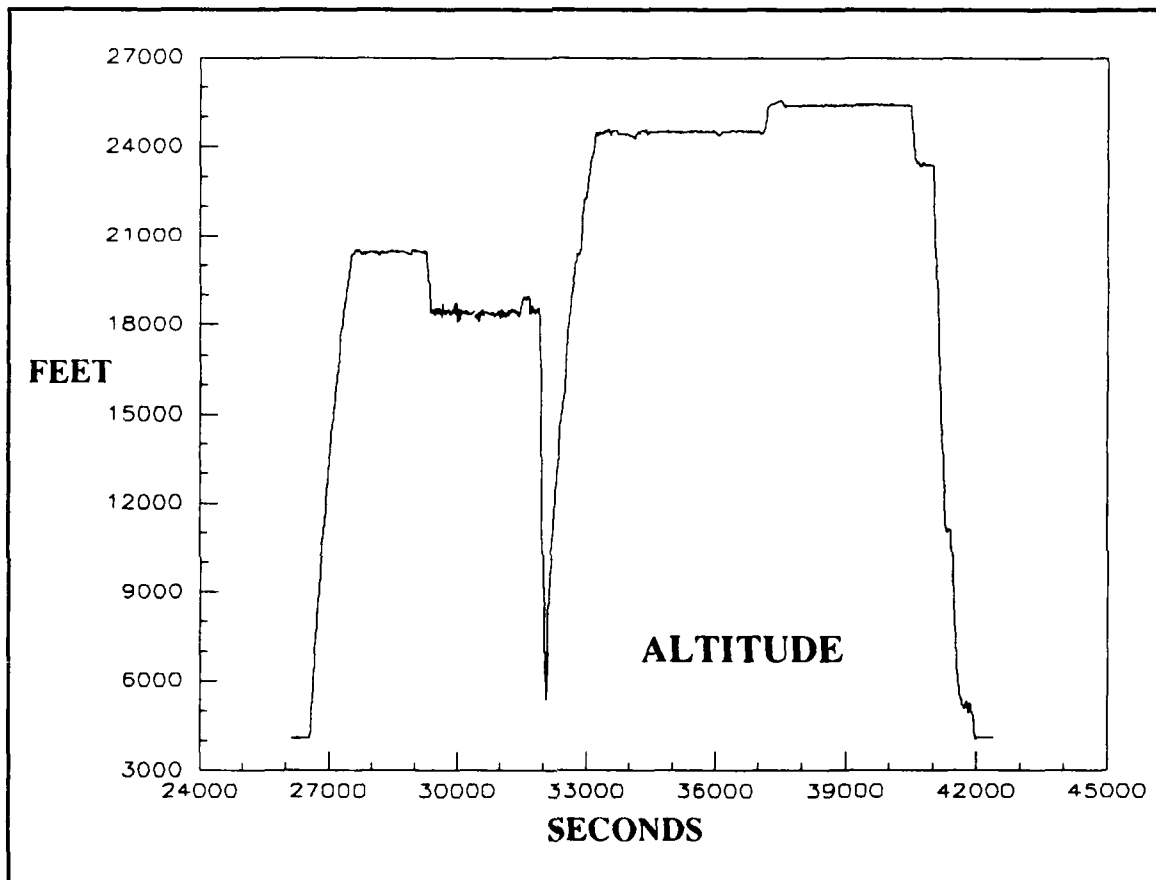


Figure D-3. Altitude Trajectory for CIRIS Flight

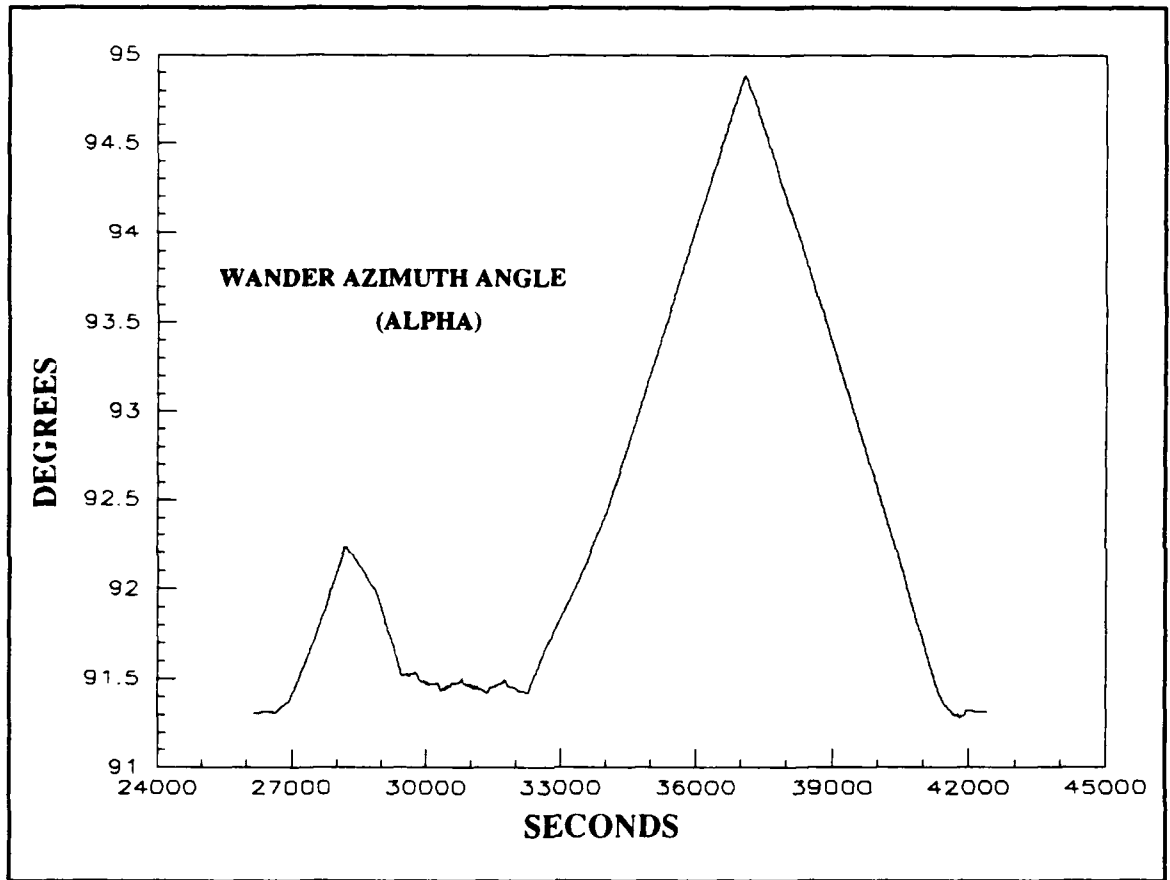


Figure D-4. Alpha Angle Time History for CIRIS Flight

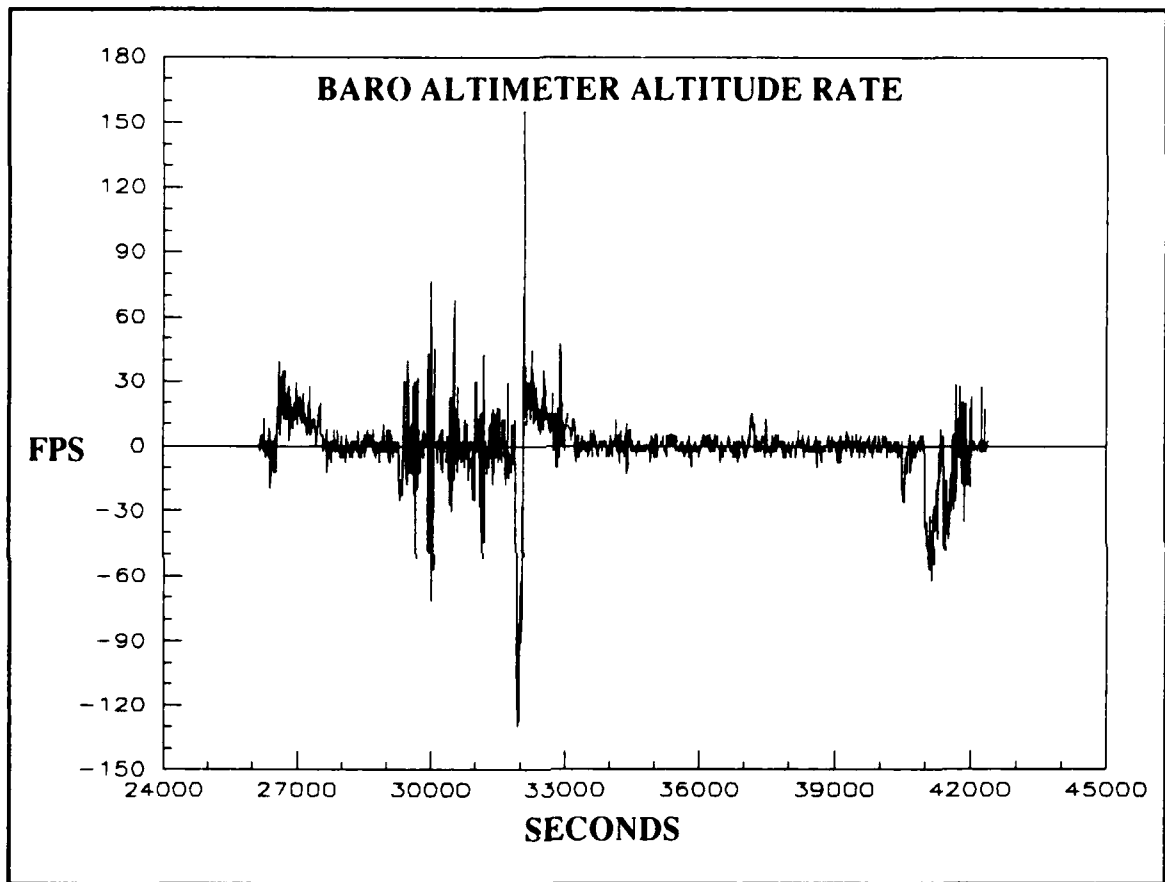


Figure D-5. Baro Altimeter Altitude Rate Time History for CIRIS Flight

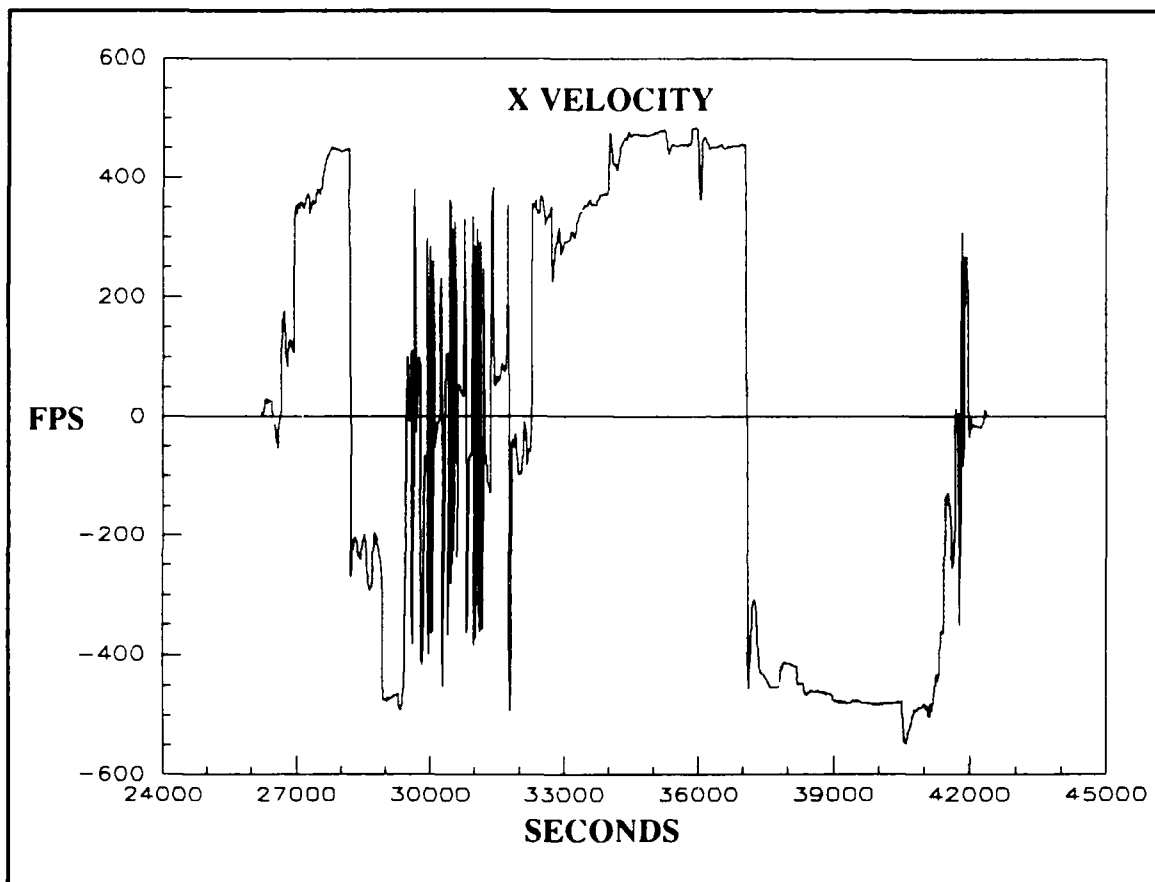


Figure D-6. X Velocity Time History for CIRIS Flight

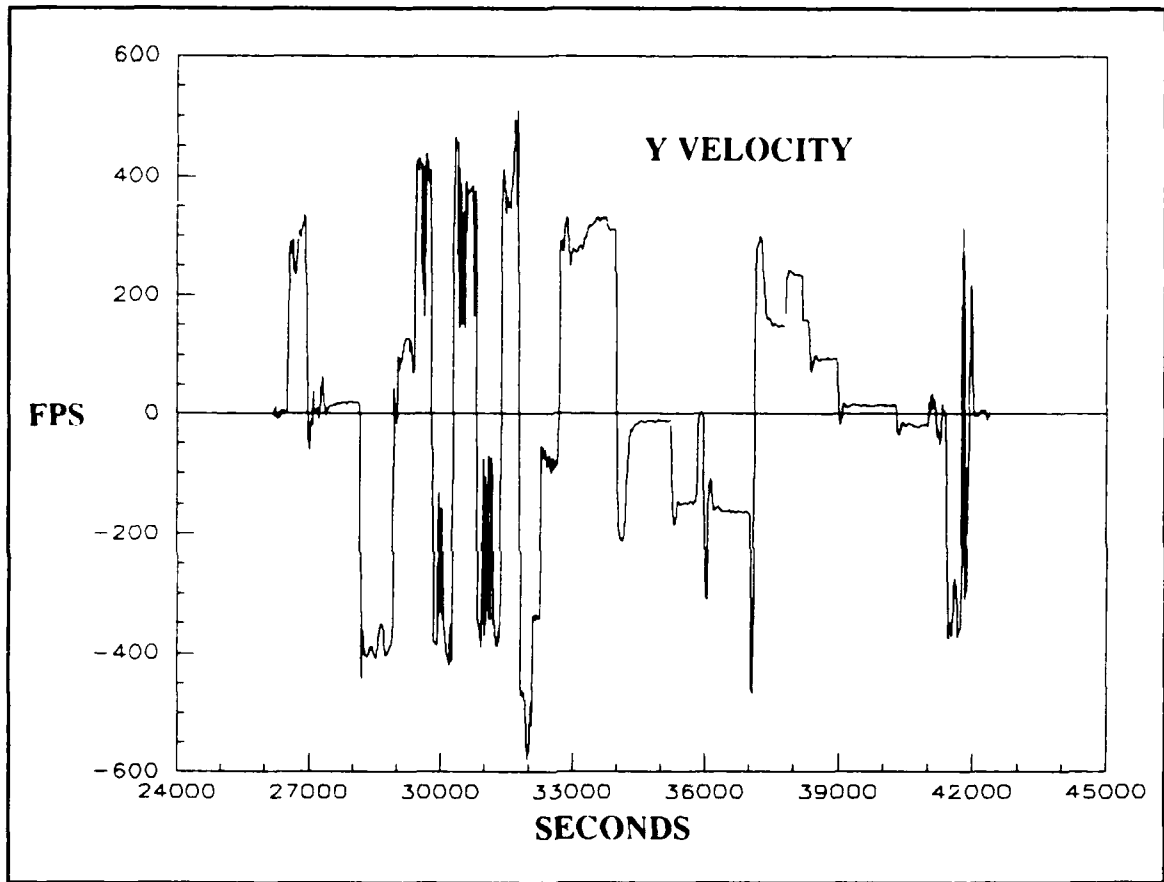


Figure D-7. Y Velocity Time History for CIRIS Flight

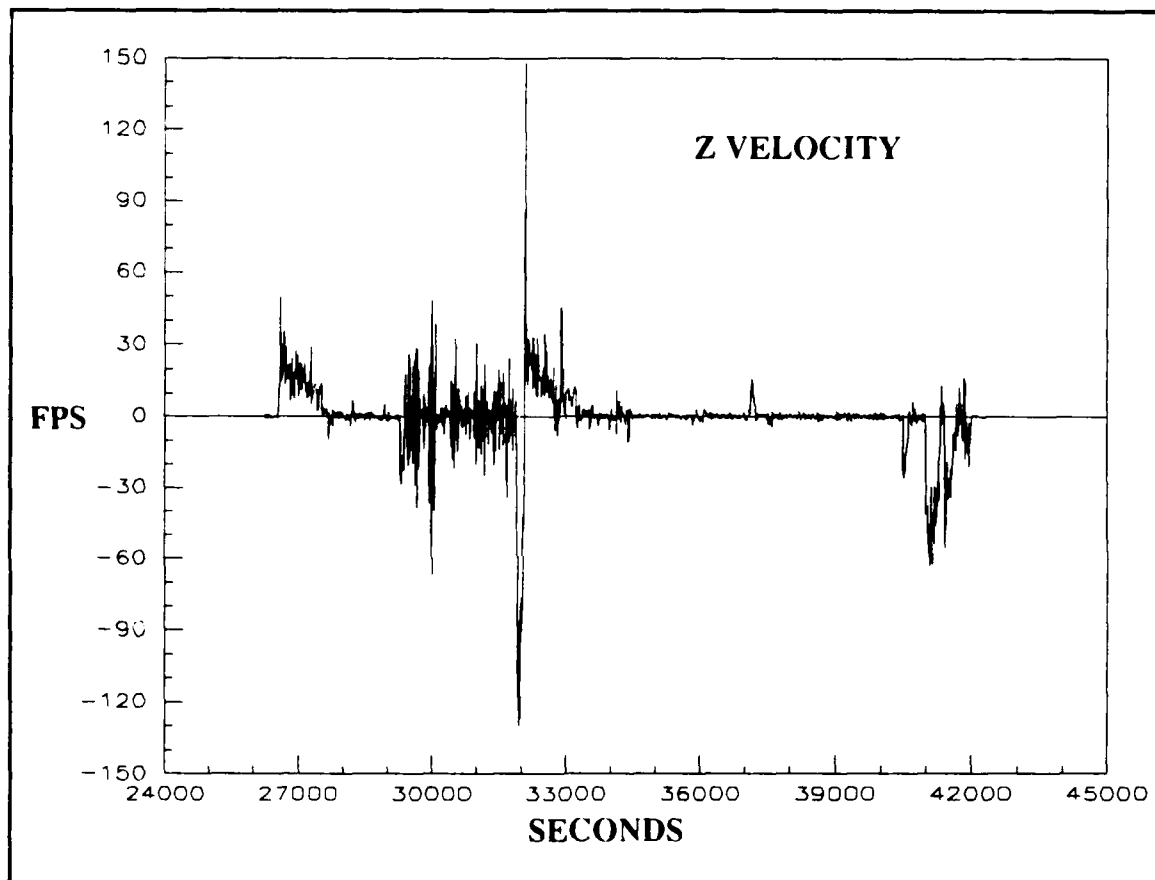


Figure D-8. Z Velocity Time History for CIRIS Flight

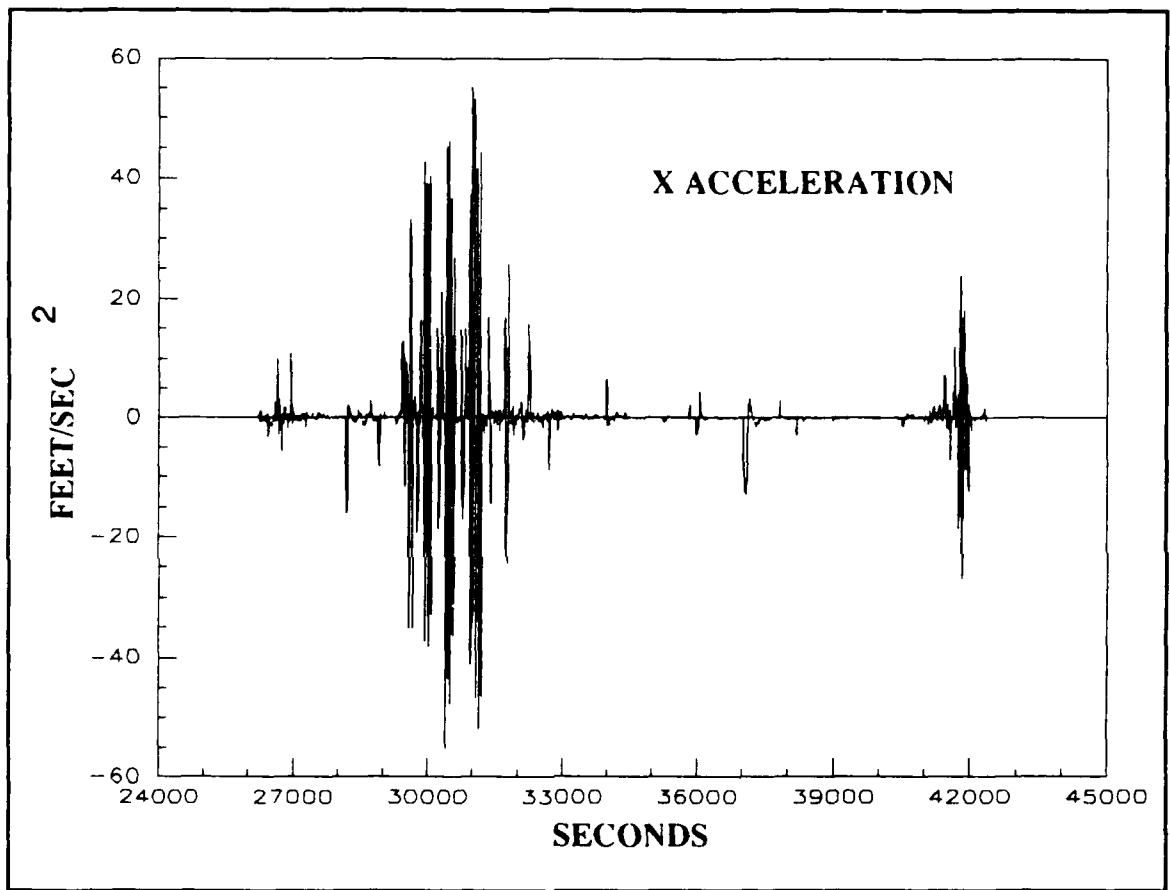


Figure D-9. X Acceleration Time History for CIRIS Flight

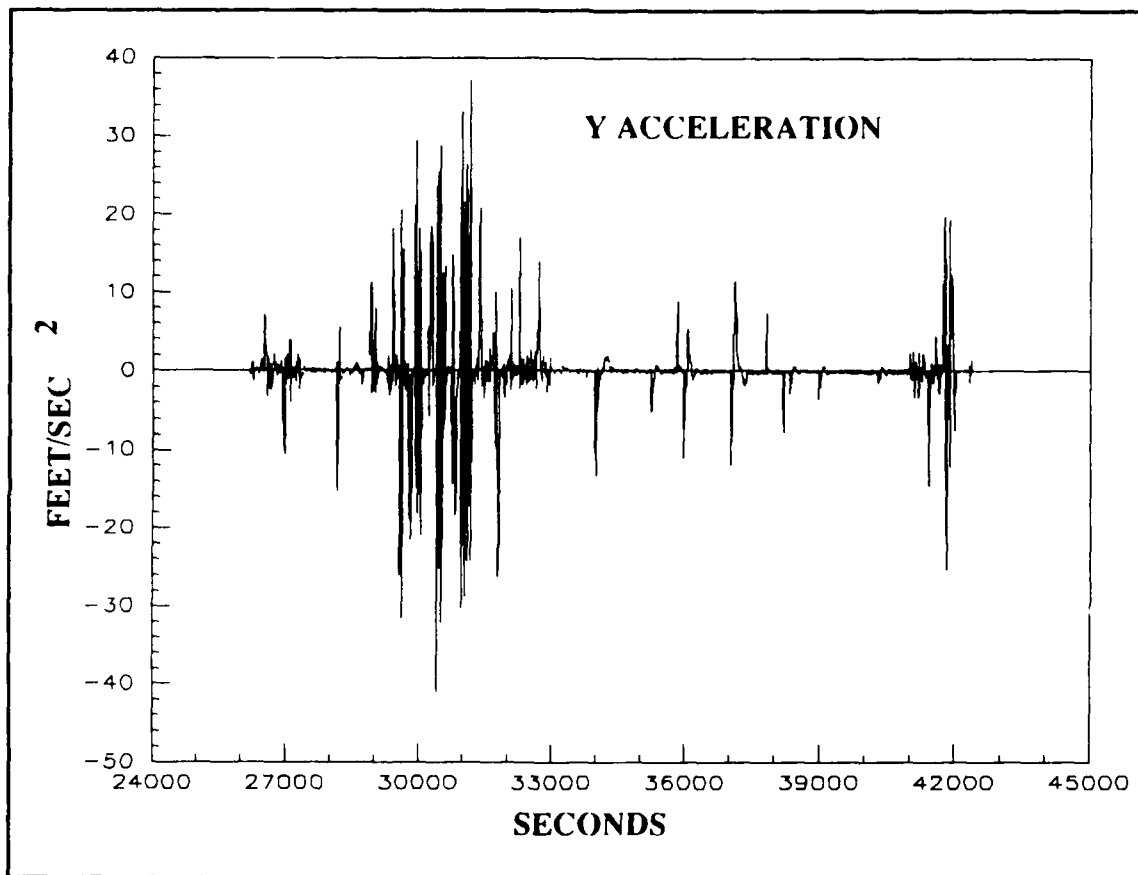


Figure D-10. Y Acceleration Time History for CIRIS Flight

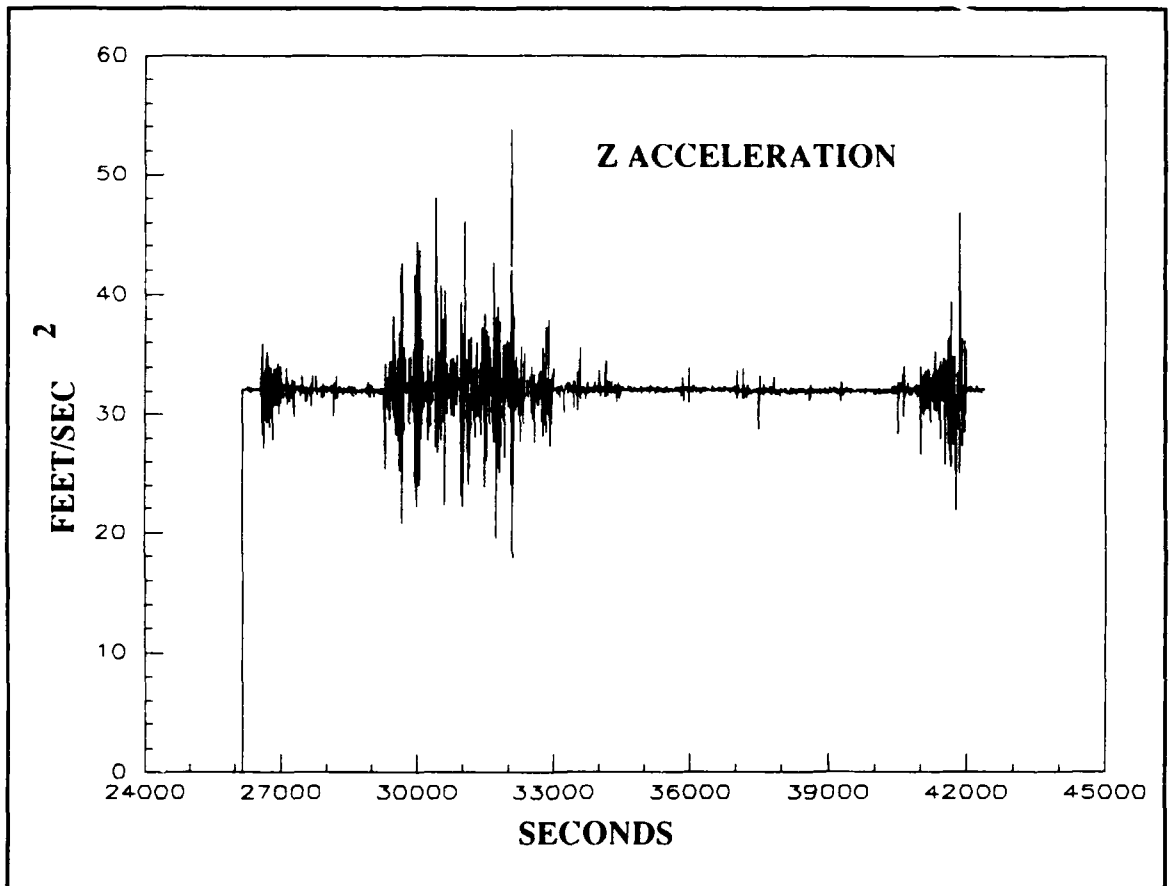


Figure D-11. Z Acceleration Time History for CIRIS Flight

Bibliography

1. Air Force Avionics Laboratory. PROFGEN - A Computer Program for Generating Flight Profiles, Technical Report AFAL-TR-76-247, November 1976. AFWAL/AAAN-2, Wright-Patterson AFB, OH.
2. Breaux, Harold J. An Efficiency Study of Several Techniques for the Numerical Integration of the Equations of Motion for Missiles and Shell, Report No. 1358, Ballistic Research Laboratories, Aberdeen Proving Ground, Maryland, February 1967.
3. Britting, Kenneth R. Inertial Navigation System Analysis, New York:Wiley-Interscience, 1971.
4. Butler, R. R. And Rhue, G. T., "Kalman Filter Design for an Inertial Navigation System Aided by Non-Synchronous Navigation Satellite Constellations," Masters Thesis, Air Force Institute of Technology, Wright-Patterson AFB, Ohio, March, 1974.
5. Carlson, Neal A. and Stanton H. Musick. MSOFE User's Manual: Multimode Simulation for Optimal Filter Evaluation, October 1987. Contract F33615-86-C-1087, Subcontract 2013-S1, Avionics Lab, AFWAL/AAAN-2, Wright-Patterson AFB, Ohio.
6. Cox, D. B. "Integration of GPS with Inertial Navigation Systems," Global Positioning System, Papers Published in Navigation, Volume I, The Institute of Navigation, Washington, D.C., 1980.
7. Cubic Corporation. Range/Range-Rate Subsystem (RRS) for the Completely Integrated Reference Instrumentation System (CIRIS), AFSWC TR-7321, Cubic Corporation, 9233 Balboa Avenue, San Diego, Ca., August 1973.
8. Defense Mapping Agency. Department of Defense World Geodetic System 1984. Defense Mapping Agency Technical Report, No. DMA TR 8350.2. Washington, D.C., 30 September 1987.
9. Dyrd, D. Litton Design Engineer, Telephone Conversations, Litton Guidance and Control Systems, Woodland Hills, CA., Comm: 818-715-2991, April 1987.
10. Guidance and Control Division. LN-39 Standard Inertial Navigation System AN/ASN-141, Technical Description, Litton Systems INC., 5500 Canoga Avenue, Woodland Hills, Ca., September 1987.
11. Guidance Test Division. "CIRIS II Test Summary Report," In-House Report, CIGTF, 6585th Test Group, Holloman AFB, NM, May 1988.

Bibliography

12. Guidance Test Division. "The Completely Integrated Reference Instrumentation System (CIRIS)," Unpublished Contractor Informational Pamphlet, CIGTF, 6585th Test Group, Holloman AFB, NM.
13. Huddle, James R. "Inertial Navigation System Error Model Considerations in Kalman Filter Applications," Advances in the Techniques and Technology of the Application of Nonlinear Filters and Kalman Filters, AGARD-AG-256, Advisory Group for Aerospace Research and Development, 13-1:13-19 (March 1982).
14. Intermetrics Incorporated. Computer Program Detailed Technical Description CEI-II-72-B Post-Flight Processor for Ciris, Volume III, Part II, Contract End Item Specification, Intermetrics Incorporated, Cambridge, MA, 7 May 1974.
15. Lewantowicz, Lt Col Zdzislaw H. Deputy Department Head, Department of Electrical and Computer Engineering, Personal Interviews, Air Force Institute of Technology, Wright-Patterson AFB, Oh, 28 March thru 21 April 1988.
16. Maybeck, Peter S. Stochastic Models, Estimation, and Control, Volume I, New York: Academic Press, 1979.
17. Maybeck, Peter S. Stochastic Models, Estimation, and Control, Volume II, New York: Academic Press, 1982.
18. Simkin, Gordon. CIRIS Post-Flight Performance Engineer, Personal Interviews, Central Inertial Guidance Test Facility, Holloman AFB, NM, 1-3 March 1989.
19. Smith, Carl O. Performance Characteristics of Integrated Inertial Navigation Systems, Masters Thesis, Air Force Institute of Technology, Wright-Patterson AFB, Oh, December, 1985.
20. Solomon, Joseph K. "CIRIS Special Study," Final Report, EENG 699, Air Force Institute of Technology, Wright-Patterson AFB, OH, March 1989.
21. Speiser, M. "Systems Engineering Analysis Report for the F-16 Standard Inertial Navigation Unit," Litton Guidance and Control Systems, Woodland Hills, CA., Revision B, March 1985.
22. Walker, Robert, Charles Gregory, and Sunil Shah. "MATRIX_x: A Data Analysis, System Identification, Control Design, and Simulation Package," Control System Magazine, Volume 2, Number 4, 30-36 (December 1982).

Vita

Captain Joseph K. Solomon [REDACTED]

He served as an enlisted electronic technician in the Air Force from 1975 to 1981. At this time he entered the Airman Education and Commissioning Program (AECP) and earned a Bachelor of Science degree in Mechanical Engineering from the University of Colorado in May 1984. Upon graduation he received a commission in the Air Force by attending the USAF Officer Training School (OTS). His first assignment was as part of the engineering team at the U.S. Air Force's High Speed Test Track in New Mexico from 1984 to 1987. In June of 1987, he entered the Air Force Institute of Technology to pursue a masters degree in electrical engineering, specializing in the aircraft navigation and stochastic control areas. He is a member of the IEEE and ASME.

[REDACTED] [REDACTED]